Experimental hydrodynamic instability at high energy density

by

Carlos Alex Di Stefano

A dissertation submitted in partial fulfillment
of the requirements for the degree of
Doctor of Philosophy
(Applied Physics)
in the University of Michigan
2014

Doctoral Committee:

      Assistant Research Scientist Carolyn C. Kuranz, co-chair
      Professor R Paul Drake, co-chair
      Associate Professor John E. Foster
      Assistant Professor Eric Johnsen
      Professor Gregory Tarle

To the many amazing people and experiences the world has put in my path over the years, and who have lent me strength and vibrancy in my pursuits.

ACKNOWLEDGMENTS

An undertaking like a Ph.D. doesn't happen without the support of a great many people along the way, and I would be remiss if I didn't mention some of these people's contributions, and their friendship, over the last several years of my life.

First and foremost, I was extremely fortunate to find my co-advisors Paul Drake and Carolyn Kuranz. Their (continuing) mentorship is first-rate, and they fostered an atmosphere that encouraged my growth as a physicist, as a professional, and as a human being. My fellow graduate students over the years, and in particular Channing Huntington, Christine Krauland, and Forrest Doss, have been a tremendous source of camaraderie as well as technical conversation. Our group's engineering staff, Sallee Klein, Donna Marion, Mike Grosskopf, and Robb Gillespie, all put up with my learning curve in designing experimental targets, and worked wonders of various magnitudes in the course of my experimental work.

My family is a source of encouragement, stress relief, and scientifically-literate conversation, as appropriate. So, to my mom, my brother, the cat, the memory of my dad, and my relatives cheering me on from Argentina: all the thanks I can muster.

A lot of writing happened at Mighty Good Coffee and at Zingerman's Coffee Company. Hannah, Keelan, and the other baristas kept me going with their hospitality.

And last, but certainly not least, I benefitted greatly from Guy Malamud's theoretical expertise during many coffee-fueled conversations, despite him not particularly caring about my problems. However, Guy, I want this on the record: *I don't care that you don't care.*

TABLE OF CONTENTS

LIST OF FIGURES

LIST OF ABBREVIATIONS

CRF carbonized resorcinol formaldehyde

KH Kelvin–Helmholtz

RM Richtmyer–Meshkov

RT Rayleigh–Taylor

MZ mixing zone

HED high-energy-density

PAI polyamide-imide

PI polyimide

FWHM full width at half-maximum

TI thermal insulator

ICF inertial-confinement fusion

JLF Jupiter Laser Facility

SN supernova

SCI Spherical Crystal Imager

NIF National Ignition Facility

LLE Laboratory for Laser Energetics

LLNL Lawrence Livermore National Laboratory

SNR signal-to-noise ratio

TI thermal insulator

LLCS Lawrence Livermore Crystal Spectrometer

EPPS Electron Positron Proton Spectrometer

EOS equation of state

LSF laser scaling factor

ABSTRACT

Experimental hydrodynamic instability at high energy density

by

Carlos Di Stefano

co-chairs: Carolyn Kuranz, R. Paul Drake

This dissertation presents a series of experiments on various aspects of shock-driven hydrodynamic instability at high energy density (HED). This is an aspect of physics with ramifications in many important applications, for example in the confinement of fusion fuel and in many astrophysical phenomena. The common theme in this research lies in the experimental technique. These experiments, and others like them, are typically performed using a system of initially-solid plastic and carbon foam, where the surface of the plastic in contact with the foam can be easily machined with a seed perturbation, allowing for precise control of the unstable interface growth under well-characterized initial conditions. A high-powered, pulsed laser is then used to irradiate the system, driving a shock wave into it. This shock ionizes and accelerates the system, converting it into an HED plasma. The acceleration and/or the subsequent motion of the shocked plasma provides the impetus that drives the instability, where the particular mechanisms at work are controlled by the direction of incidence of the shock upon the material interface, as well as by appropriate choice of an initial interface perturbation.

The first three experiments explore various details of three important interface

processes: Rayleigh-Taylor and Kelvin-Helmholtz instability, as well as Richtmyer-Meshkov physics. The final experiment studies the generation of fast electrons by the interaction of a laser with a material. These electrons are produced in virtually any HED system involving a laser, and can affect the system's dynamics significantly. They are of particular interest for the fast-ignition concept in inertial-confinement fusion, and also can have an effect on imaging-based diagnostics, such as the X-ray radiography techniques that are the primary method for diagnosing the instability experiments that are the focus of this dissertation.

CHAPTER I

Introduction

1.1 Shock-driven hydrodynamics

The question of the stability or instability of an interface between two fluids is an important one in any imaginable physical situation in which two liquids, gases, or plasmas come into contact with one another, and some manner of force is applied to the system. Instability phenomena result in the mixing (or at least rearranging) of the fluids involved and are found in nature, such as an air bubble rising in water, clouds blown through the sky by wind, or the dynamics of an expanding nebula, and also play important roles in a wide range of technologies involving fluids, for example in jet engines and inertial-confinement fusion (ICF). In the work to be described in this dissertation, I am particularly concerned with hydrodynamic instability in high-energy-density (HED) systems, in which the instability occurs at the interface between two materials at differing densities. The exact meaning of HED will be discussed in Section 1.2, but in its simplest description, as the name implies, HED refers to any situation in which a sufficiently large amount of energy is deposited into a sufficiently small space that matter begins to behave unexpectedly. The practical consequences are that the material typically ionizes, at least partially, and that a shock wave forms as the concentrated energy seeks to disperse. This shock wave (or shock waves) tends to be the primary impetus driving the subsequent dynamics of

the system.

1.1.1 Shock and blast waves

To understand how a shock wave forms, imagine that some quantity of energy is deposited locally in a system. The system will, in response, seek to dissipate this energy. Sound is the natural mechanism to accomplish this, and sound travels, in a given fluid for instance, at a characteristic velocity c that is dependent on the fluid's properties. However, a fluid can be forced to carry energy at a faster speed than this, by increasing the pressure p or, alternatively, the energy density, beyond the pressure modulations δp associated with c, which for a fluid at density ρ goes as $\sim (\delta \rho)c^2$ [23, 28]. (This is essentially an alternative expression of the definition of the sound speed from the wave equation.) When this happens, the wave fronts begin to pile up on each other, and a shock wave is formed. Fig. 1.1 shows a classic pedagogical example of this, where shocks are created by an object physically moving through a gas faster than the gas' sound speed, and therefore displacing the gas at a speed faster than the gas' sound speed. In this image, as the object moves some distance through the gas, it creates an area of higher gas pressure–and therefore energy density–at its surface due to the volume of air it has physically displaced. This localized energy then dissipates via the outward propagation of a pressure modulation (sound). However, the object is moving faster than the modulation can propagate (i.e. faster than the sound speed). Subsequent modulations, created as the object continues to move through the gas, then pile up, producing a shock. Two such shocks are visible in Fig. 1.1 as the dark lines emanating from the points of increasing slope of the object with respect to the airflow.

This example shows a shock being driven by mechanical force, although in practice any source of energy can accomplish this. In particular, the work to be described in this dissertation uses high-power pulsed lasers to deposit this energy. In all cases, the
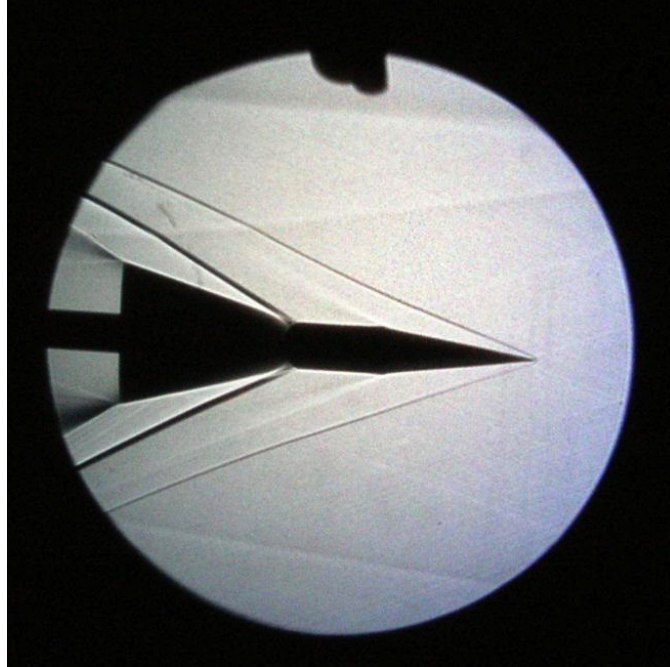
Figure 1.1: Schlieren image of an airplane-like geometrical object intercepting an airflow faster than the air's sound speed. Photo credit: M. A. Di Stefano

physical consequences of the shock's propagation are that the medium is accelerated to some velocity (that can be a significant fraction of the shock's velocity), it is heated, and its pressure and density increase. This deposition of kinetic and thermal energy into the fluid is how a shock dissipates energy. Finally, if the source of pressure ceases, a low-pressure front will propagate through the shocked material, as the material near the source location will now be allowed to expand. This is known as a rarefaction, and propagates at the shocked material's sound speed, which is faster than the shock itself [23]. When the rarefaction overtakes the shock, the shock becomes a blast wave. Blast waves tend to exhibit different dynamics than shock waves because, absent the shock wave's continued source of energy or pressure, they lose strength as they propagate.

1.1.2   Shock-driven instability

If a system such as those described previously contains material interfaces in unstable configurations, this deposition of energy into the system can cause the involved

fluids to mix. When we refer to an "unstable" configuration or an "instability" in this work, we mean the behavior of a nominally-flat interface that experiences some perturbation. Generally, if application of a force to this interface causes the material displaced by perturbation to tend to return to its nominal position, the interface is referred to as "stable." The opposite situation, in which displacement of material under application of a force to tend to cause further displacement and therefore growth of perturbation features, is called "unstable." Three fundamental hydrodynamic processes leading to this manner of outcome are the object of inquiry of the experiments described in this dissertation.

Perhaps the most intuitively visualized example of these processes is the Rayleigh–Taylor (RT) instability [74, 94], a phenomenon closely related to the idea of buoyancy. As a simple example, perturbation of the surface of deep water (a wave) will cause the displacement in time $z(t)$ from the mean surface (interface) of a particular location to exhibit oscillations at a frequency ω, going as $z(t) \sim \cos \omega t$, where $\omega = \sqrt{g/k}$ [47]. Here, g is the gravitational acceleration and k is the wavenumber. This is shown schematically in Fig. 1.2a. The relevant properties of the system, in the simplest
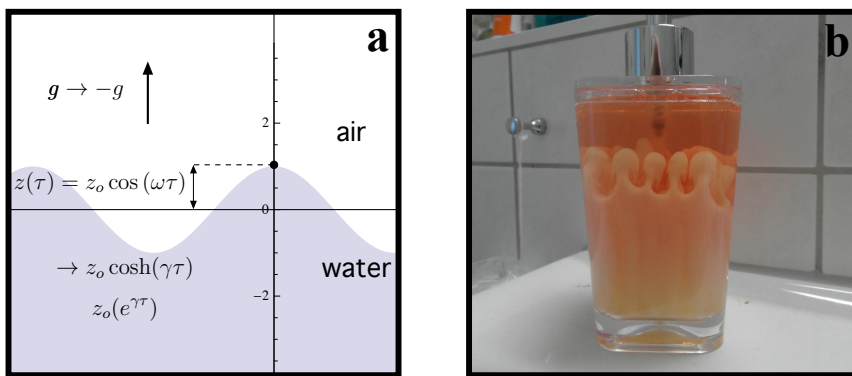
Figure 1.2: a. Schematic of the RT-stable phenomenon of deep-water waves. Inverting the two fluids changes the sign of gravitational acceleration, resulting in a runaway exponential instead of a self-correcting oscillation; b. An example of the RT instability of two soaps of differing density. Photo credit: Redditor Thermoskanne.

consideration of this situation, are that the two fluids (air and water) have differing

densities, and that the accelerating force (gravity) is acting perpendicular to the fluids' interface and from the less-dense to the more-dense fluid. If the fluids were to be inverted or, equivalently, if the direction and hence the sign of g were to change, the resulting motion would be a sinusoid with an imaginary argument: an exponential, where now $z(t) \sim e^{|\omega|t}$. This situation is demonstrated in Fig. 1.2b, in which soap was poured into a dispenser already partially-filled with another soap, such that the soap on top was denser than the soap on bottom, and left for several hours.

There are two important details regarding this result. The first is that the quantity $|\omega|$ is typically denoted γ and referred to as the growth rate. The value described above is the special case corresponding to two fluids in which one has a much larger density than the other, such that the Atwood number $A_n = (\rho_2 - \rho_1)/(\rho_2 + \rho_1)$ is approximately 1. In general, $\gamma = \sqrt{A_n k g}$. The second, a typical caveat in this type of analysis, is that it is only valid when the displacement from the mean interface is small (here, this assumption was invoked in the derivation of an equation for deep-water waves). This is referred to as the linear phase, because the relevant equations of motion can be simplified by linearizing them. As the displacement becomes a significant fraction of the feature's wavelength, the assumption no longer holds, and the interface's behavior changes. This behavior is typically referred to as nonlinear.

Kelvin–Helmholtz (KH) instability [95, 34] of a perturbed material interface arises when there is shear present at the interface. This arises naturally when a force is applied parallel to the interface, resulting in one of the fluids flowing over the other. This behavior is shown schematically in Fig. 1.3. The shear creates a torque on
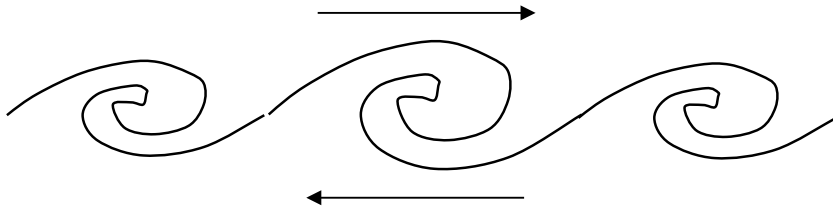
Figure 1.3: Schematic of the shearing motion leading to KH instability.

the tips of any present perturbation features, and consequently deposits vorticity at their locations over time, resulting in the growth of vortices where the feature was initially located. It is worth noting that KH instability can and often does occur simultaneously with RT instability. This is prominent in, for example, atmospheric phenomena, where shear leading to KH might be generated by wind, while gravity creates the buoyancy leading to RT. As a secondary effect, KH also occurs as a result of the shear that occurs at the tips of RT features as they interpenetrate. This oftentimes results in the features having an appearance similar to a mushroom stem and cap. This effect is clearly visible in the RT interface structure of the soaps in Fig. 1.2.

The Richtmyer–Meshkov (RM) process [76, 62] deserves special consideration in this respect. RM is not a process of instability, as the growth of structure is not related to the structure's continued displacement, but because the end result appears similar to an instability, it is often treated together with true hydrodynamic instabilities. RM arises because a shock travels at different speeds in two otherwise-identical materials at different densities. If two such materials have a perfectly flat interface, and a planar shock is traveling normal to this interface, the shock will cross the interface, and therefore change speed, at every location simultaneously. However, if the interface has some perturbation, there will be a brief period of time in which the shock is in different materials, and therefore traveling at different speeds, in adjacent locations. This creates a torque and deposits vorticity at the interface during the time it takes the shock to traverse the interface. This vorticity remains following shock passage, and results in the growth of the perturbation feature over time. This effect is shown schematically in Fig. 1.4. Finally, it is worth noting that the RM process is independent of the direction of density increase, and will both occur when the shock encounters an interface with a density increase (and thus the interface is RT-stable, and only experiences RM growth) and when the shock encounters a density decrease

6
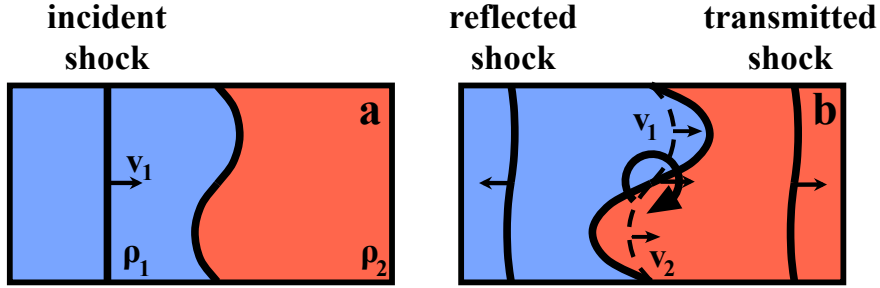
Figure 1.4: Schematic of the RM process. a. An incident shock wave approaching a perturbed interface; b. The shock wave as it crosses the interface, denoted by a dotted line, as well as the resulting forwards-propagating transmitted shock and the backwards-propagating reflected shock.

(and thus the interface will also be RT-unstable).

In the context of systems involving shock waves, unstable mixing can be driven by the direct acceleration of the fluids by the shock, by the motion of the shocked fluids, or both. Depending on the direction of incidence of the shock upon the interface (the primary relevant components are perpendicular to the interface in the direction of density *increase*, parallel to the interface, and perpendicular to the interface in the direction of density *decrease*), the subsequent motion of the fluids relative to the interface will be different, and therefore different physical mechanisms occur that can contribute to the mixing. Exploration of the details of this mixing are the primary focus and motivation of the work described in this dissertation, with experiments focused on the primary mechanisms involved in each of these three directional cases described in Chapters II, III, and IV, respectively. In the remainder of this chapter, I will discuss common aspects of these experiments. In particular, the physical properties of HED systems lead to some common elements among the experiments and will be presented in Section 1.2, while the experimental technique to create and diagnose these related systems share many similarities, and will be discussed in Section 1.3. The instability hydrodynamics in each case, however, are unique to each experiment, and will be discussed individually in the relevant chapters.

1.2 High-energy-density physics

1.2.1 The HED condition

As the name "high-energy-density physics" suggests, this field of study concerns itself with systems in which a sufficiently large amount of energy is introduced into a sufficiently small physical space that the materials involved begin to behave in a manner which deviates from our typical experiences in what we might call a "normal-energy-density" regime. The property of matter which most concisely indicates what constitutes "sufficient" is perhaps the bulk modulus K, the measure of a material's resistance to compression. A glance at tabulated values of K [41] for various solid materials shows that K tends to take values on the order of 100 GPa, or 1 Mbar (one million atmospheres). This threshhold, then becomes a convenient way to define a high-energy-density system: a system in which sufficient energy is introduced that the pressure rises above one million atmospheres [16, 23]. Introducing enough energy to bring a system to a pressure of or beyond this order of magnitude causes the constituent materials to break down into an ionized plasma state in which, among other phenomena provoked by the high temperatures and pressures, shocks are often produced. These shocks in HED systems, and the hydrodynamic instability they drive, are the focus of the work described in this dissertation.

In order to illustrate the wide-ranging application and interest of HED physics, I present here two examples of HED phenomena at opposite extremes, both in terms of size and in terms of the physical properties of their respective systems. Fig. 1.5 shows an X-ray image of the remnant of supernova (SN) 1572, otherwise known as Tycho's supernova. This image shows the gas cloud left over from the original star's supernova event. The sharply-defined, violet border corresponds to the spherical blast-wave front, still expanding outwards nearly 500 years later. The temperature near the front is on the order of roughly 20 million Kelvin, the blast-wave velocity is
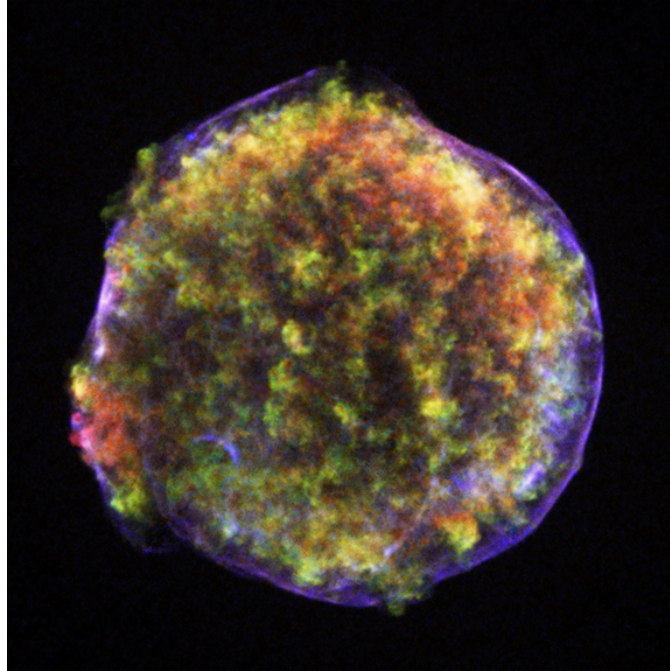
Figure 1.5: A false-color X-ray image of the remnant of SN1572, where the visible color spectrum is calibrated to an X-ray energy range of roughly 1-6 keV. Photo credit: Chandra X-Ray Observatory

approximately 5000 km/s, and the ambient density is approximately 0.2 particles per cm^3. One amazing feature of the incredible scales of SN1572's physical properties is that the width of the shock front, which can be adequately modeled as a discontinuity, actually has a width of order 100 million meters. [27]

In contrast, Fig. 1.6 shows an image of an ICF fuel pellet, balanced on a human fingertip [30]. In the ICF technique, a spherical capsule roughy two mm in diameter and containing the hydrogen isotopes deuterium and tritium, such as the one shown in the figure, is compressed until it reaches such a high pressure that the hydrogen atoms begin to spontaneously fuse, forming larger atoms and releasing their latent energy of fusion. The eventual hope is that this can be done efficiently enough to make this a commercially-viable energy source. In order to do so, the hydrogen must be compressed by roughly a factor of 1,000, bringing it to a pressure above 10 Gbar, or ten billion atmospheres.

Figure 1.6: An ICF fuel pellet. The pellet consists of a thin, spherical plastic shell filled with a mixture of the hydrogen isotopes deuterium and tritium. Photo credit: LLNL Science and Technology Review [30]

1.2.2 HED facilities

The production and study of HED phenomena in the laboratory requires some method of delivering sufficient energy to the system on a sufficiently-short time scale. In practice, there are only a few methods capable of doing so, and pulsed laser technology is one of the most widely used. The available technology surrounding such lasers is also the primary technique I used to perform the work described in this dissertation, not only to create the physical systems, but also to run the primary diagnostic used to obtain information about these systems: X-ray radiography. Many diverse laser facilities exist worldwide enabling HED experiments, each of them possessing unique characteristics that make them particularly suited for HED systems with certain properties. In the United States, a number of such facilities exist with the primary goal of contributing to the national ICF energy effort. The work described in this dissertation was performed at three of these facilities, and I will describe them briefly.

The OMEGA-60 [9] laser at the Laboratory for Laser Energetics (LLE) in Rochester, NY was used to perform the experiments described throughout Chapter III and in Section 4.3. A schematic of OMEGA-60 is shown in Fig. 1.7. This laser operates by
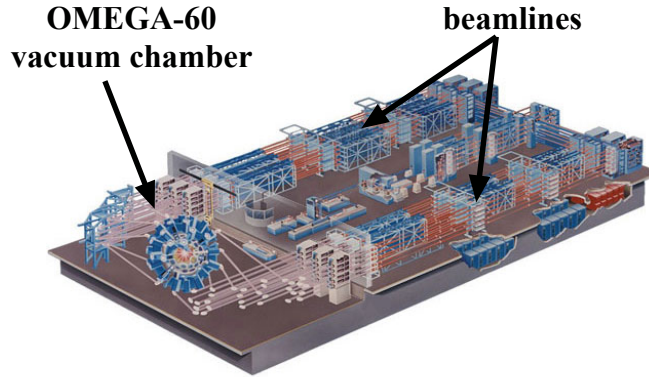
Figure 1.7: A schematic diagram of the OMEGA-60 laser. The laser drivers, amplifiers, and beamlines for the 60 beams are shown leading to the vacuum chamber, where the experiments actually occur. Adapted from LLE facility documents.

forming and amplifying an initial pulse, of wavelength 1053 nm from a Nd:glass laser, that is then split, further amplified, and then split again into 60 beams providing light at a wavelength of 351 nm at a maximum energy of approximately 500 J each in a spot of roughly millimeter diameter, and in pulses that range from approximately half a ns in duration to approximately 4 ns. In fact, the four laser systems described in this section all begin with a laser pulse at 1053 nm (infrared light), which is in some cases then frequency-doubled to 527 nm (green light) and in others frequency-tripled to 351 nm (ultraviolet light). The final beam paths are distributed in a spherical arrangement, leading into a vacuum chamber of roughly 3 meters in diameter, and converging at the chamber's center, where the actual experiments occur.

The OMEGA-EP [60] laser, OMEGA-60's sister facility also located at LLE, has different characteristics, which led me to use it to perform the experiments described in Chapter II and Section 4.2. OMEGA-EP consists of four beams which are actually created by four independent laser systems, allowing significant flexibility in beam timing. Further, two of the beams can be converted into picosecond-length pulses (short pulse) operating at a wavelength of 1053 nm, delivering between 50-800 J, depending on pulse length. Although there are only four beams, their independence,

coupled with their much greater flexibility in pulse duration and energy (from 1-10 ns and up to approximately 4 kJ per laser, at a wavelength of 351 nm) and the short-pulse capability, allows for unique possibilities. The RM experiment described in Chapter II represents a particularly elegant and effective use of OMEGA-EP's capabilities: the long, independent pulses were used to create an unprecedented steady shock while a short, picosecond pulse was used simultaneously to drive a diagnostic without which the experiment could not have succeeded. Fig. 1.8 shows a diagram of the OMEGA-EP laser facility.
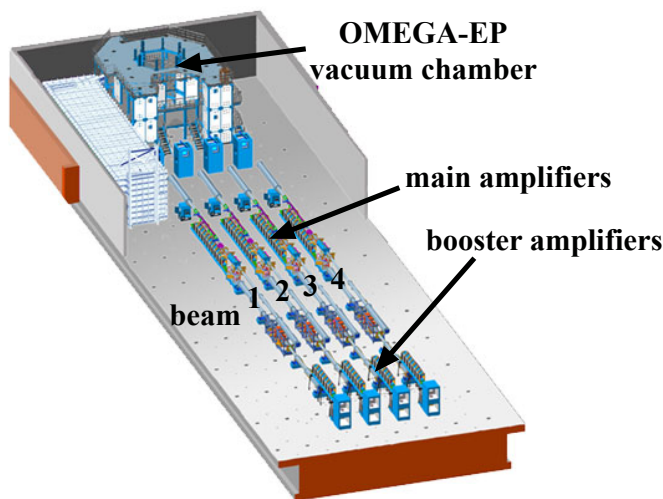
Figure 1.8: Schematic of the OMEGA-EP laser bay. The amplifiers and beamlines for the four lasers are shown leading to the vacuum chamber, where the experiments actually occur. Adapted from LLE facility documents.

The Titan laser, part of the Jupiter Laser Facility (JLF) system of lasers, is a smaller-scale laser located at Lawrence Livermore National Laboratory (LLNL) in Livermore, CA. The experiments described in Chapter V were performed here. Although Titan also has a Nd:glass laser system capable of delivering a 1-kJ, 1-ns pulse, for these experiments we exclusively used Titan's short-pulse capability. This short-pulse laser is capable of delivering approximately 100 J of energy in a 1-ps pulse onto an 8-μm-diameter spot. Although Titan offers less laser power than OMEGA-EP, this facility can be better-suited to certain experiments. Because the system is smaller

and simpler, researchers are permitted much greater flexibility in planning and executing their experiments than at larger facilities, and in addition the laser can be fired many more times in the course of one experimental campaign. From a pedagogical point of view, the fact that the researchers are required to focus and align the laser system themselves, as well as design, install, and maintain the experimental system and diagnostics with the laser's vacuum chamber makes performing an experiment on a laser such as Titan a valuable experience. Fig. 1.9 shows the Titan vacuum chamber during installation of the diagnostic setup for the experiments described in Chapter V.
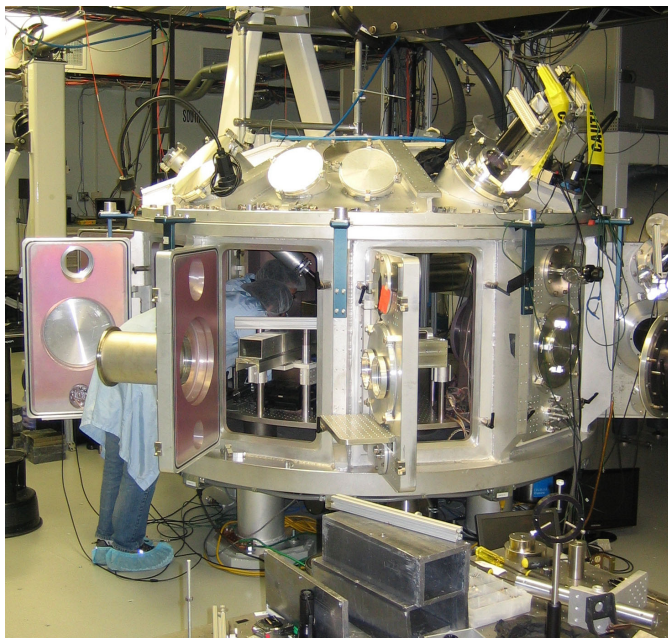
Figure 1.9: View of the Titan vacuum chamber, during installation of the experimental apparatus described in Chapter V.

Finally, the National Ignition Facility (NIF), also located at LLNL, is worth mentioning even though no work described in this dissertation was performed there. The NIF is of particular importance as it is currently the most advanced, highest-power facility of its kind, and as such offers the possibility of extending much experimental HED work, including the experiments described here, in directions not otherwise possible. As an illustration of the immense scale of this facility, its 10-m-diameter

vacuum chamber is shown in Fig. 1.10. The NIF currently permits the delivery of
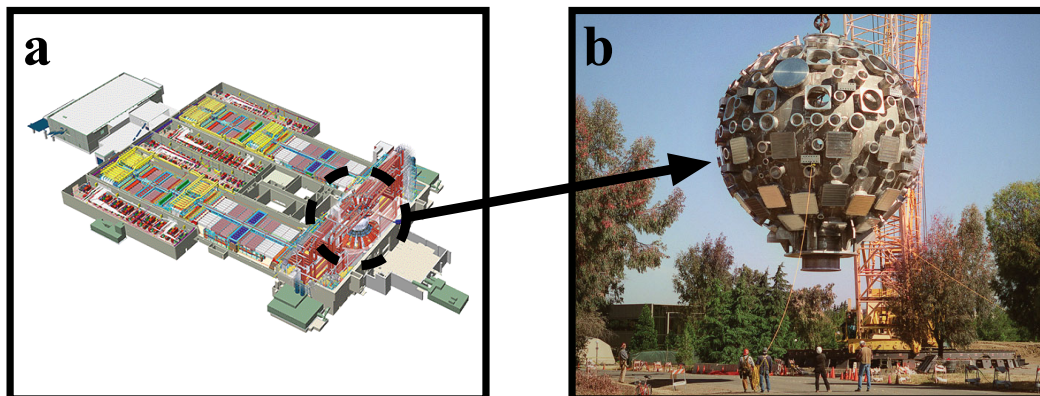
Figure 1.10: a. View of the NIF laser system. The vacuum chamber is highlighted to illustrate the scale of the facility; b. View of the NIF vacuum chamber being installed in the facility. The chamber is 10 m in diameter, three times wider than the OMEGA-60 chamber. Photo credit: LLNL

1.8 MJ of energy through 192 beams, split and then amplified from a single source pulse for uniformity, in a 1-ns pulse. Other pulse lengths are also possible. Unlike at OMEGA-60, however, these beams are not oriented in a spherically-uniform pattern, but are arranged in four circular rings, one at each of two angles about the north and south poles of the vacuum chamber. This is geometrically optimized for the hohlraum ICF concept, in which laser energy is deposited onto the inner walls of a metal cylinder through openings at the cylinder's ends, and the resulting fluorescence from the cylinder is used to heat the fuel pellets. This feature reflects the NIF's primary mission: the development of indirect-drive ICF energy technology.

1.3 Experimental technique

1.3.1 Laser targets

In general, the class of phenomena studied by the experiments in this dissertation are characterized by the action of a shock (or blast) wave at a material interface presenting a density jump, where the shock may be traveling orthogonally to the

interface (in cases where we wish to observe RT and/or RM physics), parallel to the interface (when we wish to observe KH instability), or even at some intermediate angle, if we wish to observe some combination of these behaviors [57]. In all cases, the density jump is accomplished by abutting a piece of plastic, typically either polyimide (PI) or polyamide-imide (PAI), against a piece of carbonized resorcinol formaldehyde (CRF) foam. The physical object is commonly referred to as a target, and this particular plastic/CRF target concept comes with three advantages. First, the surface of the plastic can be easily and precisely machined (to an accuracy on the order of a few tens of nanometers), such that an instability seed perturbation can be created at the material interface of whatever wavelength and amplitude profile is desired. Typical length scales for these quantities are tens of microns for wavelengths, and microns to a few tens of microns for amplitudes. Second, the CRF can be produced at a range of precisely-controlled densities (in the present experiments, the density ranges from 0.05 to 0.4 g/cm^3), allowing the Atwood number of the interface to be accurately determined and varied. Finally, because the initially-solid materials are ionized by the passing shock itself as the experiment commences, the initial conditions are created very cleanly compared to other techniques, even in non-HED systems. For example, shock tubes typically required the use of a membrane and wires (the extra material interferes with the earliest-time behavior) [83] or relied on random or otherwise poorly-characterized initial conditions.

The plastic part, an example of which is shown in Fig. 1.11, is normally produced with an embedded tracer strip. In the figure, the tracer is the horizontal band across the center of the part. The machined seed perturbation described previously is also visible: the finely-spaced vertical striae correspond to the peaks and valleys of the sinusoidal spectrum described in more detail in Section 2.9.1. The tracer strip is created from plastic that has been doped with some higher-Z element (typically iodine or bromine) and density-matched to the surrounding plastic. The higher-Z doping
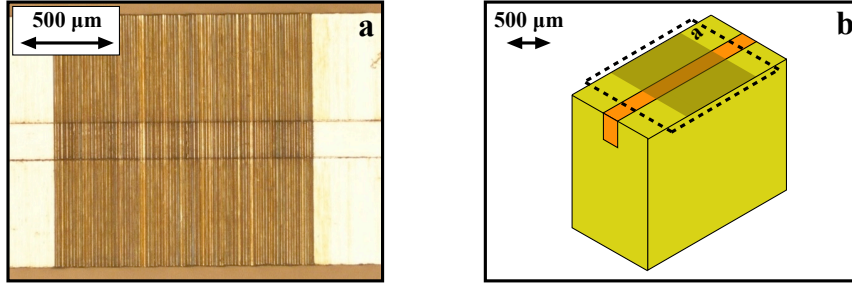
Figure 1.11: a. Photograph of the surface of a machined plastic part, from the RM experiment described in Chapter II. The tracer strip is visible as the horizontal band across the center off image, while the vertical striae correspond to the machined interface perturbation; b. A rendering of the overall part. The dotted lines denote the area shown in Fig. 1.11a, while the shaded area indicates the portion of the surface into which the perturbation has been machined.

causes it to attenuate X rays more efficiently than the surrounding material, thus permitting observation of the system at its center, away from boundary effects such as rarefactions and reflected shocks, while the matched density allows it to behave nearly identically, in a hydrodynamic sense, from the rest of the plastic. Finally, depending on the configuration, the machined plastic part may be directly irradiated by the laser, or a separate plastic ablator may be used.

Use of a tracer brings two major difficulties. First, because of the small sizes of the parts involved, it can be difficult to precisely embed and secure the tracer in the surrounding plastic. Second, doping changes the response of the plastic to elastic stress, which occurs, for example, when an end mill is used to machine the plastic's surface as described above. Considerable effort has been expended over the years to understand these properties, with the result that at present we are able to reliably produce these parts to a very high degree of accuracy.

1.3.2 X-ray diagnostics

The primary diagnostic technique used in these experiments is X-ray radiography. The imaging X-ray source is generated by irradiating a metal foil with another laser

beam or set of laser beams, causing the metal to fluoresce. The particular laser parameters and composition of the foil are chosen according to the frequency and intensity of the desired X-ray source, and the resulting beam of X rays is used to backlight the experimental system. This beam is then imaged by some method, in order to create a coherent view of the system on film or on an imaging plate. Traditionally, this is done by way of a pinhole located either at the X-ray source or at the detector, although in the case of the experiment to be described in Chapter II a spherically-bent crystal [91] was used to image the backlighting X rays. Below, I briefly describe the concepts behind these three techniques, while exact experimental details are described in the corresponding chapters.

The experiment described in Chapter 4.2 uses the technique commonly known as area backlighting. The X-ray source consists of a foil, of some material that will emit photons at a desired characteristic energy, placed some distance from the experimental system and opposite from the detector, which when irradiated produces an extended diffuse, incoherent flash of X rays that backlight the system. The detector consists of a piece of X-ray film and/or an imaging plate, in front of which a pinhole or an array of pinholes is placed. The pinholes allow an image to form on the detector. A schematic of how the diagnostic, detector, and experimental system are arranged geometrically is shown in Fig. 1.12a.

The experiments described in Sections 2.9.1 and 4.2, as well as in Chapter III use the technique known as pinhole or point-projection backlighting. The main difference between point-projection and area backlighting lies in the location of the pinhole. Instead of placing the pinhole in front of the detector, here we place it immediately behind the X-ray source. This is shown schematically in Fig. 1.12b. With collaboration from our group at the University of Michigan, LLNL has developed a technique to quickly and reliably construct these X-ray sources by attaching a foil to a thin plastic substrate, which is then offset by a spacer from a tantalum foil, into which
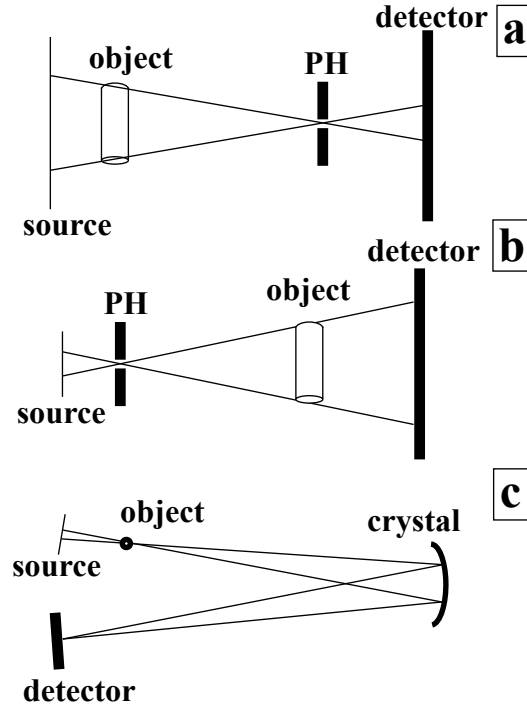
Figure 1.12: Geometrical schematics of three common imaging techniques: a. area backlighting; b. pinhole or point-projection backlighting; c. curved-crystal imaging.

a small hole has been drilled. This pinhole can be drilled to the desired diameter (typically between 10 and 50 μm) and with its axis at a range of angles to the foil normal direction, providing significant experimental flexibility. Furthermore, the pinhole is often drilled in a tapered, conical profile through the tantalum (as opposed to a straight, regular cylindrical profile) offering robustness against slight inaccuracies in either the construction of the backlighter or its alignment during the experiment. An example of an experimental pinhole backlighting source, from the side and front, is shown in Fig. 1.13.

Finally, the OMEGA-EP Spherical Crystal Imager (SCI) was used in the experiments described through most of Chapter II. This diagnostic technique offers significant advantages, the most important being that it allows for much improved shielding of the detector against exposure from stray secondary fluorescence created during the experiment while creating much stronger signal, and therefore contrast in
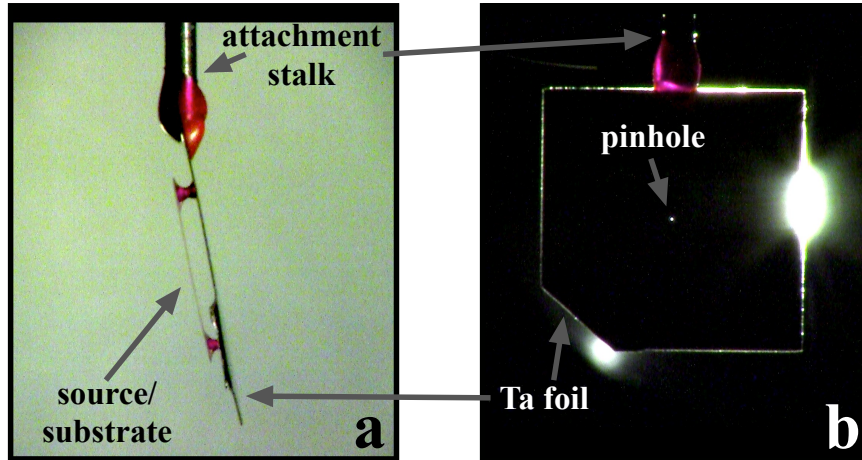
Figure 1.13: A pinhole backlighter, from the side and from the front. a. The side view shows the Ta pinhole with the offset source and source substrate; b. The front view is itself backlit, in order to show the pinhole. The outlines of the attachment stalk and Ta foil can be identified from the light diffracting around the parts' edges.

the resulting data images. This is a direct consequence of the fact that using a reflective crystal to focus the imaging X rays, as shown in Fig. 1.12c, rather than a pinhole (which works by blocking the vast majority of the incident signal) results in much greater signal on the detector. Further, the crystal's Bragg angles cause the crystal to reflect only X rays at the desired energy towards the detector. The drawbacks are that it allows no flexibility in either geometry or backlighter-source photon energy, and as such requires a compatible experimental design.

In summary, aside from their individual features, these radiographic diagnostics have some common features. As a rule, what they measure is X-ray attenuation by material. To the extent that the composition of the materials being imaged are well-known and the X-ray spectrum and intensity of the source is well-known, these radiographic images provide a measurement of the density of the system, integrated along the diagnostic's line of sight. Often, one fluorescence mechanism dominates and the source can be approximated as monochromatic, while the intensity of the source can be calibrated by measuring attenuation through well-characterized fiducial

materials, and the measurement is therefore reliable. Features such as the shock and the material interface can therefore be located due to associated changes in X-ray attenuation across them. Another common feature is that radiography allows one exposure per repetition of the experiment, as irradiation of the source vaporizes it. The ability to produce data is therefore limited by the often-intensive time and resource costs of repeating an experiment, and this factor often becomes an important consideration in experimental planning.

1.4 Chapter summary

I participated in several projects over the course of my career as a graduate student, and the paths that each of the four major projects took turned out to be vastly different. The overarching theme of my experiments, and therefore the expertise that I have developed, has been high-energy-density hydrodynamic instability physics with pulsed lasers as the primary experimental technique. However, with each of the four projects, I got the chance to study a different physical process as well as experience experimental physics at very different stages of the lifespans of long-term projects. Furthermore, in each of these projects, I had the opportunity to collaborate closely with and learn from practicing scientists from several institutions, and of varying levels of seniority. This turned out to be extremely valuable to my development as a physicist. The final project, hot-electron propagation performed on the Titan laser, stands out as well as a learning experience, as it represented a departure from both typical techniques and typical physics practiced in our group. Below, I summarize my work on these four projects.

Chapter II describes work I performed on an experimental campaign studying RM physics. This campaign was performed on the OMEGA-EP laser [60], and pioneered the use of OMEGA-EP's independent, NIF-style beams to create a driving laser pulse whose duration was of a similar length as the time scale as the physics being

studied. I was involved in the development of the campaign from the very beginning, participating in the development of the experimental platform, including the design of the physics, the analysis technique, and the implementation of a novel diagnostic technique to address experimental difficulties introduced by the use of much longer laser pulses than was the case in previous experiments.

Chapter III describes work I performed on an experimental campaign studying KH instability on the OMEGA-60 laser. This was already an established platform when I became involved. Previous work on this platform had created well-defined, observable KH structure, and when I became involved the focus was on understanding smaller-scale and more-complex interface structure due to KH. In this case, I gained valuable experience working on a project in which the foundation work had been performed, and the goal was to investigate more subtle details of the physics.

Chapter IV describes work I performed on an experimental campaign that had, at its core, the study of RT instability. This was a campaign that had been established and successful for many years before I began work on it. The work I describe in this chapter, performed on both the OMEGA-60 and OMEGA-EP lasers, does not concern the instability directly; rather, it takes advantage of two features of these experiments in order to probe the general hydrodynamics of shock-driven systems such as those described throughout this dissertation.

Finally, Chapter V describes an experiment that differs significantly both in experimental technique and in the physics it studies. Whereas the work presented in previous chapters focused on hydrodynamics arising from laser-driven shocks, this experiment investigates the generation of fast electrons by the interaction of short-pulse lasers with solid materials. The main diagnostic was X-ray spectroscopy, and the experiment was performed on the Titan laser at the JLF. The physics involved studies an important detail, described in Chapter V, of X-ray radiography, the primary diagnostic in the instability work that forms the core of my dissertation work. Both

the diagnostic technique and the nature of performing experiments at JLF, however, differ significantly from my main experiences with X-ray radiography at OMEGA, and this experiment added valuable breadth to my training as a physicist.

CHAPTER II

Richtmyer-Meshkov mode coupling under steady-shock conditions

2.1 Introduction

The work presented in this chapter is largely adapted from the papers "Richtmyer-Meshkov evolution under steady shock conditions in the high-energy-density regime," currently under review for publication at *Applied Physics Letters*, and "Observations of late-time, steady-shock-driven Richtmyer-Meshkov behavior in the high-energy-density regime," to be submitted to *High Energy Density Physics*. It is the product of collaboration between myself and Guy Malamud, who designed the theoretical and experimental basis for the experiment [56] and performed all the simulations described here. My role was to take the design, translate it into an executable experiment, and interpret the results.

From the perspective of experimental technique, a highlight of this experiment was my application of a novel diagnostic in this kind of experiment, the OMEGA-EP spherical crystal imaging system (SCI) [91]. Usual imaging techniques were poorly suited to the particular characteristics of this experiment, as will be described in Section 2.9.2, and use of the SCI was critical to the success of the experiment. In addition, my experience has paved the way for at least two other experiments [58, 57],

also relying on this diagnostic, studying other hydrodynamic flows.

2.2 Experimental background

The growth of structure within flowing media is of fundamental importance across a substantial fraction of physics, from superfluidic He [12] to supernovae [14]. In flowing media, shock waves generate structure by several mechanisms when they cross interfaces. One of these, known as Richtmyer-Meshkov (RM) [76, 62], occurs as a consequence of structure on the interface and/or the shock front, by the deposition of vorticity upon shock passage. RM produces structure in many laboratory systems, including gasses [83], liquids [69], and high-energy-density plasmas [1, 20, 59], as well as in natural systems exhibiting shock waves, such as supernova remnants [40]. Control of initial conditions has been a limiting factor in past laboratory studies of RM, which have proven neither able to resolve its earliest-time transient linear behavior [76, 63], nor able to cleanly observe its nonlinear phase during which multiple RM modes couple and the low-density regions (bubbles) merge to form larger structure. The work described here reports on the experimental observations of these two behaviors, both from well-characterized initial structure. These results solidly ground the analysis or simulation of later phases in the evolution of this important process.

Previous RM experiments, including the only existing evidence of RM mode coupling, have mostly been performed in shock tubes. Such experiments have two characteristic disadvantages. First, they have low shock strength, placing the fluid in a regime where drag forces affect the interface dynamics [69, 72]. Second, the initial conditions are substantially uncertain because the interface typically involves a membrane and wires [83], or they are created using a dynamic method, for example by provoking an acoustic standing wave at the interface [69]. The consequence is that one can neither produce a consistent multimode interface, exhibiting clean hydrodynamics at the earliest times, nor easily characterize the initial conditions from which

the observed structure evolves. The few previous experiments to use a laser to create the driving shock wave have mitigated these concerns, but have all been single-mode studies and have involved systems in which the interface was also Rayleigh-Taylor (RT) unstable [29, 75] and/or the structure was strongly affected by interactions with the shock wave [29]. In addition, the prior laser experiments all involved the growth of structure within a region of expanding plasma of variable density, which complicates simulations and invalidates standard analytic analyses, since these typically rely on assumptions of uniform density through the region of growth. In contrast, the present experiments involve only the growth of structure within regions of constant plasma density. These experiments are novel in this respect and also because they produced steady, multimode RM conditions using a well characterized, cleanly-produced multimode initial interface perturbation, free from viscous drag effects. This is an important experimental step in addressing unanswered theoretical questions about the complexities of late-time multimode RM behavior.

The present experiments were designed [56] to take advantage of the capacity of the OMEGA-EP laser facility [60] to generate a sufficiently-long and sufficiently-energetic driving laser pulse that steady shock conditions can be created and maintained for a few tens of nanoseconds–the time it takes the desired interaction to develop. Because the RM growth is seeded by a well-characterized initial interface perturbation, it is possible to develop a precise Fourier analysis of the interface structure. Fourier analysis, in turn, demonstrates the predicted RM physics described in the preceding paragraphs: the linear growth phase as well as the two nonlinear spectral characteristics of mode interaction and mode saturation. This type of analysis has previously been performed on similar systems studying the RT instability [75], but never on an RT-stable, RM-dominant system.

2.3 Theoretical background

If a material interface is seeded with a perturbation consisting of a single sinusoidal mode of initial amplitude $a^\dagger$ and wavenumber k such that $ka^\dagger \ll 1$, the perturbation amplitude a will initially experience a linear growth phase. Immediately after shock breakout, the interface experiences a short transient period, in which the perturbation is first compressed by the shock to an amplitude a_o, and then its growth velocity increases until reaching a maximal, steady linear value U_{RM} [76, 63]. In the simplest approximation [76], due to Richtmyer, this value takes the form $a_o A k u_{\mathrm{int}}$, where A is the Atwood number at the interface and u_{int} is the shocked interface velocity. However, it is well-known that the Richtmyer estimate is only valid under certain conditions, and is often exceeded [63, 104, 105, 106]. If the system is allowed to evolve until ka exceeds about 0.1, the system enters a nonlinear growth phase [105, 106], in which the RM growth velocity begins to decay, and eventually approaches 0 following an asymptotic profile scaling as $(kt)^{-1}$ [33].

If the interface is seeded with two superposed sinusoidal modes k_1 and k_2, each of these will again initially grow linearly (and, consequently, independently) as just described. However, as the modes begin to behave nonlinearly, they will couple and produce harmonics at wavenumbers $(k_1 \pm k_2)$. Still later in time, the modes will begin to compete with each other, and due to the greater asymptotic velocity of the lower-frequency modes [83, 33], they will reabsorb the higher-frequency ones (so-called "bubble merging") on some characteristic time scale dependent upon their relative frequencies.

Finally, if the interface is seeded with many modes $\{k_1, k_2, \ldots, k_i\}$ such that it can be regarded as a spectrum, all of the above behavior will be observed, and in addition, in the bubble-merging phase, the characteristic wavelength should obey a power law in time of coefficient θ, where θ eventually converges to some value. Theoretical predictions place this value at around 0.4 [3, 2].

2.4 The experimental system

The experimental system is composed of four axially-stacked layers of material, shown in Fig. 2.1, with a cross-section width of 1100 μm along the diagnostic line of sight. The first layer, a 125-μm-thick polycarbonate film (the ablator), is pressed
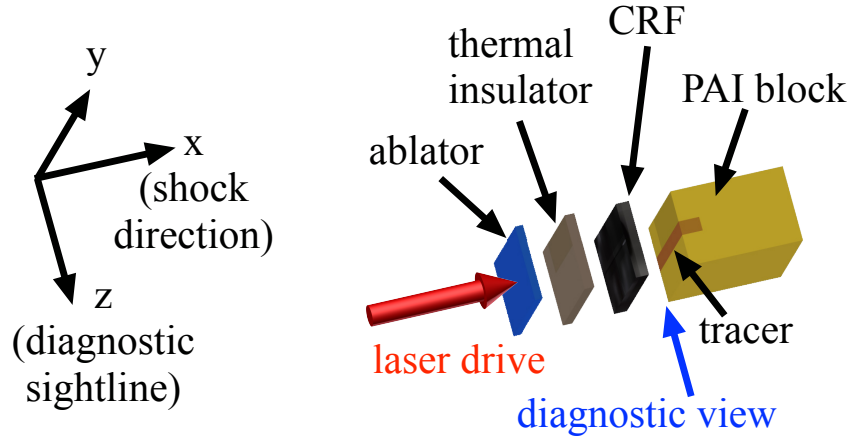
Figure 2.1: Exploded-view rendering of the experiment's physics assembly; red arrows indicate the direction of the laser drive. The axes shown correspond to the axes used in Fig. 2.3.

against a second film functioning as a thermal insulator (TI), made of 150-μm-thick bromine-doped plastic ($C_{50}H_{48}Br_2$). Both layers are of density 1.2 g/cm^3. The purpose of the double layer is to allow the high-Z bromine doping to prevent radiation and high-energy particles, generated by the laser's interaction with the plastic, from propagating through the system and heating the physics-relevant layers in advance of the shock's arrival, while avoiding direct irradiation of a layer including a high-Z material, which would result in the emission of high-energy X rays. Such X rays would both introduce unwanted signal onto the detector and heat the physics-relevant layers. Next, a 200-μm-thick layer of carbonized resorcinol formaldehyde (CRF, of density 0.4 g/cm^3) foam is pressed against the TI, and a block of polyamide-imide (PAI, $C_{22}H_{14}O_4N_2$) plastic, of density 1.4 g/cm^3, is pressed against the CRF. This block features a 200-μm-wide tracer layer of iodine-doped plastic at its center, ex-

tending 300 μm down the system's axis. The higher-Z iodine content of the tracer permits observation of the experiment at the center of the system, away from distorting boundary effects, by attenuating imaging X rays much more efficiently in the tracer than in the surrounding plastic. The interface between the CRF and the PAI block is where the RM growth is produced. A seed perturbation, with amplitude profile $a(y)$, where

$$a(y) = 5\,\mu\mathrm{m} \cdot \cos\left(\frac{2\pi y}{100\,\mu\mathrm{m}}\right) - 2.5\,\mu\mathrm{m} \cdot \cos\left(\frac{2\pi y}{50\,\mu\mathrm{m}}\right),$$

was machined into the face of the PAI block abutting the CRF, resulting in an overall profile with two modes. In one case, the block was machined flat to enable a baseline measurement of the interface. This design, with the shock passing from the lower-density CRF to the higher-density PAI block, enables the RM structure to grow within two uniformly shocked layers, avoiding phase reversal, in which the shock encountering a density *drop* leads to a negative initial growth rate and consequent inversion of the perturbation [76, 63], and growth of structure within a rarefaction. These last two properties were both present in the previous experiment of Glendinning et al [29].

Two ultraviolet OMEGA-EP beams irradiate the ablator in sequence, driving a shock wave into the system, which then crosses the physics-relevant interface about 17 ns later. The energy profile of this sequential irradiation is shown in Fig. 2.2. The beams have a 10 ns, flat-topped temporal profile, with the tail end of the first pulse and the lead end of the second pulse tapered to allow the most stable profile possible during the transition, and a spatial profile of diameter 1100 μm at full-width, half-maximum, smoothed by distributed phase plates, with the intention that the beams' combination effectively behave as a single, long flat-topped pulse. The first beam has an energy of approximately 4 kJ, while the second has an energy of approximately
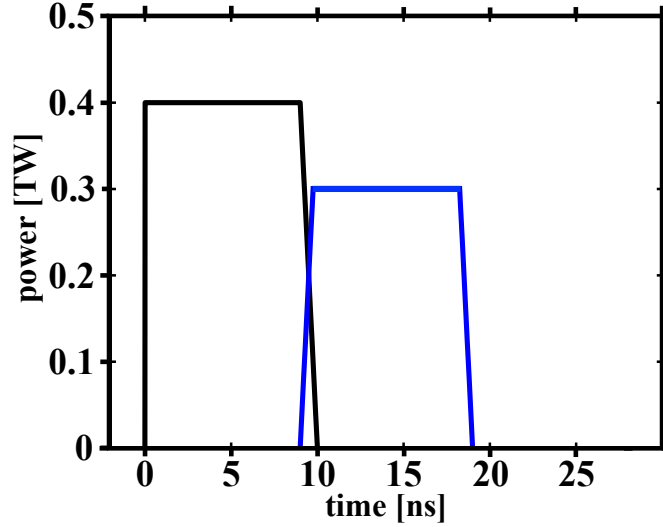
Figure 2.2: Nominal energy profile of the two driving laser pulses.

3 kJ. These energies represent the maximum energies available at the time of the experiment. Because the purpose of the second beam is simply to sustain the ablation pressure on the target, preventing the already-launched shock from decaying into a blast wave, its lesser energy does not significantly affect the shock properties during the window of time in which the system is diagnosed. This property was extensively studied via simulations during the original design [56].

At some time (in this work, 20, 22.5, 25, 30, and 35 ns) following the beginning of the initial driving laser pulse, a third, infrared OMEGA-EP beam, containing 850 J in a 10-ps pulse and defocused to a spot size of diameter 200 μm, irradiates a 20-μm-thick copper foil located 6 mm from the main physics target. This produces a flash of X rays, primarily at the copper K_α energy of 8.0 keV. These X rays backlight the system, and are collected, spectrally-selected, and imaged by the SCI [91], producing a radiograph of the experiment on an imaging plate. More details of this diagnostic are described in Section 1.3.2.

2.5 Results

Examples of experimental radiographs of the perturbed and unperturbed systems, both taken at 30 ns, are shown in Figs. 2.3a and 2.3b, respectively. In both frames
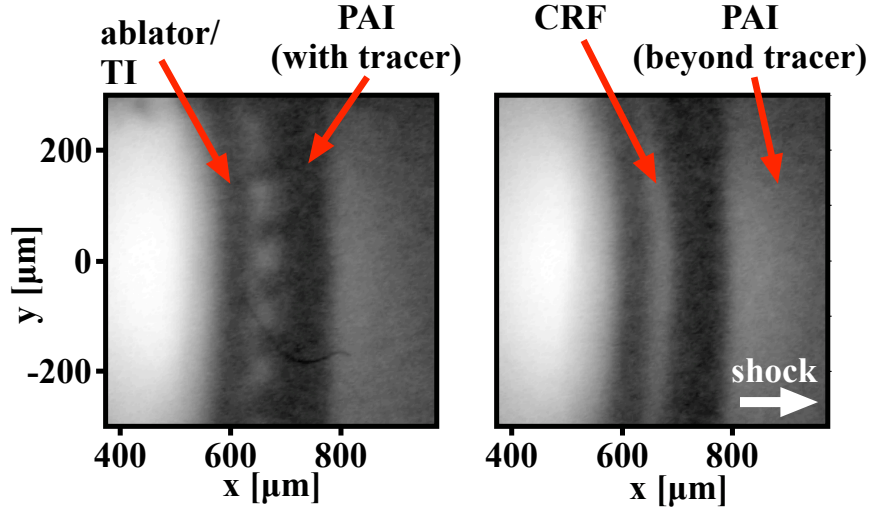
Figure 2.3: a. Experimental radiograph, taken at 30 ns, with an initially-perturbed interface; b. Experimental radiograph, also taken at 30 ns, with an initially-flat interface. The axes in Fig. 2.3a and Fig. 2.3b correspond to the axes used in Fig. 2.1.

the shock is traveling from left to right, and is in the tracer layer at the time the image is collected. (The shock can be identified if the image contrast is optimized for this purpose, at the expense of clarity of the RM physics.) From left to right, the leftmost light-colored area corresponds to the ablation front, the following dark region corresponds to the ablator and the TI, the following thin light region to the compressed CRF layer, the following dark layer to PAI with the embedded tracer, and finally the rightmost light area corresponds to unshocked, undoped PAI beyond the tracer's end. The shock is curved as a result of the ablation-pressure profile produced by the laser beams, and as a result any shocked layer is both curved and compressed. This has led to smaller axial dimensions and a different lateral profile than might be expected from the layers' initial thicknesses, and introduces long-wavelength modes into the system, though we do not expect these to affect the dynamics we wish to

observe on the time scale of the experiment. Finally, in the left frame, the CRF and plastic have clearly interpenetrated via the RM process due to the machined seed perturbation, while the right frame shows the interface's evolution in the absence of this perturbation. The difference in the RM growth between the two cases will be quantitatively discussed presently.

Examples of experimental radiographs, taken at 20 ns and 35 ns, are shown in Fig. 2.4. These two radiographs represent the earliest and latest times at which data
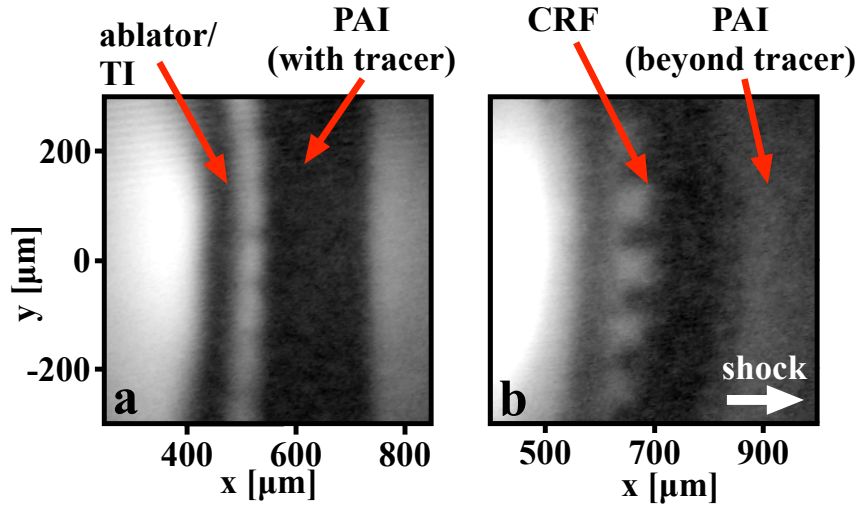
Figure 2.4: a. Experimental radiograph, taken at 20 ns; b. Experimental radiograph, taken at 35 ns. The RM growth of the interface structure during the elapsed time is evident from the two frames.

is available. At 35 ns, the shock has passed out of the tracer layer, and is identifiable in the undoped plastic layer. At 20 ns, the shock can also be resolved, although the optimal image contrast for this would obscure the RM physics we show in the figure.

2.6   Interpretation of the observed one-dimensional flow

The end goal of examining the one-dimensional hydrodynamics is to establish that the necessary conditions for observing clean, purely RM behavior have been achieved. This requires demonstrating that the shock and interface have steady velocities. In

addition, by then simulating the system and reproducing the shock and interface motion correctly, we have confidence that we understand the hydrodynamic properties of the experiment, specifically the equation of state of the various material layers in the system and the strength of the initial driven shock.

Fig. 2.5 shows the measured locations, along with least-squares fits, of the shock and interface from the data. In this figure and in Fig. 2.6, each data point cor-
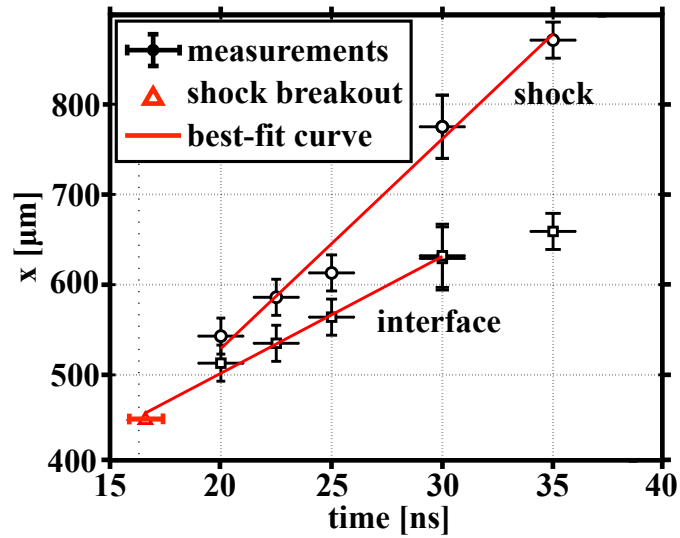
Figure 2.5: The trajectories of the shock and mean interface as measured in the data. Least-squares fits to the data are shown in red, and the extrapolated shock breakout time is shown as a triangle. These quantities' values are listed in Table 2.1.

responds to the measured location from one repetition of the experiment, and the uncertainties reported correspond to the uncertainty in laser timing (horizontal) and the uncertainty in the location of the feature (vertical) in each data point. The trajectory of the shock supports a straight-line fit very well, indicating that we have driven a steady shock as we expected. From the shock positions, we are able to extrapolate a breakout time, or the time the shock crosses from the CRF into the plastic, shown as an open triangle. Finally, the interface trajectory coupled with the shock breakout time also supports a straight-line fit well, providing further evidence that the one-dimensional flow is steady until at least 30 ns.

The low displacement of the interface at 35 ns, however, warrants closer inspection. Fig. 2.6 shows the same shock (black points) and interface (gray points) data overlaid upon a density map of the experiment in time, obtained from a one-dimensional Hyades [54] simulation of the system. Hyades is a Lagrangian hydrodynamic code us-
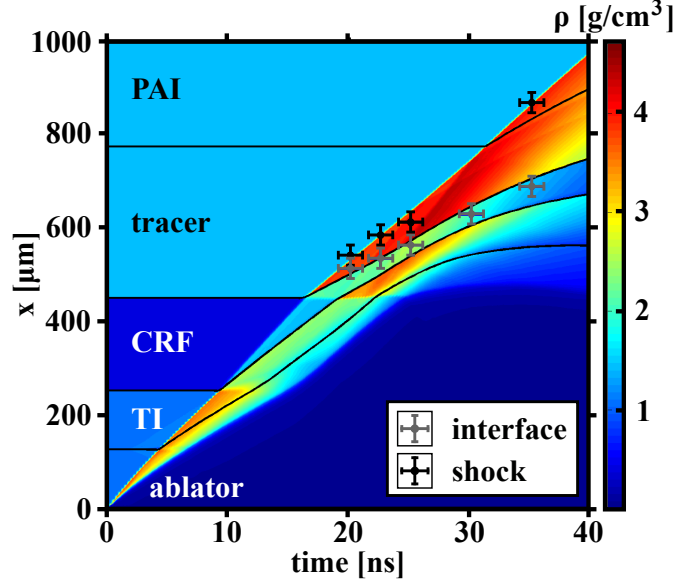
Figure 2.6: Density contour map showing the simulated one-dimensional evolution of the system. The measured locations of the shock and of the RM-relevant interface are overlaid as points, in black and grey respectively, for comparison.

ing multigroup-diffusion radiation transport, single-group, flux-limited diffusive electron heat transport, a laser absorption calculation, and average-atom ionization, tracking total mass density and momentum density and independently solving for the electron and ion temperatures. The simulation used the CH equation of state (EOS) from the SESAME EOS tables developed at Los Alamos National Laboratory, and the simulation's laser conditions were calibrated to reproduce the experimentally-observed shock. In this figure, the shock and the various material layers are clearly identified by the pronounced density jumps associated with them. Although the shock retains a steady velocity until 40 ns, as evidenced by its straight trajectory in time, the interface velocity begins to fall off around ∼33 ns. This indicates that,

Table 2.1: Properties of the one-dimensional flow, both of relevant velocities and of relevant interface parameters. Shown in the upper row are the incident and transmitted shock velocities u_{is} and u_{ts} as well as the shocked interface velocity u_{int}. Shown in the lower row are the shocked interface Atwood number A_{PS}, the Mach number M, the pressure P, and the interface shock breakout time t_{s}.

	u_{is} [μm/ns]	u_{ts} [μm/ns]	u_{int} [μm/ns]	
measured		23.2$\pm$ 1.6	12.9 $\pm$ 0.6	
simulated	28	21.5	14	

	A_{PS}	M	P [Mbar]	t_{s} [ns]
measured				16.6 $\pm$ 0.8
simulated	1/3	8	2.85	16.3 $\pm$ 0.3

according to the simulation, the rarefaction associated with the disappearance of the ablation pressure as the driving laser pulse ends has propagated through the system and reached the interface around that time. Therefore, we *expect* that the interface location at 35 ns will not support a straight-line fit, and exclude it from the calculation. The RM growth is, in consequence, no longer occurring under strictly steady conditions beyond $\sim$33 ns, although at 35 ns we expect the discrepancy to be small due to the short elapsed time since arrival of the rarefaction. In future experiments, we can readily extend this time limit by adding OMEGA-EP's fourth beam to the end of the driving laser pulse, lengthening the pulse by about 50% and adding several nanoseconds of steady interface motion [56].

For reference, Table 2.1 contains a summary of the RM-relevant properties of the one-dimensional flow as measured in the experimental data where possible, as well as those and other relevant properties as predicted by the simulation. In this table, the Mach number M is that of the incident shock, or the ratio of the incident shock velocity u_{is} to the sound speed in the CRF, and the Atwood number A_{PS} is the ratio of the difference between the densities of the shocked plastic and CRF to their sum. The reported uncertainty of the quantities found by least-squares fits are the quantities' associated standard deviations, while the uncertainty of the simulated

shock breakout time corresponds to an artificially-wide simulated shock front that takes time to traverse the interface. This artifact arises from the numerical methods used by the simulation and the consequent limited resolution of the shock front.

2.7 Analysis of observed Richtmyer-Meshkov structure

In order to extract the mode amplitudes from the data, the images were first processed by applying a Gaussian smoothing function over a small number of pixels, less than the resolution limit (roughly 10 μm) of the diagnostic, in order to eliminate small-scale noise, on the order of a few microns, in the images. The material interfaces, identified by steep intensity gradients in the images, were then sharpened using the unsharp-mask filtering technique [19, 58]. To do so, the image is first blurred using a two-dimensional Gaussian filter, and then the blurred image is subtracted from the original. Mathematically, the pixel-by-pixel operation to obtain the unsharp-mask image I_{USM} is expressed as

$$I_{\mathrm{USM}} = I_0 - I_0 \otimes \frac{1}{\pi R^2} e^{-\frac{(x-x_0)^2 + (y-y_0)^2)}{R^2}} \Delta x \Delta y, \tag{2.1}$$

where the second term is the convolution of the matrix I_0 with a matrix having the Gaussian form on the right. In this equation, I_0 is the original image intensity value, Δx and Δy are the pixel dimensions (here, 2.5x2.5 μm), and R is the Gaussian radius over which the filtering is applied, and x_0 and y_0 are the spatial coordinates of each given pixel. A value of R=20 μm produced the optimal sharpening for our data. In the processed image, the contours of value zero then correspond to the locations of the material interfaces. An example of this process is shown in Fig. 2.7, for the 35-ns data from Fig. 2.3b. In this figure, the zero contours are highlighted using black lines, while the color-mapping has been converted into a binary form; that is, all pixels where $I_{\mathrm{USM}} > 0$ have an identical darker color, while all pixels where
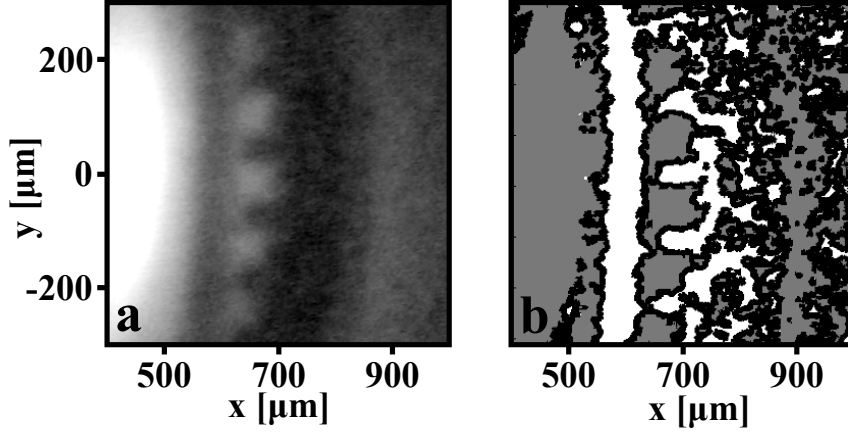
Figure 2.7: a. Experimental radiograph, taken at 35 ns; b. Unsharp-mask filtering of the same radiograph, with the midway contour indicated by black lines.

$I_{USM} < 0$ have an identical lighter color. The unsharp-mask process is most effective and accurate when the structures involved are thick compared to the pixel size, and when the overall intensity change is large. Thus, the unsharp mask picks out the CRF/ablator and RM-relevant interfaces well, and the shock somewhat less well. There is significant artifact present in areas of low intensity in the image, due to the greater relative magnitude of characteristic noise fluctuations in such locations.

The contour exhibiting RM growth is then extracted, and Fourier analysis is used to obtain the spectral content of the interface. The spectral decompositions of such contours, from the images previously shown in Fig. 2.3, are shown in Fig. 2.8. In Fig. 2.8, the length of contour sampled is the central 400 μm; therefore, the wavenumbers l shown correspond to wavelengths λ given by $(400\,\mu\text{m})/l$. The original modes, using this convention, correspond to $l = 4$ and 8 for $\lambda = 100\,\mu$m and 50 μm, respectively. In the spectrum from the initially-perturbed system, in addition to the original modes, the development of a coupled harmonic (l=4+8=12) is clearly observed, along with another higher-order mode (l=12+4=8+8=16). Meanwhile, the nominally-flat system exhibits comparable growth to the perturbed one in modes that were not seeded, while exhibiting much less growth in the seeded modes. Error in the mode amplitudes is estimated by considering growth measured on the initially-flat interface shown in

36
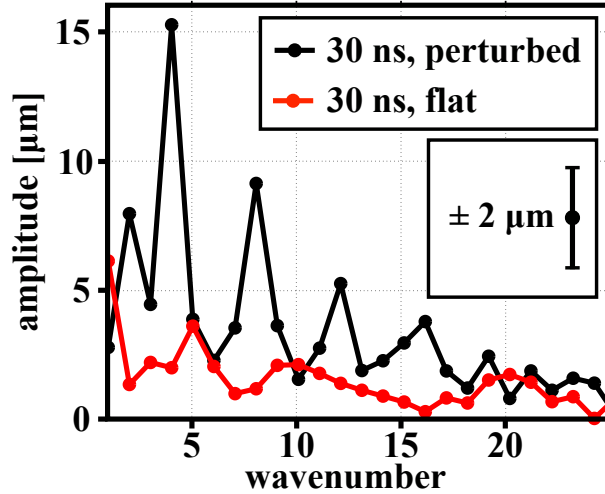
Figure 2.8: Fourier transform of the perturbed and flat contours at 30 ns, correspond-
ing to the data shown in Fig. 2.3. The growth of the fundamental modes
$l=4,8$ plus the appearance of the harmonics $l=12$, 16 are evident.

Fig. 2.3b. This method demonstrates how much of the spectral components at later
times is specifically attributable to the effects of the machined seed perturbation, and
what portion is secondary structure due to other hydrodynamic processes occurring
at the interface. Finally, to illustrate the full behavior of the interface, a time se-
quence of the full spectrum is shown in Fig. 2.9. The spectrum at 22.5 ns is excluded
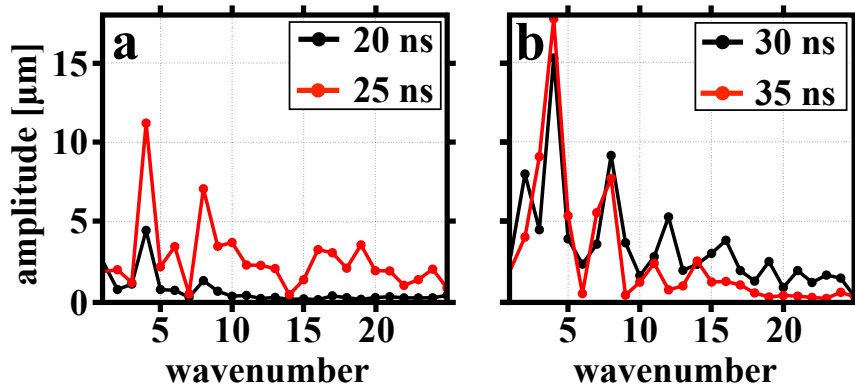
Figure 2.9: Time evolution of the full interface spectrum. a. Spectrum at 20 and 25
ns; b. Spectrum at 30 and 35 ns.

to preserve the equal time intervals between curves, as well as for clarity in the figure.

By performing this technique on data at all existing times, and extracting the
amplitudes of the modes of interest at each time, we can reconstruct the system's

37

temporal evolution. In the two frames in Fig. 2.10, the solid lines show this evolution for the 4, 8, and 12 modes (i.e. the fundamentals and the first harmonic) in time, as measured in the experiment.. Fig. 2.10a plots this evolution in real time, while Fig. 2.10b plots it nondimensionally, scaled relevant to each mode. Results from
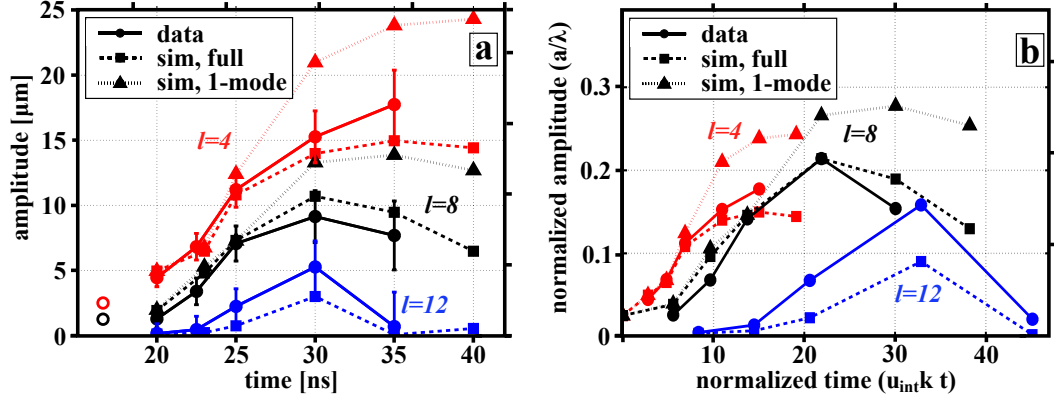
Figure 2.10: Time evolution of the two fundamental modes (l=4, 8, shown in red and black, respectively), plus one harmonic (l=12, shown in in blue), showing their growth and early saturation behavior. The solid lines correspond to data, the dashed lines to full simulation output, and dotted lines to output from a one-mode simulation seeded with only the relevant mode. a. The time evolution plotted in real time; b. The same time evolution, plotted in a nondimensionalized form scaled relevant to each mode.

simulations of the experiment are also presented in Fig. 2.10, and will be discussed in subsequent sections.

At around 17 ns, the passing shock compresses the interface perturbation to roughly half its initial amplitude [76]. This postshock amplitude, a_o, can be estimated analytically from Richtmyer's theory as

$$a_\text{o} = a^\dagger (1 - \frac{u_\text{int}}{u_\text{is}}), \qquad (2.2)$$

and is plotted as open circles in Fig. 2.10. From 17 ns until around 25 ns, the fundamental modes grow independently and linearly, and the new harmonic is not yet observed. In the earliest phase, from 17 ns to approximately 22.5 ns, the growth rate exhibits transient behavior, ramping up to a maximum linear value achieved

between 22.5 and 25 ns, corresponding to a value of a/λ of roughly 7-13%. Although it is difficult to produce a reliable measurement of this maximum growth rate based on the two data points present, the overall contour of the amplitude plot suggests that the growth rate must, at some point during the linear phase, be significantly larger than the theoretical rate U_{lin} predicted by Richtmyer to be

$$U_{\mathrm{lin}} = A u_{\mathrm{int}}(k a_{\mathrm{o}}), \tag{2.3}$$

or roughly 0.73 μm/ns based upon the parameters in Table 2.1. This is consistent with previous observations that shock conditions such as ours tend to produce a departure from Richtmyer's predictions, while other approximations for an observed linear rate are empirical in nature, and do not provide much insight into the physics at work [100]. Around 25 ns, the harmonic mode $l = 12$ appears which, along with the decrease in growth rate of the original modes after 25 ns, indicates that the original modes are coupling. At later times, beyond ~ 30 ns, the higher modes are observed to begin decaying. This indicates that a third behavior is influencing the dynamics: bubble merger, as the faster-growing low modes are now overtaking the higher ones. A caveat to this is that, as seen in Fig. 2.6, the density of the shocked foam supporting the interface motion begins to decay between 30 and 35 ns, indicating that by 35 ns the shock conditions are no longer strictly steady.

Error in these measurements is estimated by considering, in our earliest-time data image, the measured growth of the non-fundamental modes, since they should not have had any time to develop. At late times, the procedure described for Fig. 2.8 was used, and a linear fit to these two results was used at other times. These uncertainties largely result from systematic difficulty in making Fourier measurements of the interface, and as such are likely consistent from data point to data point. Furthermore, the overall temporal amplitude contour is self-consistent, indicating

that the observed phases of RM behavior are qualitatively present, regardless of the accuracy of any given amplitude measurement.

2.8   Simulation support of the experimental results

To confirm that mode coupling is responsible for the observed effects, we wish to compare the growth of the coupled fundamental $l = 4$ and $l = 8$ modes to their growths in isolation from each other. We do not possess full, single-mode data sets of this system, and therefore performed simulations in order to observe these differences. The simulated system was initialized using the 1D Hyades simulation described in Section 2.6.

The steady-shock jump conditions obtained from the Hyades simulation were then used to perform two-dimensional simulations [56] of the experiment using Dafna [43, 67], a multi-material HLLC (Harten-Lax-van Leer-Contact)-based [97] code, with interface tracking and AMR (Adaptive Mesh Refinement) capabilities [8]. The interface contours were then obtained from the simulations, and then were analyzed using Fourier techniques, similarly to the experimental analysis previously described. The growth of the fundamental modes from a full two-mode simulation is plotted in Fig. 2.10 as heavily-dotted lines with square points, while the growths from the two single-mode simulations, with $l = 4$ and $l = 8$, are shown as finely-dotted lines with triangular points in Fig. 2.10. The growth of the $l = 12$ harmonic, from the two-mode simulation, is also plotted. (In the single-mode cases, each mode does create higher-order harmonics with itself, 4+4=8 or 8+8=16, but the harmonics' growths of ~ 0.5 μm are not observable on the time scale of the experiment.)

The simulation results support the validity of our interpretation of the experimental observations in several ways. First, the overall amplitude contour of the data is preserved in both simulations until the maximum linear growth rate is achieved. From there, the two-mode behavior becomes nonlinear around 25 ns, suggested by

the decay of the growth rate after that time as well as the appearance of the 12 mode, which can only occur due to interference between the two original modes. The time scale for this is sensible, as existing work tends to predict nonlinearity when the system reaches an amplitude-to-wavelength ratio of $a/\lambda \sim 0.1$ [105, 106, 63]. However, it is interesting to note that the divergence of the data and two-mode simulation from the single-mode simulations seen in Fig. 2.10 appears to suggest that, in the absence of mode coupling, the linear growth rate should persist significantly longer in this system than this scaling predicts.

2.9 Multimode physics

2.9.1 The multimode experiment

In a separate experiment, a system similar to the one described above was driven, but in this case the plastic was machined with a 60-mode seed perturbation, described by

$$x(y) = \frac{a_0}{k_{\max} - k_{\min}} \sum_{k=k_{\min}}^{k_{max}} F(k) \cos\left[k\pi\left(\frac{y}{L} + \phi\right)\right], \qquad (2.4)$$

where, for each k, $F(k)$ was randomly assigned an integer value of either ± 1 and ϕ was randomly assigned a value on the range [-1,1], and the wavelength/amplitude spectrum was defined by $k_{\min}$=40, $k_{\max} = 100$, and a_0=10 μm. This multimode perturbation was chosen such that its collective behavior would approximate that of a continuous spectrum, as described in Section 2.3. This experiment was diagnosed using the point-projection backlighting technique, rather than the SCI described previously, in which a nickel foil was irradiated by a third ultraviolet OMEGA-EP beam, producing a flash of X rays at the Ni He-α energy of 7.8 keV, and a 10-μm-diameter pinhole was placed at the source to create a beam from these X rays. The system was imaged by an X-ray framing camera, and recorded on film. Point-projection imaging is discussed in more detail in Section 1.3.2.

Data obtained roughly 10 ns following shock breakout is shown in Fig. 2.11. The
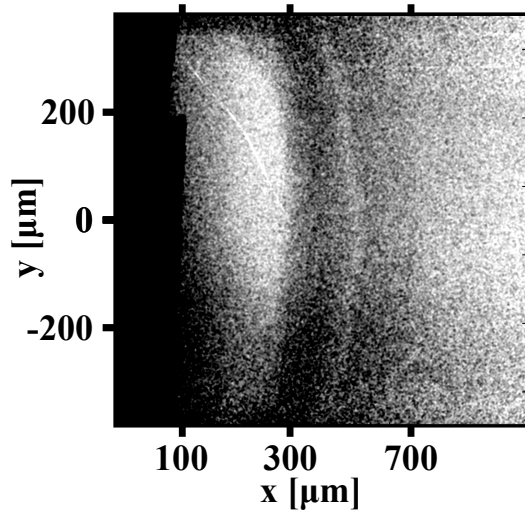
Figure 2.11: Experimental radiograph, taken at 30 ns, of the 60-mode system described in Section 2.9.1. The same one-dimensional flow features as in the date shown in Fig. 2.3 are visible, although identification of the two-dimensional RM physics requires careful use of of Fourier analysis.

same one-dimensional flow structure can be identified in this image as in Fig. 2.3; however, the contrast is poor and the size scale of the noise structure in the image is much larger. These issues are discussed further in 2.9.2. This makes it impossible to identify the RM bubble structure by eye, and we must rely on the Fourier technique outlined elsewhere in this chapter to detect it. In some sense, the two-mode experiment described previously serves, for the present case, as a demonstration of the validity of this Fourier technique due to our ability to corroborate our spectral measurements by direct inspection.

Fig. 2.12a shows the processed deconvolution of a 400-μm-long segment of the RM-relevant interface, done using the same unsharp-mask method described in Section 2.7. The contour at the TI/CRF interface provides another clue that the Fourier technique is valid: despite the relatively large-scale structure present in the image, the image-intensity contour picks out a straight line at this interface. This is what we expect to find, as the TI/CRF interface was initially smooth, and we therefore expect no
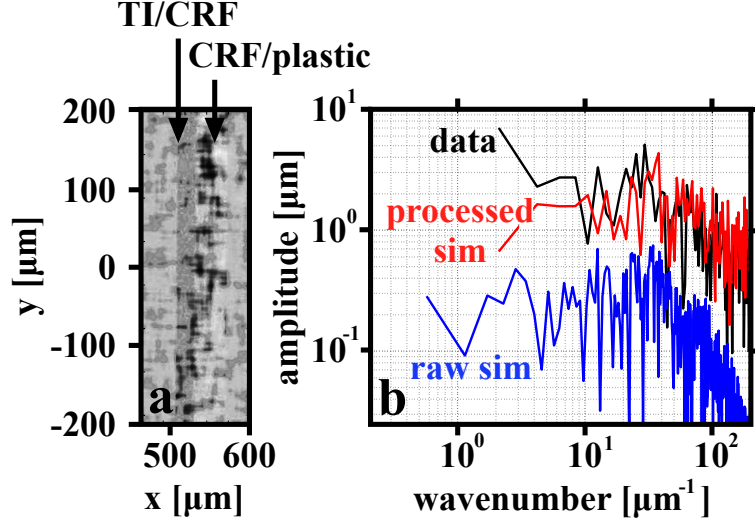
Figure 2.12: a. Unsharp mask of the 60-mode system. The unsharp mask picks out the the CRF/TI interface as flat, but not the CRF/plastic interface; b. Fourier transform of the RM-relevant interface in Fig. 2.12a in black, along with the equivalent Fourier transform of the simulated system, including simulated diagnostic effects, in red and the Fourier transform of the raw simulation output in blue.

structure to grow there. The contour of the perturbed CRF/plastic interface, on the other hand, does show structure. The Fourier spectrum of the CRF/plastic interface is shown as the black curve in Fig. 2.12b, alongside spectra from a simulated system [56]. The blue curve corresponds to the contour of the direct simulation output, while the red curve corresponds to a contour that has been processed to simulate artifacts of the diagnostic's limitations and analysis procedure. This processing was done as follows. First, the CRF and plastic areas in the 2D-simulation output are calibrated to the signal levels seen in the experimental radiograph. Next, we apply a moving-average smoothing filter with a 10 μm $\times$ 10 μm area to the image, to simulate blurring due to the resolution limit imposed by the finite size of the backlighting pinhole. Finally, we add multiplicative noise having a variance of the inverse of the signal-to-noise ratio (SNR) observed in the data, and then recover the contour using the same procedure described for the data. Signal issues are discussed in more detail in Section 2.9.2.

It is difficult to draw a conclusion about the physics from such limited data;

however, the result and our ability to reproduce it numerically suggest that our understanding of the underlying processes is sufficient to use this as a basis for further exploration of the physics. First, as in the examination of the one-dimensional flow discussed in Section 2.6, the fact that we are able to numerically reproduce the experimental results is a good indicator that the assumptions we make about the driving physics are valid and, equally important, that we understand the details of the information that our diagnostic provides about the experimental flow. Second, the experimental result validates the analysis method we prescribed for the RM physics [19, 56]. This is possible because the length of interface we sample is sufficiently large that there is a statistically-significant presence of RM-bubble information on top of the random noise artifacts. With further data, we should be able to make the measurements we originally set out to. Finally, the slope of the spectrum at $k \gtrsim 3$ is consistent with our prediction that we should observe mode saturation at those wavelengths, while the relatively-low Atwood number for this experiment means we expect some symmetry between the RM bubbles and spikes, and hence that we can track the bubble height with some accuracy from the overall width of the structure at the interface. Further data points, especially the collection of a time series of radiographs, would allow us to establish these measurements with more confidence. The vastly-improved image quality possible with current radiography techniques would also bolster our confidence in these measurements.

2.9.2 Diagnostic details

The introduction of the long drive ($\sim$20 ns) into this experiment poses several diagnostic challenges which make it difficult to employ traditional imaging techniques, such as point-projection backlighting. First of all, the extended length of the driving pulse causes secondary fluorescence to occur at the expanding ablation front, which will saturate the detector absent some manner of shielding. Second, the sustained

ablation pressure due to the long drive pulse prevents the system from rarefying, which causes the densities at the RM-relevant interface to be higher. Finally, the CRF density of 0.4 g/cm^3 needed to create the desired physics is high compared to many other similar experiments, which have typically used CRF of density between 0.05 and 0.1 g/cm^3. The one-dimensional simulated density profile of the experiment is shown at the imaging time is shown in Fig. 2.13, along with the typical density of a previous experiment. Also shown in this figure is the intensity profile of a line
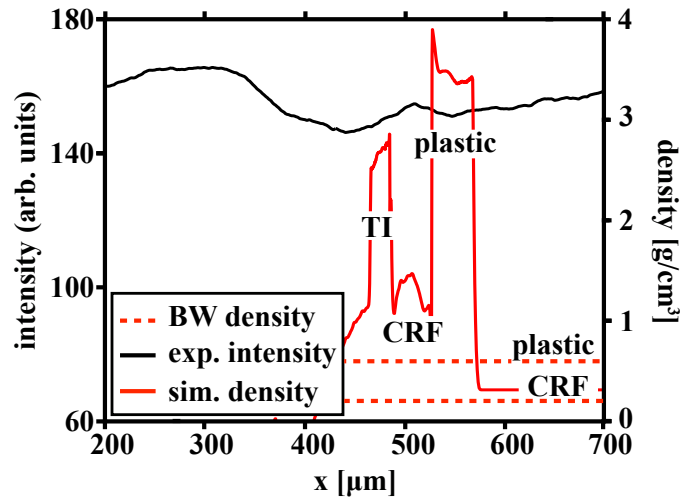
Figure 2.13: One-dimensional simulated density profile of the present experiment compare to typical densities in previous experiments. A line sample of the intensity on the radiograph, taken at $y = -200$ μm, is also shown. The intensity units are arbitrary, but scaled to demonstrate the contrast in the radiograph. Finally, dotted lines show typical material densities in previous blast-wave-driven experiments.

sample along the target axis, taken from the experimental radiograph shown in Fig. 2.11. This line sample quantifies the low contrast that is visually evident in Fig. 2.11, and is due to the diagnostic difficulties described above. Finally, the dotted lines indicate, for comparison, typical material densities in previous, similar experiments initiated with a shorter laser pulse, and in consequence with physics driven by a blast wave (BW) rather than a steady shock. The lower densities permit, from an identical X-ray source, much better signal and contrast in the resulting data.

Typically, the first issue can be solved by using a gated diagnostic, such as the X-ray Framing Camera at the OMEGA-EP facility. However, because of the densities involved, use of a high-enough-Z backlighting material to achieve acceptable transmission through the CRF results in a laser-energy-to-X-ray conversion efficiency too low to achieve sufficient contrast [103]. The result is evident in the data shown in Fig. 2.11. This image has a SNR of roughly 0.7, and noise structure on the size order of several microns. In contrast, a SNR of unity is typically considered the absolute minimum necessary to discern individual features at all, with 5 taken as the ideal minimum offering certainty regarding one's observations [80, 81], a criterion easily met using the crystal-imaging diagnostic.

The new crystal-imaging diagnostic used in the two-mode experiment, examples of which were shown in Fig. 2.3, addresses all of these diagnostic issues through the use of a fundamentally-distinct method of imaging the backlighting X rays. Rather than employing a pinhole, which essentially blocks the vast majority of produced imaging photons in order to create a beam, the curved crystal focuses them directly, and the only limit on the useful signal is the collection area of the crystal itself. Second, because the crystal selects for a particular energy of photons and focuses them to a narrow beam, it is possible to shield the detector in such a way that nearly all unwanted fluorescence is prevented from interfering with the diagnostic. [91]

2.10   Conclusions

The experiment presented in this chapter, as a whole, represents a novel use of contemporary laser and diagnostic capabilities to probe hydrodynamics under conditions not previously achievable. The results demonstrate our ability to create, diagnose, and measure RM physics under steady HED shock conditions deeply into the nonlinear regime, where mode interactions strongly affect the dynamics. The results with the SCI diagnostic indicate that we have accomplished our goal of cleanly

producing and measuring these physics, and in particular that we were able to observe the presence of three important theoretically-predicted aspects of RM physics: early-time transient behavior of the growth rate, nonlinear mode interaction producing new modes, and the growth and saturation of those modes over time. The first of these has not previously been observed, while the others have not been observed from precisely-characterized initial conditions under steady shock dynamics. Our experience with the multimode initial perturbation shows that the analysis technique we developed has promise in exploring more-complicated and less-clearly-resolved interface structure, due to the statistical effect of measuring an interface that is long compared to the length scale of noise and other artifacts in the data.

Further, the experimental platform presents several directions in which the results presented here can be extended. For example, current OMEGA-EP laser performance allows for the opportunity to increase both the power and temporal duration of the driving laser pulse, which would enable the extension of the steady shock conditions by roughly 5 ns and allow the probing of RM structure further into its development. Also, the initial mode combination chosen for the present experiment represents the simplest conditions producing the desired physics, and more complex initial conditions, such as a multimode perturbation with wavenumber-dependent amplitude [56, 96], could offer more detailed expression of these physics, including the possibility of pushing the system to self-similarity in a manner that could be measured statistically from the Fourier spectrum at the interface, while simulations suggest that simpler, single-mode conditions could extend the linear phase and allow a more reliable quantitative measurement of the linear growth rate.

CHAPTER III

Mixing-zone growth due to Kelvin-Helmholtz instability

3.1 Introduction

The work described in this chapter is an adaptation of the paper "Observation and modeling of mixing-layer development in high-energy-density, blast-wave-driven shear flow" [18], published in *Physics of Plasmas*. My role in this work was twofold. In the experimental planning process, I designed a target package, to support the existing OMEGA-60 Kelvin–Helmholtz (KH) experimental platform [37, 32], that could be fabricated entirely in-house and led the portion of the experimental campaign in which these targets were shot. Following the experiment, I developed the vorticity-deposition reasoning used to identify the appropriate physics for modeling the observed interface structure.

3.2 Experimental background

Shear-flow hydrodynamics, especially those arising in shocked systems, are important processes in high-energy-density (HED) physics, both for the effects they introduce in technological applications such as inertial-confinement fusion [25] and for their role in the evolution of natural phenomena, such as expanding nebulae [7]

and solar dynamics [71]. When an interface between two materials in a system with shear flow exhibits perturbation or imperfections, the shear flow introduces vorticity at the location of those perturbations. This can lead the interface to become KH unstable, causing the perturbations to grow in size and the two materials to interpenetrate, and eventually driving the flow to a turbulent state. The region in which the fluids interpenetrate is known as the mixing zone (MZ). Traditional experiments [69] have proven able to study KH, as such, only at Reynolds numbers insufficiently high to permit an evolution towards turbulence [21], which requires a Reynolds number in excess of $\sim 10^4$. Other traditional experiments, studying turbulence in shear flows produced using splitter plates [11], have achieved higher Reynolds numbers, but have proven unable to isolate the KH phase of the evolution. The development of HED facilities, such as the OMEGA laser facility [9], permits the study of KH in the plasma state with shear velocities at least an order of magnitude greater than that of the splitter-plate experiments (tens of km/s versus a few km/s) and with better-known initial conditions. Shear flow under these conditions better represents the relevant hydrodynamics in the previously-mentioned systems of interest.

The first such experiments [32, 38], performed at the OMEGA laser facility, took advantage of an initial well-characterized, single-mode sinusoidal interface perturbation to seed ordered, readily-observed, individual interface vortices. These vortices are the fundamental building block of more-complex shear instability behavior, and the significance of those experiments lies in the direct vortex measurement they achieved. More recent experiments have been performed on the same platform, but taking a different approach with respect to the initial interface conditions [89, 90]. The interfacial surfaces of the parts used were nominally machined flat, so that the KH-seeding perturbations were surface roughness arising from inherent imperfections in the machining process. This roughness was on the order of 100 nm in size. This work then examined the performance of a simulated turbulence model in predicting

experimentally-observed growth [39].

An important point about the relative behavior of the shear flow in these two experiments is that the blast wave has introduced two complications into the hydrodynamic behavior. Firstly, the shock front creates circulation by means of baroclinic vorticity deposition (via the cross product of the gradients of pressure and density). Secondly, because the velocity of the post-shock flow decreases behind the shock front and eventually reverses, shear-driven vorticity deposition only proceeds in the initial direction for a limited period in time and space. As we discuss further below, the consequence is that vorticity deposition in the initial experiments [32, 37] is dominated by baroclinic effects while that in the later experiments is dominated by shear-flow effects. These two mechanisms are distinct in origin, but result in similar physical observables, and so we have chosen to refer to them as two aspects of KH, rather than as two distinct processes. We will refer to these two mechanisms comprising KH as sustained shear (S) vorticity deposition and baroclinic shock (B) vorticity deposition.

Motivated by this observation, we have performed further rough-interface experiments with the purpose of studying the initial interface conditions carefully, in order to understand the mechanism responsible for growth. We present here an analysis of these initial conditions, and of the effects we expect them to have on the system's KH behavior. We have also performed simulations, calibrated to the experimentally-observed flow, intended to provide insight into the system's hydrodynamics as they evolve prior to imaging. Finally, we use the combined results of our interface analysis and flow simulations to test the correspondence of the observed interface growth to the growth predicted by a purely-hydrodynamic model of the system.

3.3 The experiment

3.3.1 Experimental conditions

The experimental system is created by abutting a block of carbonized resorcinol formaldehyde (CRF, of initial density either 0.1 g/cm^3 or 0.05 g/cm^3 with a 1-mm-square cross section) foam against a block of plastic (polyamide-imide, $C_{22}H_{14}O_4N_2$, initial density 1.4 g/cm^3) 1 mm thick in the diagnostic-view direction. These two blocks are shown schematically in Fig. 5.1a, from the point of view of the diagnostic. The plastic part features a 200-μm-thick tracer layer positioned at the center of the block, in a coplanar orientation with respect to the diagnostic imaging plane. This tracer is doped with iodine, causing imaging X rays to be preferentially absorbed within it, and thus allowing examination of the flow at the center of the target, away from boundary effects. Its density is matched to that of the plastic, such that its hydrodynamic behavior is nearly identical to that of the surrounding plastic. The edge of the tracer is visible in the oblique view of an actual target shown in Fig. 5.1b, while in the Fig. 5.1a schematic the tracer lies in the plane of the figure and behind the visible layer of plastic. A 30-μm-thick polycarbonate ablator, framed by a 50-μm-thick gold washer with an aperture centered upon and of identical cross-section to the CRF, is placed against the end of the CRF block. Finally, thin beryllium walls sandwich the CRF and plastic in the direction of the diagnostic line of sight, to mitigate effects due to lateral expansion of the system in that direction [73]. The physics-relevant parts are shown in Fig. 5.1. The purpose of this geometrical setup is to allow a blast wave to be driven into the CRF, normal to the ablator, such that shear flow is created between the CRF and plastic, at their interface. The resulting KH growth at this interface will be determined by the initial conditions there, which in turn are largely dependent on the topological properties of the surface of the plastic. These will be discussed in detail in Section 3.4.
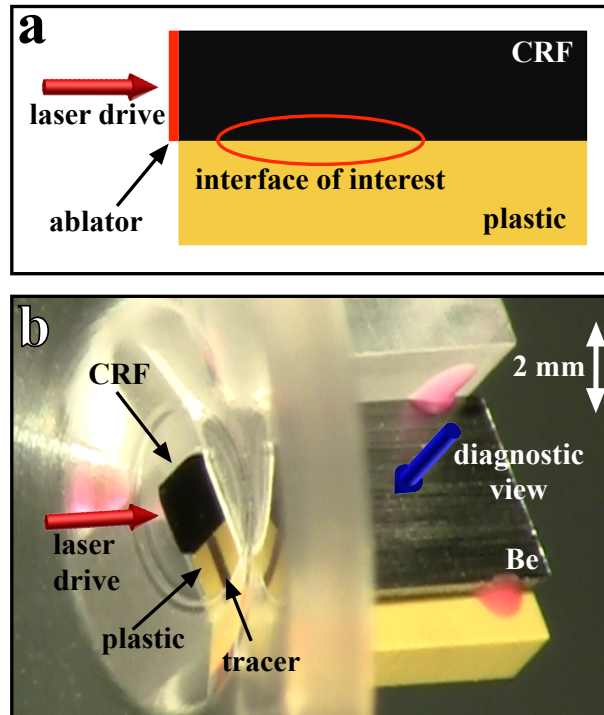
Figure 3.1: a. A sketch of the physics-relevant components, shown from the diagnostic viewpoint; b. An oblique view of an experimental target during the assembly process, showing the surface to be irradiated by the laser and the diagnostic viewing direction. The transparent material is acrylic, used in the assembly of the system. The beryllium wall is also visible, but the gold washer has not yet been placed.

Ten OMEGA laser beams, simultaneous to better than ±200 ps and at an energy of 450 J each, drive a shock wave into this system. The temporal profile of this pulse is a nominally-flat-topped, 1-ns-long square shape, and the beams are spatially smoothed by an SG8 distributed phase plate, producing a spot, of diameter ~820 μm full width of the half-maximum (FWHM), upon the ablator. The fringes of the laser spot are blocked by the gold washer, and a shock wave is thus driven through the ablator towards the CRF, but not directly into the plastic. At the time the driving laser pulse ends, the shock wave has only penetrated a few tens of microns into the foam. The ensuing rarefaction from the driven surface quickly overtakes the shock, turning it into a blast wave, and it is this blast wave that creates the interface dynamics the experiment observes.

At 35 ns after the beginning of the driving laser pulse, a second pulse of three OMEGA beams irradiates a small vanadium foil placed opposite the target from a camera, producing a flash of 5.2-keV He-α X rays, which are used to backlight and produce transmission radiographs of the experiment. These beams also contain 450
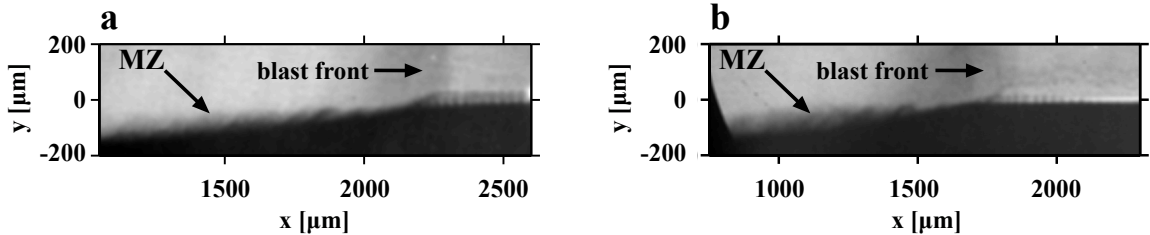
Figure 3.2: Examples of experimental radiographs, showing developing MZ structure in the shocked fluid. The (rightwards-propagating) blast-wave front is visible slightly to the right of the image's center, and the growing MZ in the shocked fluid is visible at the interface to the left of the blast wave. a. This system used 0.05 g/cm^3 CRF; b. This system used 0.1 g/cm^3 CRF.

J each in a flat-topped, 1-ns-long square temporal profile, and are focused to either a 700-μm or 1000-μm diameter spot at FWHM. The vanadium is offset from a tantalum foil into which a pinhole has been drilled, of diameter either 10 or 20 μm. (The optimized diagnostic setup employed a 700-μm laser spot size, with a 10-μm pinhole

and Agfa D7 film. This combination permitted both high contrast and high resolution for this system.) Two examples of experimental radiographs, corresponding to each CRF density, are shown in Fig. 3.2. In these radiographs, lighter color corresponds to higher transmission. The CRF is the material occupying roughly the upper half of the frame, while the plastic occupies the lower half. The rightwards-propagating blast wave is visible, as well as developing MZ structure at the material interface to its left.

3.3.2 Experimental results

The experiment was repeated several times with each density of CRF, and always imaged at 35 ns. This imaging time was chosen such that complicating 3D effects, related to the finite width of the target in the diagnostic direction, have not yet reached the tracer layer at the center of the system [37, 73]. For each resulting radiograph, the width of the MZ was measured at several distances behind the location of the blast wave. This width was defined as the distance from 90% to 10% of the difference in intensity saturation values between the CRF and the plastic, with the intensity averaged over a region of 40 μm, in the horizontal direction, centered on the location being measured. This measurement, for the radiograph shown in Fig. 3.2b, is demonstrated graphically in Fig. 3.3. Due to the contrast between the two materials
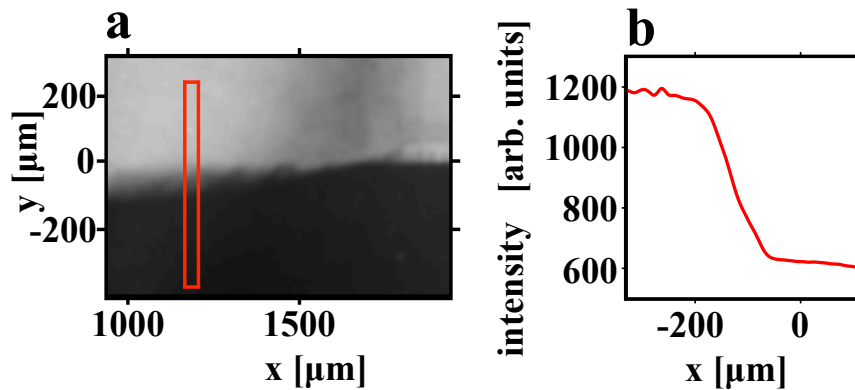
Figure 3.3: a. An example of the sampling region of the MZ; b. Lineout from the sampled region, used to determine the MZ width.

and because the film response to the imaging photons is nearly linear at the signal densities reaching the detector [53], this method produces a consistently-determined measurement that also compensates for complications introduced by large-scale gradients in the intensity of the X-ray source, which can make it difficult to precisely pinpoint the boundaries of the MZ.

The results of these measurements, for all obtained data, are shown in Fig. 3.4. In
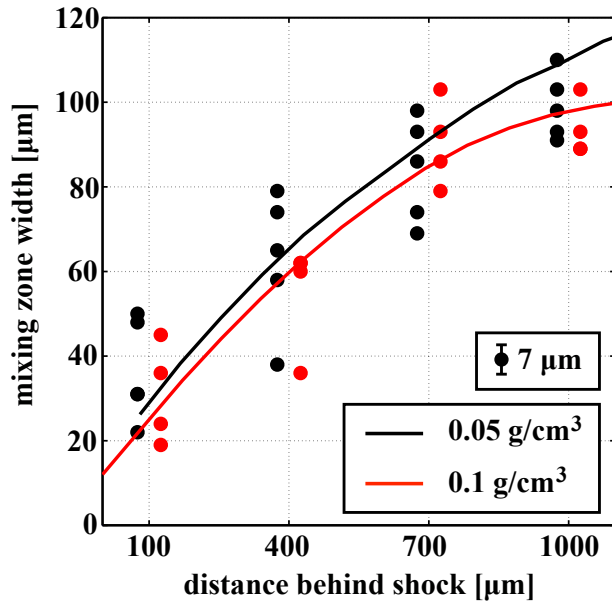
Figure 3.4: Experimental mixing-zone widths, plotted as points, overlaid on solid curves showing the prediction of Eq. 3.2. This prediction is discussed in Section 3.6. The 7 μm error corresponds to the approximate resolution limit of the diagnostic, due to the finite aperture of the backlighter pinhole. The black line and points correspond to systems with 0.05 g/cm^3 CRF, while the red line and points correspond to systems with 0.1 g/cm^3 CRF.

this figure, the measurements are plotted as points, while the solid curves correspond to theoretical predictions to be discussed in Section 3.6. The resolution of the data images, and hence the accuracy of our MZ measurements, is limited by the finite aperture of the pinhole used to collimate the imaging X rays, and in most cases is less than 10 μm. This is much more exact than the reproducibility of the experimental results. Therefore, we represent the error in these measurements by a generalized

error bar in Fig. 3.4 estimating the aperture-limited resolution of the diagnostic, while noting that it is small compared to the variation inherent in repetition of the experiment.

3.4 Interface growth conditions

A depth scan, performed at the interface surface of one of the plastic parts prior to the experiment [26], is shown in Fig. 3.5. Regular tooling striae, corresponding to
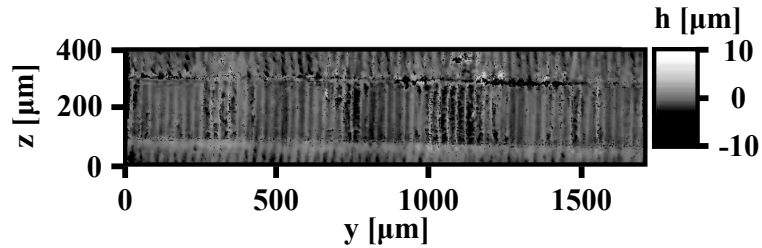
Figure 3.5: Surface depth scan of the initial interface. The wide horizontal band is the surface of the tracer strip, and the vertical features are the tooling striae.

the 16-μm distance between passes of the mill used to machine the final surface, are clearly visible across the part. Spectrally, however, this mode is not significant. (The eye likely only picks it out because it is organized coherently in the vertical direction.) The mode composition is shown in Fig. 3.6. These features occurred consistently on all the plastic parts used in the experiments.

It is well-known that in this kind of experiment the act of driving the system can itself affect the initial conditions [22, 49], and in this experiment the surface perturbation just described acts as a seed for more pronounced coherent structure that the blast wave will experience as the initial conditions. In all experimental frames, such structure is found to arise ahead of the blast wave, as shown in Fig. 3.7, on a length of interface of roughly 100-300 μm. In some images, a dark front is visible near the tips of the features, suggesting that heating of the interface ahead of the blast wave ("preheat") is driving a secondary "wall" shock off the surface of the
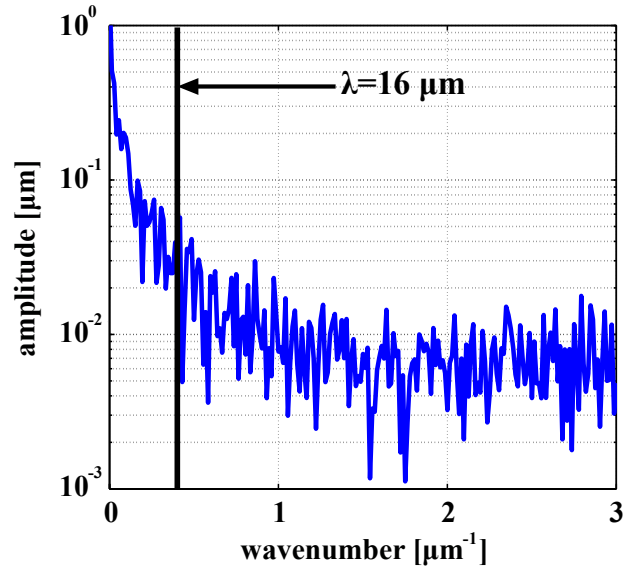
Figure 3.6: The Fourier transform of the initial interface surface's depth scan. The tooling wavelength λ=16 μm is indicated by the vertical lines.
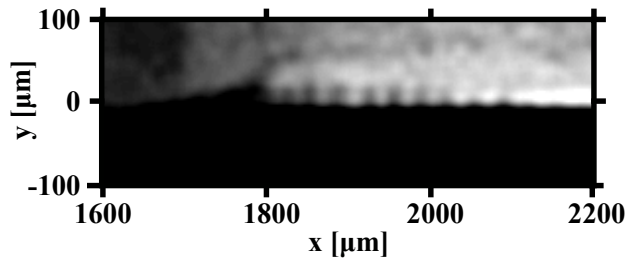
Figure 3.7: The experimental radiograph from Fig. 3.2b, contrast optimized to highlight the periodic structure at the unshocked interface.

plastic into the foam, and that the features could therefore be some combination of consequent Richtmyer-Meshkov [76, 62] and Rayleigh-Taylor [74, 94] growth, seeded by the machining striae. The mechanism producing this shock is difficult to pinpoint, as preheat arising from the laser's interaction with the ablator tends to produce a long wall shock extending well ahead of the primary blast wave, while a wall shock localized to the area immediately ahead of the blast wave is characteristic of the radiative regime, which does not correspond to the present experiment. We speculate that plasma penetration along the foam-plastic interface might be responsible.

Fig. 3.8 shows an example of the Fourier transform of the interface position in this region, extracted from the data in Fig. 3.2b. Although the tooling wavelength
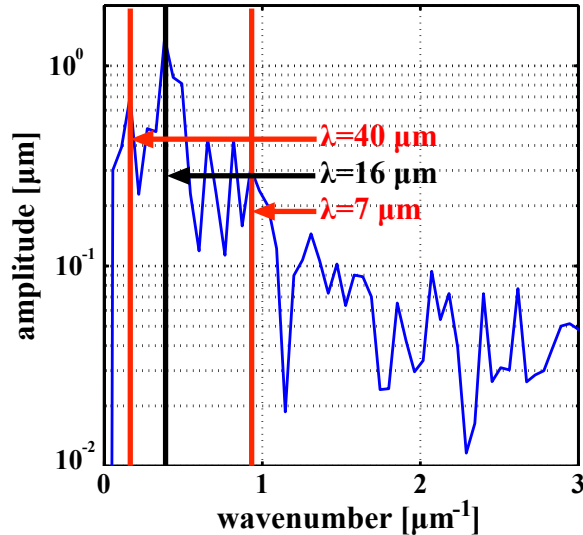
Figure 3.8: The Fourier transform of an interface (corresponding to the data in Fig. 3.2b) just prior to the arrival of the blast wave. The tooling wavelength $\lambda=16$ μm is indicated by the vertical black line, and the upper and lower resolution limits of the Fourier transform are indicated by the vertical red lines.

corresponds to a discernible peak, there is also a broad spectral band with amplitude roughly within a factor of 3 of the peak, from $\lambda=40$ μm down to about $\lambda=7$ μm. These wavelengths coincide respectively with the roughly the upper measurable limit for the length of interface showing structure and the resolution limit of the diagnostic.

The above observations imply that the appropriate theoretical treatment of interface behavior should account for the evolution of an interface having a broadband initial structure. Theoretically, we expect that in such a case vortex merger may play a role in the evolution. The evolution in the presence of vortex merger would be expected to differ from the growth of independent vortices, as follows. Independent vortices would saturate at a peak-to-valley amplitude that is roughly half their wavelength [37, 77, 17]. In the present experiment this would produce no growth beyond that already present ahead of the shock. In contrast, in dynamics dominated by vortex merger the characteristic wavelength $<\lambda>$ grows with time as the vortices merge. This would cause the amplitude of the MZ to grow with time, as indeed is observed. Thus, the observed behavior in the present experiment provides direct evidence that vortex merger is present and important. We model this behavior in the next section.

An interesting counterpoint to these initial conditions is presented by those in the Harding experiment [32, 37]. That experiment was performed using an intentional initial perturbation consisting of a single sinusoidal mode of much larger wavelength and amplitude than the surface features used in the present experiment, and the tooling was also more precise, producing a smoother surface. The resulting system, consequently, exhibits KH behavior much more closely resembling that of a classical, single-mode vortex sheet [17, 77, 37]. Indeed, Harding's experimentally-measured growth can be fully accounted for by such a single-vortex model [32].

3.5 Growth model

We have previously indicated that the growth of the MZ can be thought of as arising from the introduction of vorticity at the interface and its consequent effect on pre-existing structure over time. In a simple, conceptual form arising from dimensionality arguments, the height h of a broadband mixing zone due to the combination of shear and baroclinic vorticity deposition can, at early times, be expressed mathe-

matically as

$$h = h_0 + \alpha\sqrt{\Gamma_S t + \Gamma_B t}, \qquad (3.1)$$

where Γ_S and Γ_B are the shear and baroclinic circulations deposited at the interface, respectively, t is the elapsed time since blast-wave passage, h_0 corresponds to the initial MZ height, and α is a scaling coefficient. Note that, at a given time, t will be different at every spatial location along the interface.

Examining the two circulation terms individually, the shear circulation depends upon the interface shear velocity Δu and the characteristic (average) interface wavelength $<\lambda>$, as $\Gamma_S = \Delta u <\lambda>$. Further, if the behavior is dominated by vortex merger, then $<\lambda>$ will increase in time. (In the limit that the behavior becomes self-similar, $<\lambda>$ will grow in time approximately as $<\lambda> \propto t$, with a constant height-to-characteristic-wavelength ratio $h/<\lambda>$ [77].) The baroclinic circulation has a more complex dependence upon the pressure change across the blast wave ΔP, the density change across the interface $\Delta\rho$, as well as the spectral properties, including the initial interface perturbation wavelength $<\lambda_0>$ and initial amplitude a. Finally, it is worth stressing that this particular analysis requires the assumption of a broad initial interface spectrum, such that the dynamics will be strongly influenced by vortex merging relatively early in time, and hence will not apply to a system with a dominant initial interface wavelength, such as the one presented by Harding [32].

Fig. 3.9a shows an estimate of the baroclinic circulation deposition (extracted from the numerical simulations described in Section 3.6) for these experiments, given the interface conditions encountered by the blast wave, as described in Section 3.4. Over the section of shocked interface visible in the data, the baroclinic circulation is $\Gamma_B \sim 60\text{-}100$ $\mu\text{m}^2/\text{ns}$. Fig. 3.9b shows the shear velocities at these same locations in time, roughly 15-25 $\mu\text{m/ns}$, from which we estimate a shear circulation of $\Gamma_S \sim 250\text{-}400$ $\mu\text{m}^2/\text{ns}$, roughly a factor of 5 greater. For this reason, we expect that the KH behavior in a system with our initial conditions will exhibit shear-dominated growth,
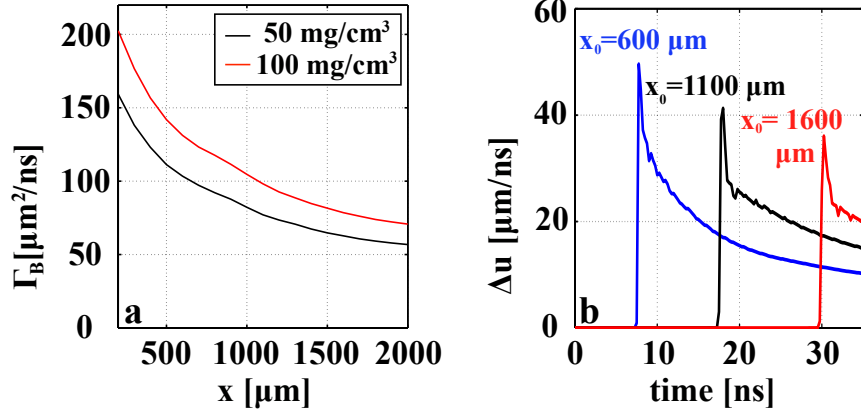
Figure 3.9: a. Baroclinic circulation, as derived from the Euler fluid equations, using the simulated blast-wave parameters; b. Examples of simulated interface shear velocities at given initial fluid parcels, in time. This can be used to estimate the circulation being deposited by the post-shock shear flow.

with a relatively minor contribution from the blast wave itself. In contrast, a similar analysis of Harding's interface yields a baroclinic circulation roughly 50 times greater than ours, while the shear growth rate for such a single-mode-dominated system is 20 times smaller than that corresponding to the initial characteristic wavelength in our system. This is consistent with his result that a single-vortex baroclinic growth model can fully account for the growth observed in that experiment.

In the present experiment, however, depending on how one interprets the spectra shown in Figs. 3.6 and 3.8, it is also possible that there is a contribution to the growth from longer-wavelength modes that do exist and that would not require vortex merger to produce the observed MZ amplitudes. The three frames in Fig. 3.10 show results of a two-dimensional synthetic hydrodynamic simulation of the experiment involving 0.1 g/cm^3 CRF, in which the actual measurement leading to the spectrum in Fig. 3.6 was seeded at an interface corresponding to the shocked materials in the experiment, and a shear velocity of 25 μm/ns was imposed on the interface. Fig. 3.10a corresponds to the state of the experiment roughly 80 μm behind the shock, Fig. 3.10b to the state 160 μm behind the shock, and Fig. 3.10c to the state 240 μm behind the shock. The point of this simulation is not to attempt to make a measurement of the interface;

61
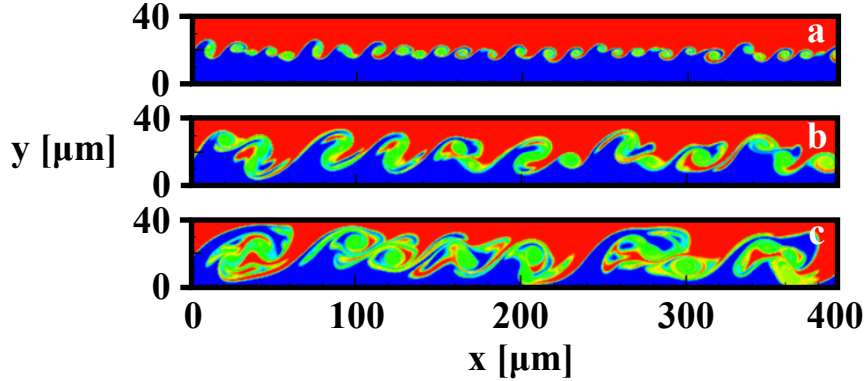
Figure 3.10: A synthetic hydrodynamic simulation, seeded with the interface structure measured from the part shown in Fig. 3.5. The three frames correspond to the evolution of the experimental system with 0.1 g/cm^3 CRF approximately 80, 160, and 240 μm behind the shock.

rather, the clear observation of vortex merger confirms that it is reasonable to suppose that this mechanism is also at work in the experiment, and that the appearance of very-long-wavelength modes is too slow to have much of an effect on the time scale of the experiment.

If such very-long wavelengths were to be initially present, however, the Γ_S term in Eq. 3.1 again would become relevant, and these modes would need to be treated according to Hurricane and Harding [32, 37]. They are difficult to exclude absolutely, because the length of growing structure ahead of the shock, as shown in Fig. 3.7, is too short to detect them using Fourier techniques. In order to do so rigorously, it would be useful to perform further such simulations in which various portions of the spectrum are isolated, thereby demonstrating the relative importance of those wavelengths to the observed behavior.

3.6 Theoretically-predicted KH growth

The nonlinear evolution of classical hydrodynamic shear-driven, broadband growth, in the regime dominated by vortex merger, has been well-documented for many decades, both experimentally [11] and theoretically [77]. Mathematically, it can be

62

expressed as

$$h = C \int_0^\tau \Delta u_{\mathrm{s}} \mathrm{d}t + h_0, \tag{3.2}$$

where the difference between this form and the shear term in Eq. 3.1 involves accounting for the increase with time of $<\lambda>$, which is proportional to Δu_s and also to the time-dependent rate of vortex merging. The proportionality coefficient C will be discussed in more detail below. The principal complication in applying such a model to a decaying, blast-wave-driven system is the fact that Δu_{s} itself has a strong temporal and, moreover, spatial dependence arising from the blast wave's continuous loss of energy as it propagates. Thus, use of simulation to estimate the values of the fluid's physical properties helps accurately track the system's evolution.

To estimate the time-dependent value of Δu_{s}, as well as the values of other relevant fluid properties, two-dimensional simulations, calibrated to produce a correct blast-wave velocity profile, were performed. This was done using a hydrodynamics code [35] built by the Computational Flow Physics Laboratory at the University of Michigan. This code solves the multi-fluid Euler equations using the high-order-accurate Discontinuous Galerkin method, using piecewise linear basis functions. The typical resolution of these simulations was 10 μm. The experimental system is modeled over the size of the CRF and plastic parts, a 2 mm x 4 mm area, and the materials are modeled as ideal gases, maintaining their respective densities. Although the simulation does not allow for the lateral expansion of the system outwards into vacuum, the experimental imaging time is chosen to occur prior to three-dimensional rarefaction effects reaching the tracer [37]. For the purpose of modeling interface dynamics, therefore, this is not a concern. A density map of the simulation, shown at the imaging time for the 0.1 g/cm^3 case, is shown in Fig. 3.11.

The blast wave is created by initially depositing energy into a thin region corresponding to the ablator in the actual experiment, with a reflective boundary condition

63
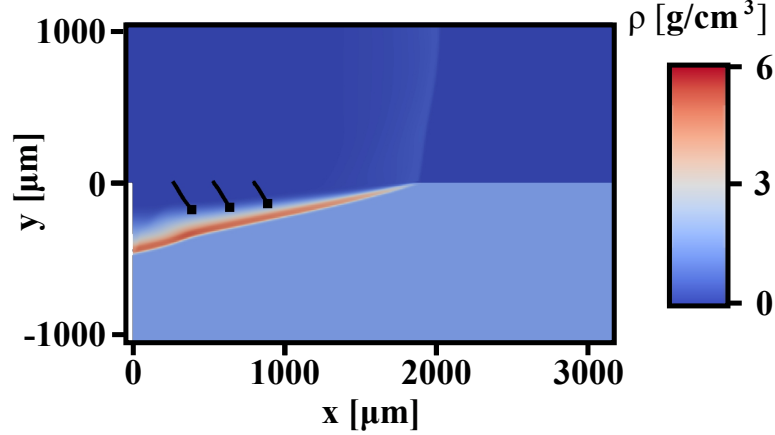
Figure 3.11: A density map of the experiment-calibrated simulation, for the 0.1 g/cm³ CRF case. The black squares are examples of the Langragian test particles used to track motion of the shocked fluid. These test particles were embedded at various locations along the initial material interface, and the markers' trails show their paths of motion under the subsequent evolution of the system. The thin extra band on the left of the upper half of the domain corresponds to the area in which the explosion energy was dumped into the system at the beginning of the simulation.

at this location. Elsewhere, the boundaries permit the free exit of material. This reflective boundary condition is, of course, not physical, and so the simulation is used with the caveat that, near the ablation front, the simulation's predictions may not be reasonable. Comparison of the simulated one-dimensional flow to that predicted using the radiation hydrodynamics code Hyades [54], which includes a laser package and does allow the laser-ablation front to be modeled, indicates that the boundary condition begins to have a significant effect on the flow within roughly $x < 1$ mm from the ablation front at the imaging time of 35 ns. This is consistent with flow expected from original experimental design simulations [37]. Finally, the simulation is calibrated by adjusting the initial energy deposition and the adiabatic index to produce shock behavior (both of the primary blast wave and of the lateral shock driven into the plastic by the pressure of the shocked CRF) consistent with experimental observations.

Lagrangian test particles (shown in Fig. 3.11), embedded in the simulation at

various locations along the interface, allow accounting of the motion of the shocked fluid, and hence the tracking of the relevant parameters at individual fluid parcels for the duration of the experiment. The resulting simulated values for the shear velocity Δu_s, examples of which are shown in Fig. 3.9b, can then be numerically inserted into Eq. 3.2, along with an initial MZ height $h_0 = 12\,\mu\mathrm{m}$ estimated from measurements of the widths of the initial MZ in the experimental radiographs, immediately in front of the blast wave. Finally, an empirical value of 0.18 for the proportionality constant C was used, taken from measurements done in pure hydrodynamics experiments [11], and also consistent with theoretical predictions for a self-similar evolution [77]. The results of this calculation are shown in Fig. 3.4, alongside the measured MZ heights from the experimental data. The generalized error bar included in the figure comes from width measurements of nominally-sharp features, such as the unshocked interface, and corresponds to the pinhole-aperture-limited resolution of the diagnostic. It can be seen in this figure that, at all locations, the model's predictions fall within the spread of the experimental data. As discussed in the previous section, the experimental observations directly imply that vortex merger dominates the evolution of structure at the interface. The results shown here would be consistent with fully self-similar behavior, but the coefficient C is not so closely constrained that one can draw a definite conclusion regarding how close the system actually is to such behavior.

3.7   Conclusions and future directions

Initial conditions clearly play an important role in KH dynamics at a material interface, determining the physical processes at work and the consequent interface growth occurring in the system. In this chapter, we drew a theoretical distinction between two sources of circulation arising from vorticity deposition (baroclinic deposition by the blast wave versus sustained-shear deposition by the ensuing shocked flow). We further emphasized the nonlinear evolution of the interface (proclivity to-

65

wards independent vortex growth versus vortex-merger-dominated dynamics). We then identified conditions for each aspect's contribution to the overall growth observed.

Further, we were able to create an HED system designed to produce experimentally-observable KH structure, and in which we were able to understand clearly the initial conditions seeding the growth of this structure. Predictions of the growth using classical models of the appropriate physical processes, and adapted to the particular dynamics of this HED experiment, are consistent with the growth observed, and this result, combined with that of previous experiments [32] suggests that shear-instability dynamics in HED systems are dominated by pure hydrodynamic behavior. In our particular case, the evidence clearly indicates that the dominant behavior is vortex merging, and that the system may be approaching a self-similar state. This has relevant implications for HED systems that exhibit similar shear flows as some aspect of their dynamics.

This work can be extended in several directions, the most immediate involving performing similar experiments in which the spectral characteristics of the initial interface surface are more-finely controlled. Such initial conditions would allow us to further test our ability to predict KH behavior using the theoretical reasoning presented here. Also, advances in laser technology have permitted the design of an experimental platform to study hydrodynamics under steady shock conditions [56, 19, 58], which has the potential to free the instability analysis from complications related to decaying shock conditions. Finally, simulation or even vortex-merger modeling [77] of various portions of the initial mode spectrum could provide a rigorous test of the self-similarity of the system.

CHAPTER IV

Late-time breakup and shock behavior in Rayleigh-Taylor experiments

4.1 Introduction

The work described in this chapter is adapted from the manuscript "Late-time breakup of laser-driven hydrodynamics experiments," published in *High Energy Density Physics*, as well as from separate, unpublished work arising from similar experiments as those described in this manuscript. The first part of the chapter concerns the breakup of Rayleigh–Taylor (RT) structure in experiments where the energy of the laser driving the instability is low, and the second uses data from RT experiments for an entirely different purpose, namely to study the driving of shocks in plastic by a laser. My role in these projects was the planning and execution of the experiments, as well as data analysis. In addition, I also performed the theoretical turbulence analysis contained in the manuscript. In the second part, I also include experimental results previously reported by Carolyn Kuranz and Paul Drake [24, 51, 50].

4.2 Turbulence in HED instability experiments

4.2.1 Experimental background

High-energy-density, blast-wave-driven hydrodynamic instabilities are relevant to any physical system characterized by the sudden deposition of relatively large amounts of energy into small volumes. These instabilities are of practical concern, for example, in efforts to harness energy via inertial-confinement fusion, and they also play a fundamental role in many astrophysical processes. The experiment described here is motivated by the latter, particularly the physics of Type IIa supernovae. In these core-collapse supernovae, a spherical blast wave originates at the center of a star and propagates outward, across the star's layers of gases. It has been demonstrated that, by appropriate choice of parameters, a blast-wave experiment can be constructed that exhibits hydrodynamic similarity, including unstable behavior, to the supernova [82, 78]. However, one process that does *not* behave similarly across these systems is the onset of turbulence, which will be explored in more detail here.

Experiments of this nature [24, 51] can be performed using pulsed lasers, such as those at the Omega Laser Facility [9, 60], to drive the physics. First, a planar blast wave is created by depositing pulsed laser energy onto a material surface. The rapid rise in pressure due to the initial irradiation drives a shock wave into the material, while the end of the laser pulse and consequent relaxation of this pressure allows a rarefaction to follow. The pulse length is chosen such that the rarefaction quickly overtakes the shock wave, turning it into a blast wave before it reaches the region of physical interest to the experiment.

Such a blast wave can in turn be used to drive hydrodynamic instabilities. Of particular interest to this experiment is the RT instability [74, 94], which arises in a fluid or collection of fluids as a potential-energy-reducing mechanism when a particular portion of the fluid containing a density gradient experiences a pressure gradient

68

with an antiparallel component. In this situation, any nonuniformity in the gradients' lateral spatial profile will grow in time, and this perturbation develops into spikes of the denser material penetrating into the less-dense material. In the present experiment, this configuration is achieved by layering two carefully-chosen, solid materials of differing density in the path of the blast wave. A density gradient is immediately present at the materials' interface, and a pressure gradient arises due to the materials' differing responses to the passing blast wave. Previous experiments performed using the OMEGA-60 laser have demonstrated significant RT-unstable growth of a controlled interface perturbation in this manner [50].

When such an experiment evolves over long enough times, the possibility exists for secondary processes to develop and influence the system's dynamics. In particular, such processes can introduce lateral motion in the system that undermines the unidirectional flow the experiment seeks to create and study. The blast wave, meanwhile, loses energy as it propagates, and in the experiment this causes the motion of the interface to slow. The effect of the blast-wave-driven physics in the system consequently diminishes, and eventually the RT physics is no longer the dominant process. This limits the time scale on which the experiment is meaningful.

In the present experiment, performed on the OMEGA-EP laser, RT instability is seeded in a system as described above, using a well-characterized perturbation at the interface between two materials and driven by a roughly-planar, laser-produced blast wave. Turbulent-like structure is observed in X-ray images of the system taken at relatively late times instead of the well-ordered RT spikes and bubbles expected from the perturbation pattern, and this chapter investigates the origin of this structure, focusing principally on the possibility that the blast-wave-driven flow can become turbulent as well as the influence of secondary effects in the shocked system.

4.2.2   Experimental design and results

The experimental system is composed of a 100-μm-thick polyimide (PI, $C_{22}H_{10}O_5N_2$) plastic disk of density 1.4 g/cm^3 abutting a carbon resorcinol formaldehyde (CRF) foam cylinder of density 50 mg/cm^3, all enclosed in a 25-μm-thick PI shock tube, shown in Fig. 5.1. At the disk/CRF interface, a seed perturbation comprising two
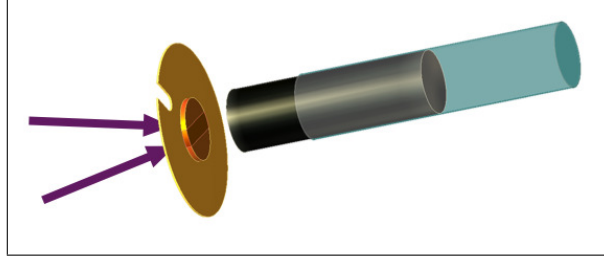
Figure 4.1: Exploded-view rendering of the experiment's physics assembly. From the left: arrows indicate the direction of the laser drive; the round, flat component is the plastic disk; the black cylinder is the CRF; and the light-blue, transparent cylinder is the enclosing shock tube.

orthogonal sinusoids of initial wavelength $\lambda = 71$ μm and amplitude $a_o = 2.5$ μm has been machined into the plastic. Embedded in the plastic is a 250-μm-thick tracer layer of iodine-doped plastic, orthogonal to the diagnostic sightline, encompassing exactly three rows of the sinusoidal features. The tracer material is chosen such that it is of similar density to the surrounding disk, thus not affecting the hydrodynamic evolution of the system, yet is significantly more opaque to the imaging X rays, thus permitting us to view the physics at the center of the target, away from boundary effects. In the axial direction, the tracer layer begins at the interface surface, but only extends partway through the disk, such that it does not reach the outer, laser-irradiated surface. The plastic disk, with the seed-perturbation and tracer features visible, is shown in Fig. 4.2.

Two OMEGA-EP beams, producing laser light at a wavelength of 351 nm with 1-ns-long, flat-topped temporal profiles, simultaneously irradiate the outer surface of this plastic disk, as shown by the arrows in Fig. 5.1. The spatial profile of each pulse
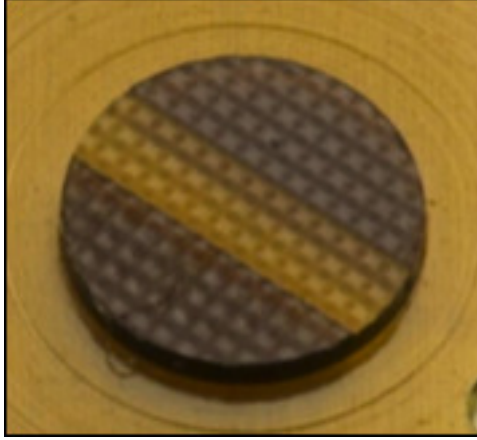
Figure 4.2: Surface of the machined plastic. The seed perturbation is clearly visible, as well as the lighter-colored tracer layer traversing the disk.

is smoothed using a distributed phase plate (DPP) producing a 750 μm spot size (full-width, half-max) on the disk. The two beams' total energy is roughly 2400 J, resulting in an average irradiance of roughly 5.4×10^{14} W/cm^2. The sudden pressure of about 20 Mbar of the resulting laser-ablated plastic plasma drives a shock wave into the disk. In the first nanosecond, while the laser pulse is on, the shock travels approximately 40 μm into the disk. At this point, the laser pulse ends, and a rarefaction propagates into the plastic. It overtakes the shock, creating a blast wave, around 70 μm into the disk, prior to reaching the material interface. For comparison, previous experiments on the OMEGA-60 laser produced a 40 Mbar impulse. The ablation pressures quoted here are those that reproduce the observed shock locations in calibrated simulations of the respective experiments done in the 1D Hyades code [54].

As the blast wave passes the interface, it imparts to the interface some velocity, and the interface's subsequent deceleration against the CRF causes growth of the initial seed perturbation's amplitude. Immediately following blast-wave breakout from the plastic, the Richtmyer-Meshkov process is primarily responsible for perturbation growth, but the RT growth rate quickly increases, and within 2 ns becomes the dominant mechanism for the duration of the experiment. After a 38-ns delay from the initial laser pulse, a single ultraviolet beam irradiates a 5-μm-thick vanadium foil,

offset 4 mm from the experimental system, producing the 5.2-keV He-α X rays used to image the system. This beam has the same temporal profile as the blast-wave drivers, but not the same spatial profile. It has an energy of around 1 kJ and is smoothed by a DPP, producing an 1100 μm spot size (again full-width, half-max) on the foil, resulting in an average irradiance of 1×10^{14} W/cm^2. Opposite the experimental system from this diffuse X-ray source, a pinhole is placed in front of X-ray film, positioned such that the resulting image on the film has a magnification of 6.

Figure 4.3a shows a radiograph of an OMEGA-60 experiment, which featured a shock driven by a 40-Mbar ablation pressure into a PI layer 150 μm thick. The experiment was imaged at 21 ns, measured from the beginning of the initial physics-driving laser pulse to the beginning of the imaging laser pulse. In this image, the
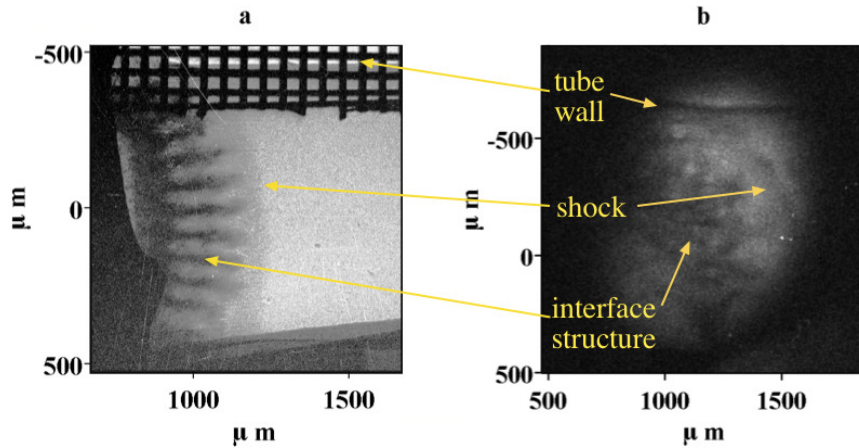
Figure 4.3: a. Radiograph of a previous, similar experiment, taken at earlier time and with a greater driving energy; b. Radiograph of the present experiment. In both frames, the shock tube is horizontal, and the blast wave propagates from left to right.

shock tube occupies nearly the entire frame, and the edges are partially obscured by a spatial fiducial (a gold grid of known wire spacing) at the top and a transmission fiducial (aluminum foils of known thickness) at the bottom. The right half of the image is mostly occupied by unshocked foam, and the rightward-propagating blast wave is visible in roughly the center of the image. To the left of the shocked foam behind the

blast wave, the dark region is shocked, iodine-doped plastic. The interface between these two materials shows the RT-unstable structure the experiment is designed to produce. The leftmost, darkest area of the image shows part of a 25-μm-thick gold foil used to shield the camera from the ablated-plasma plume created when the initial laser pulse drives the experiment, and finally the thin light region between the foil and the iodinated plastic corresponds to undoped plastic, beneath the tracer layer. Under these conditions, one observes well-ordered RT structure at the material interface.

Figure 4.3b shows a radiograph of the current experiment, featuring a shock driven by a 20-Mbar ablation pressure into a PI layer 100 μm thick. The experiment was imaged at 38 ns. The shock, propagating left to right, is visible in the upper-right corner of the image, as is the mixing layer to its left. The shock-tube wall runs horizontally along the top of the image, and the corner of the fiducial grid is present at the bottom, at around 1000 μm along the abscissa. A secondary shock, moving radially inward from the tube wall due to preheating of the shock-tube wall by the driving laser event, is also present in the upper right, along with the associated kink in the forward shock [49, 22].

The radiograph in Figure 4.3b, in contrast to Figure 4.3a, presents an interesting anomaly in the behavior of the mixing layer. Instead of the expected well-ordered series of spikes and bubbles resulting from RT-unstable growth of the initial seed perturbation, the mixing layer consists of incoherent structure. The appearance of the image is complicated by the three-dimensional profile of the RT structure, whose cross-section follows the initial seed pattern in Figure 4.2. The bulk of the the signal attenuation in the plastic occurs in the tracer region in the center of the disk; what the radiograph should show, then, is the integrated attenuation of three rows of RT spikes. If the spikes begin to exhibit independent lateral motion, however, they fall out of alignment with each other. Instead of a well-defined attenuation profile, the result will be several regions of distinct attenuation, depending on how many spikes

73

fall in the path of the imaging X rays at a given location. Thus, the mixing layer will appear significantly disordered.

Despite the fact that individual spikes are difficult to discern in this image, the regions of greater and lesser attenuation are of the expected size scale. As shown
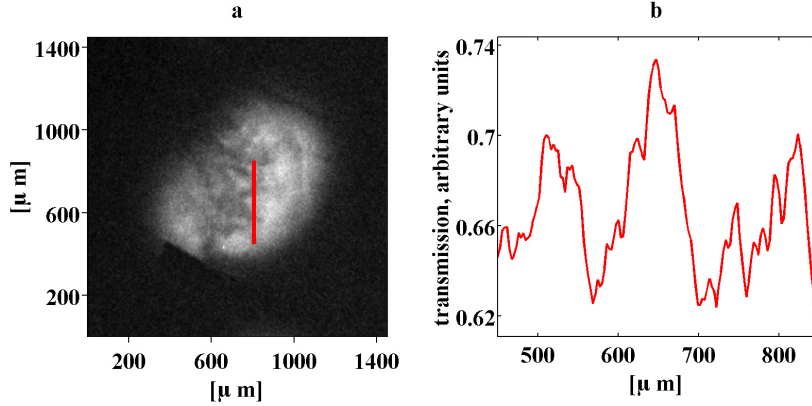
Figure 4.4: Transmission sample in the mixing region.

in Fig. 4.4, regions of signal attenuation are spaced roughly 90-100 μm apart; this is larger than the initial perturbation wavelength of 71 μm, but the discrepancy is consistent with the effects of dynamics commonly observed in this kind of experiment. Two underlying causes could lead to distortion of the interface structure. First, the entire system's outward expansion in the wake of the forward shock increases the separation between RT features. Second, asymmetries in the nominally-planar shock cause growth with a lateral component. In this particular experiment, the forward shock front is significantly curved, and is even more distorted by its lower speed in the wall-shocked region, causing the RT features to diverge and increasing their apparent wavelength. This leads us to believe that what is seen in the mixing layer is in fact spikes of RT structure that have lost their purely-axial, RT-driven motion, and have begun to evolve under the influence of other processes.

4.2.3 Discussion

We now turn to consideration of processes that can give rise to this kind of in-coherent structure, beginning with the capacity of the flow's physical properties to allow for the development of turbulence. The structure in the Fig. 4.3b radiograph displays qualitative similarity to simulation work [66, 64] done on the transition of similar experiments from a highly-ordered flow dominated by axial RT instability to a fully-turbulent flow in which the lateral periodicity of the initial interface structure is no longer apparent. In the context of this work, our radiograph appears to be an image of the system in an intermediate phase, where the bubbles have begun to coalesce due to some smaller-scale dynamics. The purpose of such analysis is not to make a determination of the flow itself becoming turbulent, but to establish that the flow admits structure on a scale that can seed larger-scale lateral motion leading to bubble coalescence such as that in Fig. 4.3b.

To estimate a time for the appearance of a turbulent length scale in this ex-periment, we establish the evolution of the bounding length scales from simulated physical properties of the system [79, 107]. The bounding length scales depend upon the Reynolds numbers of the two materials near their interface, which in turn de-pend on their viscosities. A simple estimate of the viscosity ν can be found using Braginskii's formula [10],

$$\nu[\text{cm}^2/\text{s}] = 3.3 \times 10^{-5} \frac{A^{1/2} T[\text{eV}]^{5/2}}{\log{(\Lambda)} Z^4 \rho[\text{g}/\text{cm}^3]},\tag{4.1}$$

where A is the corresponding mass number, T the ion temperature, $\log{(\Lambda)}$ the Coulomb logarithm, Z the ionization, and ρ the density. Although these plasma properties cannot be directly measured during this experiment, they can be simu-lated, which is sufficient for the purpose of understanding the length scales on which the phenomena of interest can arise. The values used here are taken from the values

given immediately on either side of the interface by the 1D Hyades simulation of this experiment mentioned previously.

Since the Coulomb logarithm $\log(\Lambda)$ tends to not be sensitive to variations in temperature, ionization, and ion/electron density, and our goal here is an estimate of length scales, it is convenient and appropriate to make the simple approximation $\log(\Lambda) \sim 2$, based on an order-of-magnitude estimate of these parameters [36]. The resulting viscosities of the two materials are shown in Fig. 4.5a.
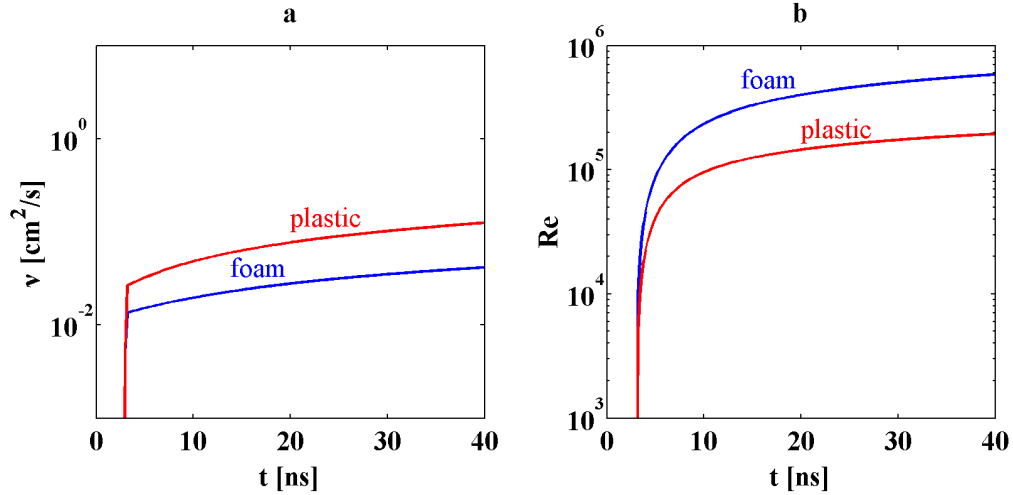
Figure 4.5: a. Calculated value of the plasma viscosity at the interface; b. Corresponding Reynolds number.

Since we are interested primarily in the behavior of the mixing zone, we can construct relevant Reynolds numbers for both materials using as kinetic scales the length L and growth velocity v of the RT-unstable features in the mixing region. Assuming that the growth is predominantly self-similar (linear growth velocity), and approximating L by the size of the mixing region evidenced in the data in Fig. 4.3, the corresponding Reynolds numbers are shown in Fig. 4.5b.

These Reynolds numbers can be used to estimate a lower bound on the turbulent length scales that can appear (from the Kolmogorov microscale λ_k) and an upper bound (from the Taylor microscale λ_T). The physical significance of these scales is that below λ_k the system's viscosity tends to smooth out any turbulent behavior,

while above λ_T the viscosity promotes the development of a laminar boundary layer, and thus the initial, well-ordered configuration of the mixing layer persists. Again using L as the relevant length scale,

$$\lambda_k \sim L \cdot (\mathrm{Re})^{-3/4} \text{ and} \tag{4.2}$$

$$\lambda_T \sim L \cdot (\mathrm{Re})^{-1/2}. \tag{4.3}$$

Dimotakis [21] showed that turbulence can arise when there exists a sufficiently-large region between these two bounds that the scales are decoupled from the corresponding limiting effects of the viscosity. This region λ is given as

$$50\lambda_k < \lambda < 5\lambda_T. \tag{4.4}$$

These bounds are shown in Figure 4.6, and indicate that on the order of 10 ns following the drive of the initial shock, turbulent behavior can begin to occur on a roughly 1-2 μm size scale at the material interface.

The largest-scale structures in this experiment are the RT spikes and bubbles themselves, and as they exist for longer times and continue to have a greater amplitude-to-wavelength aspect ratio, the possibility of secondary dynamics affecting their lateral stability grows. Such dynamics do not need to occur on the scale of the structure seen; the spikes and bubbles provide the scale size, and only need some mechanism by which they can begin to laterally coalesce as they are allowed to evolve for longer times prior to imaging. Fig. 4.6 indicates the capacity of the flow to accommodate small-scale structure, and it has been shown that turbulence of this size scale can cause significantly larger-scale mixing to occur at the material boundary [39]. We now describe some processes that could produce the kind of structure seen in Fig. 4.3b.

One example of such a process is Kelvin-Helmholtz (KH) instability at the mixing
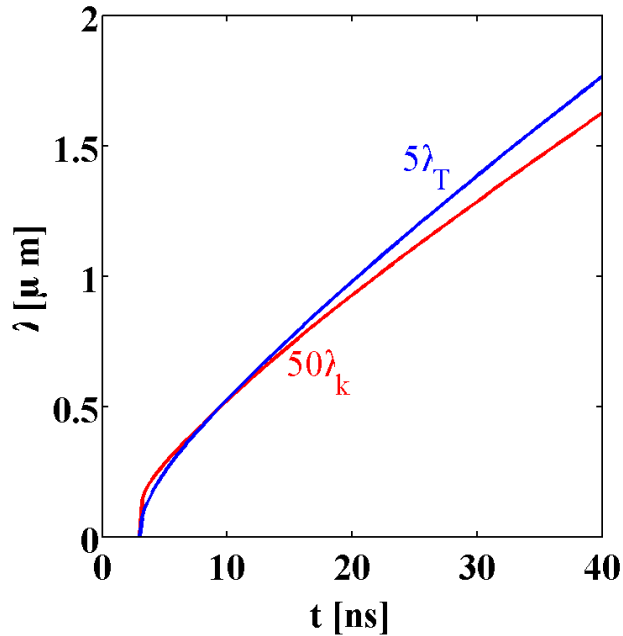
Figure 4.6: Inner and outer scales for turbulent development at the interface. The red curve corresponds to a multiple of the inner, Kolmogorov microscale, while the blue corresponds to a multiple of the outer, Taylor microscale.

zone. As the plastic and CRF interpenetrate, their interface experiences a shear force. Given that the mixing zone at the interface of the experiment in Fig. 4.3b has grown to roughly 300 μm, a simple estimate of the scale size $\lambda_{\mathrm{KH}} \sim .1 \cdot \Delta(u)t$ that could develop is about 30 μm, or roughly the lateral width of the original RT features.

Another possible source of lateral motion is from the vortex ring that develops within the RT bubbles as they evolve. The same shear that could seed KH instability at the bubble boundary also imposes a drag force on the outer edge of the bubble that the interior does not experience. Over time, this motion develops into large-scale vortical motion, of differing vorticity at the bubble tip, center, and base due to variation in the shear at these locations. This could also serve to destabilize the bubbles laterally and provoke their coalescence.

Finally, we turn to the question of why this behavior is seen in the late-time radiograph in Fig. 4.3b, but not in previous experiments imaged at earlier times. From

Fig. 4.6, we estimated that the properties of the flow in this experiment begin to allow for a turbulent subrange on the order of 10 ns following the initial shock. However, more time is required for this structure to develop, and even more time would be required for it to cause the primary RT bubbles to coalesce. Fig. 4.7 shows the interface acceleration history for both the previous OMEGA-60 experiments and the present OMEGA-EP experiment, as well as typical imaging times for both experiments. The
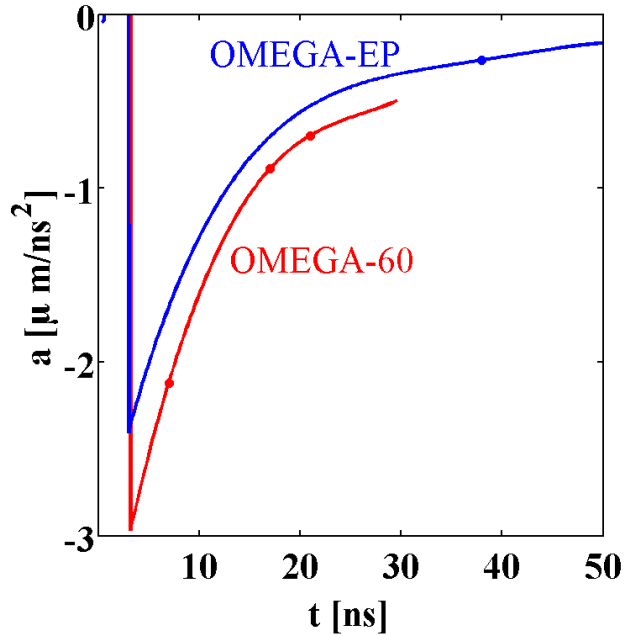
Figure 4.7: Acceleration profiles, from simulation, of the interfaces in the OMEGA-60 and the OMEGA-EP experiments, corresponding to the data in Fig. 4.3.

profiles in Fig.4.7 were obtained from the same 1D Hyades simulations used previously to estimate the ablation pressures and turbulent scales λ_k and λ_T. Analysis of the OMEGA-60 case indicates a time of 15-20 ns for the appearance of the turbulent scale [79], which is very close to the imaging times of these experiments, and suggests that secondary dynamics have not had sufficient time to develop. The present experiment has evolved for a much longer time prior to imaging, and has been driven by a weaker blast wave, which could provide the time for these dynamics to noticeably affect the interface structure. It is also possible that, since the radiograph actually

79

shows an integrated line of sight through three rows of RT features, some coalescence has begun to occur but is simply not yet obvious. Since secondary structure would likely occur in random locations, if for example one spike has begun to break up at a particular location but the other two in line with it have not, this would be difficult to observe directly in the radiograph.

4.2.4 Conclusions

The onset of secondary processes, combined with dissipation of the blast-wave energy and the resulting slowing of the interface, has important ramifications for the relative importance of different hydrodynamic processes in instability experiments of the kind described here. In turn, this limits the useful duration of such experiments. In the preceding analysis, we have explored some of the specific mechanisms by which this can occur. It is clear that the scale of the turbulent-like behavior seen in the radiograph in Fig. 4.3 is too large to be a direct consequence of turbulent flow, and in fact any turbulence that could be developing would be of smaller scale than the resolution limit of the imaging diagnostic. However, because the system is being imaged at a late time, this structure has time to seed larger-scale motion that could result in the RT features coalescing. As a result, the axial RT physics that is the physics of interest to this experiment is no longer the dominant process in the system, whose behavior is instead being driven by developing secondary dynamics.

4.3 Laser-driven shocks in the plastic medium

4.3.1 Experimental background

Laser-driven shock waves play an important role in experimental high-energy-density physics, including the study of various astrophysical phenomena [82, 78], inertial-confinement fusion [1], and pure hydrodynamic instability [24, 32, 56]. Often,

an experiment of this nature is initiated by the direct irradiation of some solid material with a pulsed laser. This deposition of energy onto the material surface causes it to ablate, and the pressure of the resultant plasma on the remaining material drives the desired shock wave into the material. The details of the interaction of the laser with the material, then, are of consequence to the properties of the produced shock wave, and by extension, to the physics one hopes to observe.

Simulations can be a useful tool in planning such experiments, but since the physics depends upon the particular shock wave driven, it is not sufficient that the simulation code only properly model the hydrodynamics of shock-wave propagation. It must also be able to predict the behavior of the driven shock wave given the particular lasers available, and this task turns out to be considerably difficult, given the complex and diverse physical processes relevant to the laser's interaction with the material it irradiates. To date, attempts to model this interaction have only been partially successful, making experimental evidence important both to understanding the reliability of current models and to future improvements to such models.

In designing these experiments, it is typically desirable to choose a low-atomic-number material for the ablator, in order to limit the emission of high-energy photons during irradiation. Such materials are mostly gaseous under normal conditions or otherwise not suitable for machining, greatly limiting the options available. Beryllium is one possibility, and due to its impermeability, is particularly valuable when a higher-Z gas is involved in the experiment. Experiments specifically designed to measure laser-driven shock propagation in beryllium ablators have been performed [52]. However, beryllium's brittleness and toxicity introduce considerable difficulty into the machining process, and thus is not always a practical choice. Plastic, on the other hand, is convenient and unproblematic because it can be easily shaped, machined, and doped according to experimental needs. It is thus extensively used, but plastic test work has mostly been directed towards its equation of state (EOS) [5, 4], rather

than laser interaction with the material.

This kind of experiment is very resource intensive, and thus it can be difficult to secure facility and financial support for dedicated experiments of such narrow scope as ablator-behavior characterization. Previous work on this topic has been focused on the context of spherical fusion implosion capsules [92, 15, 31]. It is, hence, particularly desirable to find a way to use the results of existing experimental data for this additional purpose. Here, we will describe an experiment, performed on the OMEGA-60 laser [9] and using a planar plastic ablator, whose primary goal is the study of blast-wave-driven RT hydrodynamic instability under high-energy-density conditions [82, 78, 24, 51], and describe a method for exploiting data involving several variations of the experiment's initial conditions to extrapolate information about early-time behavior of the shock. We will then compare these results to predictions made using the CRASH simulation code in an effort to better understand the effectiveness of CRASH's laser-energy deposition model. The predictive capabilities of simulations for this system, in the context of an interest in the effect of variation in the properties of the hydrodynamic flow on RT instability growth, have already been studied [65]. In the present work, we focus on the dynamics of the shock itself, and on the performance of simulation with variation in the interface Atwood number.

4.3.2 The experiment

The experimental system we will use to analyze shock behavior in this work consists of a 150-μm-thick polyimide (PI, $C_{22}H_{10}O_5N_2$) disk of density ρ_P=1.4 g/cm^3 pressed against a carbonized resorcinol formaldehyde (CRF) foam cylinder of lesser density, either ρ_C=0.1 g/cm^3 or ρ_C=0.05 g/cm^3. These two components are then encased in a PI shock tube with 0.025-mm-thick walls. In some cases, the PI disk has had sinusoidal patterns machined into the face abutting the CRF. These patterns typically have amplitudes a=2.5 μm and wavelengths of several tens of microns. In

some experiments the sinusoid oscillates only along one direction (a so-called two-dimensional perturbation), while in others orthogonal sinusoids were machined into the plastic (a so-called three-dimensional perturbation). Although these patterns significantly affect the interface dynamics after passage of the blast wave, the lateral profile of the shock quickly stabilizes itself following breakout from the plastic, and its propagation is unaffected. This was confirmed using otherwise-identical 2D CRASH simulations of the patterned- and flat-interface experiments.

The plastic disk is irradiated by ten simultaneous, 450-J OMEGA beams, each having a 1-ns, flat-topped temporal profile and a spatial profile smoothed by an SG8 distributed phase plate (DPP), producing an 820-μm-diameter spot on the disk. This results in an irradiance of about $9\mathrm{x}10^{14}\mathrm{W/cm^2}$, and creates an ablation plasma of roughly 40 Mbar. This sudden ablation pressure drives a shock wave into the disk. When the laser pulse ends, the relaxation of the laser pressure allows a rarefaction to propagate into the disk. At this time, the shock has traversed only roughly half the disk, allowing enough time for the rarefaction to overtake the shock and turn it into a blast wave before breakout from the disk.

Following a delay (our definition of duration is the elapsed time between the start of each pulse and the measurement time), a second pulse of 3-5 beams irradiates a metal foil (typically, of atomic number around $Z=23$), oriented orthogonally to and offset approximately 1 mm from the experimental system's axis, which produces the He-α X rays used to image the system. For example, a frequent choice is vanadium, resulting in 5.2-keV X rays. These beams have the same temporal profile and energies as the physics drivers, and are defocused to a diameter of 800 μm at the foil. A tantalum foil containing a pinhole, often 10 μm in diameter, is placed between the system and the foil, and is offset 500 μm from the foil. This effectively creates a point source of X rays backlighting the system, which is then imaged by a detector located opposite the system from the pinhole, with typical magnification of $\sim$20.

An example of such a radiograph, to which simulation results will be presently compared, is shown in Fig. 4.8. In this image, the light-colored area occupying most of
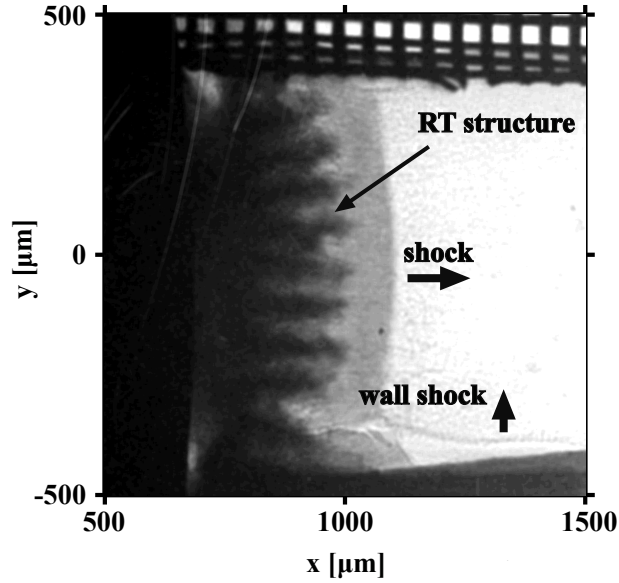
Figure 4.8: An experimental radiograph, for a system involving 0.01 g/cm^3 foam, taken at 21 ns. The rightwards-propagating blast wave is visible just to the right of the image center, and the Rayleigh-Taylor interface structure is to its left. A wall shock is visible propagation upwards from the shock tube wall at bottom.

the right-hand side is unshocked foam. The rightwards-propagating shock is visible as the sudden darkening of the radiograph just right of center, while the material interface, exhibiting RT-unstable structure, is present just left of center. At the shock-tube edges near the top and bottom of the frame, a gold grid serving as a spatial fiducial and aluminum strips serving as a transmission fiducial are respectively visible. Finally, a secondary shock known as a wall shock, likely driven by preheat of the shock tube by radiation or energetic particles arising from the laser/ablator interaction [22, 49, 18] is visible at the bottom of the image.

In order to extract the shock position from the data, a horizontal line sample of the radiograph, averaged over some number of vertical pixels (18, corresponding to about 20 μm in the data in Fig. 4.8 is taken at the shock location. The midpoint of the rise in image intensity is taken as the shock location. The values obtained from

the data in this manner, for both 50 mg/cm^3 and 100 mg/cm^3 foams, are shown in Fig. 4.9 [24, 51, 50]. A power-law function is then fit to these shock locations in time,
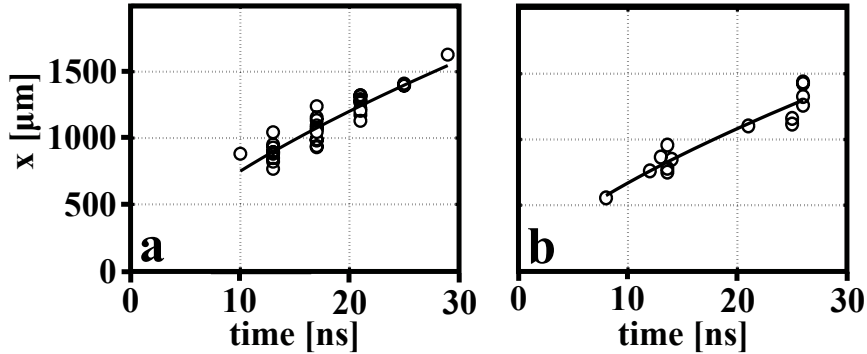
Figure 4.9: a. Shock locations for all available data for systems with 0.05 g/cm^3 CRF; b. Shock locations for all available data for systems with 0.1 g/cm^3 CRF. Best-fit power-law curves are also plotted, as solid lines, for each case.

and this best-fit curve is what will be used to test the performance of the simulation. The two shock propagation curves x_{50} and x_{100}, for the 50 mg/cm^3 and 100 mg/cm^3 foams, respectively, are

$$x_{50}[\mu m] = 157.37 \cdot (t[\text{ns}])^{0.6786}$$

$$x_{100}[\mu m] = 135.40 \cdot (t[\text{ns}])^{0.6940}.$$

4.3.3 The simulation

The CRASH code is an Eulerian, adaptive-mesh-refinement radiation-hydrodynamic model built to simulate experiments in the high-energy-density physics regime [98]. CRASH uses a multigroup diffusion radiation transport model, with the radiation and electron heat conduction solved implicitly, and utilizes fully 3-D ray tracing to model the laser energy deposition [99].

In order to make a comparison to the experimental results discussed earlier, CRASH was used to simulate the irradiation of a 150-μm, 1.4 g/cm^3 PI disk with a 4.5 TW, 1-ns laser pulse, with 100 ps rise and fall times. Behind the disk, the foam is modeled as low-density PI (either 0.05 or 0.1 g/cm^3) bounded radially by 25-μm-thick PI walls. The choice of a model for the CRF is an important problem for the accuracy of this or any simulation, because the non-continuous internal structure of the CRF introduces complications in the EOS that are difficult for the simulation to capture. Within this constraint, low-density, continuous PI was chosen because it is a familiar material of similar chemical composition as CRF. The entire setup is shown in Fig. 4.10. In order to lower computational cost, the simulation models the

1400 μm

25 μm

920 μm

1024 μm

150 μm

■ **vacuum (simulated as 0.01 mg/cm PI)**

■ **PI (1.43 g/cm)**

■ **PI (0.05 or 0.1 g/cm)**
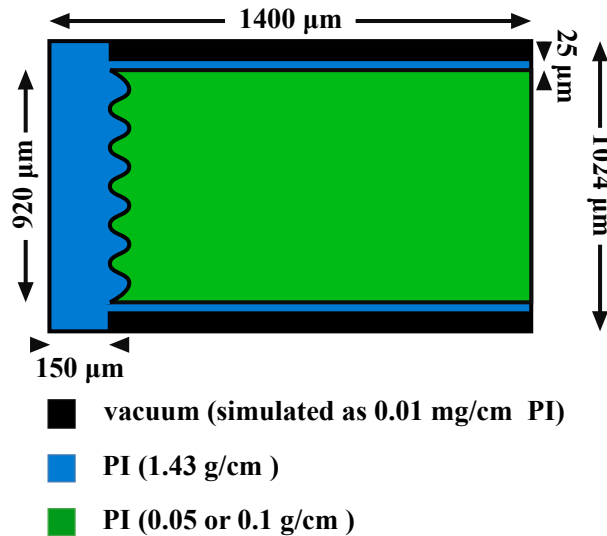
Figure 4.10: A schematic drawing of the simulation setup. The chemical composition of the CRF and plastic are similar, and are both modeled as PI at each material's corresponding density. The vacuum is modeled as PI, at an extremely low-density. Note: the perturbation is not drawn to scale.

ten OMEGA beams used in the experiment as four distinct beams at angles chosen according to the distribution of incident angles of the real beams. The power of each simulated beam is then weighted accordingly, as one incident at 50°, three at 42.0°, four at 31.7°, and two at 10.2°. Finally, because of discrepancy between the CRASH laser physics model and the experimental results, the laser energy must be scaled by

some factor, which we shall refer to as the laser scaling factor (LSF), in order to give shock positions consistent with experimentally-measured values. For typical HED experiments, the LSF ranges from around 50% to 100%. This scaling factor accounts for three-dimensional effects missing in the two-dimensional simulation, as well as error introduced by assumptions made by the code in modeling the relevant laser-plasma-interaction physics. The scaling will be discussed in more detail in section 5.7.

At the end of the pulse, the simulation shows the shock as having advanced 75 μm into the disk, and the rarefaction following the pulse's end catches up to the shock by $\sim$ 2ns, allowing a blast wave to form just before shock break-out from the disk and into the foam, occurring at 2.4 ns. A density map taken from the CRASH output at this time is shown in Fig. 4.11, and a radiograph simulated from the information in this density map combined with known X-ray material transmission properties is shown in Fig. 4.12. Note that these are the same conditions under which the data in Fig. 4.8 was obtained.
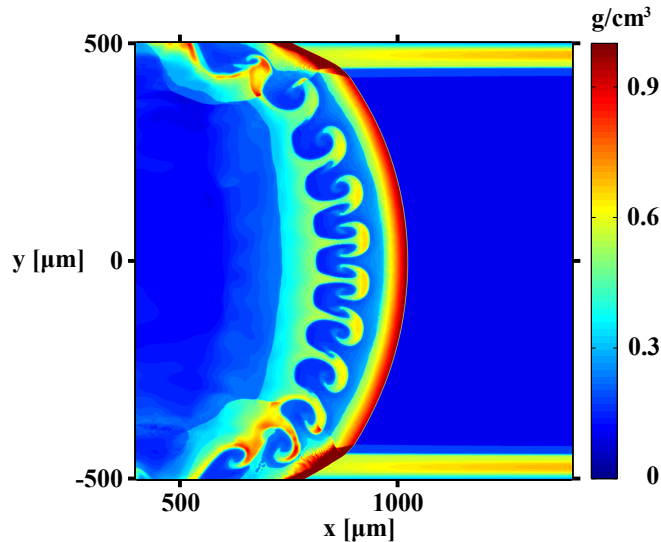
Figure 4.11: A density map of the simulated system, corresponding to the data image in Fig. 4.8.
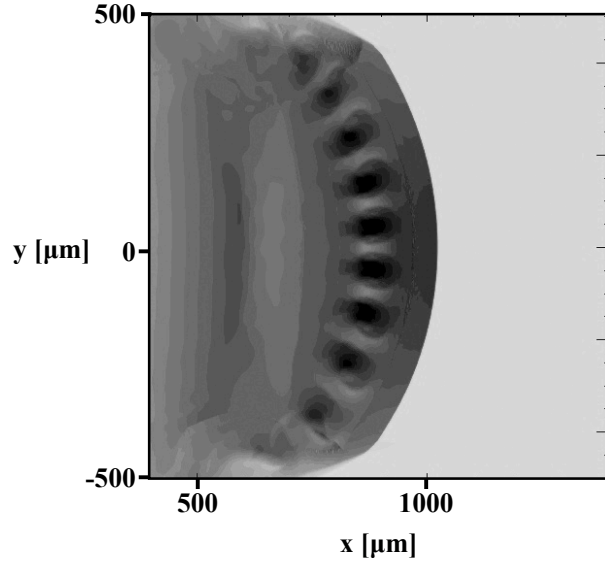
Figure 4.12: A simulated radiograph of the same system shown in Fig. 4.8, starting from the density map in Fig. 4.11. The image is then processed to account for photon attenuation and typical signal levels to produce the contrast shown.

4.3.4 Discussion

In order to assess the performance of the simulations, identical runs were performed with varying LSFs for each CRF-density case. Fig. 4.13a shows the result for the 0.1 g/cm^3 case, overlaid upon the best-fit data curve. For this system, the data
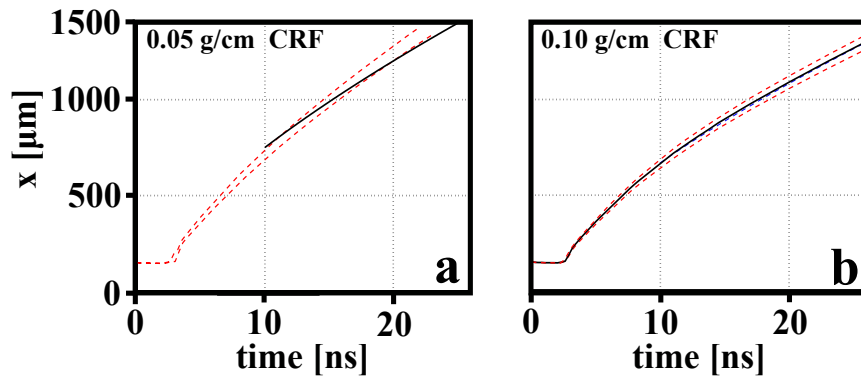
Figure 4.13: a. Data best-fit curve (solid line) overlaid upon simulated trajectories (dotted lines) that bound the data curve for times at which data exists, for systems with 0.05 g/cm^3 CRF; b. Data best-fit curve (solid line) overlaid upon simulated trajectories, for systems with 0.1 g/cm^3 CRF. The simulated trajectories also serve to demonstrate the sensitivity of the blast-wave trajectories to the LSF.

curve is well-bounded by simulated trajectories with LSFs of 0.725 and 0.75. The separation between these two curves, at times for which experimental data exists, varies from 12 μm at early times to 18 μm at later times, implying that the simulation fits the experimental curve to about $\pm$ 6 μm for an LSF of roughly 0.74. In Fig. 4.13a, simulation curves with LSF of 0.7 and 0.8 are shown alongside the data curve, to illustrate the sensitivity of the shock trajectory to LSF.

The same results are shown, for the 0.05 g/cm^3 case, in Fig. 4.13b. In this case, the trajectories predicted by the simulation do not match the experimentally-observed results as well as in the previous case. However, for times at which data is available, the curve is bounded by simulated trajectories with LSF of 0.675 and 0.775. On average, a curve with LSF of 0.725 most closely agrees with the data, to within approximately $\pm$ 35 μm. The drift of the simulated shock trajectory away from the best-fit curve to the data is, nonetheless, small compared to the shot-to-shot variation in the experimentally-observed shock locations.

Finally, it is worth briefly mentioning the influence of the initial perturbations on the subsequent behavior of the blast wave. The shock travels, in the plastic, at approximately 60 μm/ns, and thus traverses the 5-μm peak-to-valley region of the perturbation in around 100 ps. This is very short compared to the global time scale of the experiment. The shock quickly stabilizes itself to any deformation it experienced in crossing the perturbed interface, and we therefore expect the overall effect on the shock location and speed to be inconsequential. This was confirmed by a new simulation done in CRASH, identical to those described here, but with an initially-flat interface. This simulation predicted identical blast-wave trajectories as simulations with perturbed interfaces.

4.3.5 Conclusions

In this work, we were able to simulate, using CRASH, the propagation of a HED blast wave through a plastic-ablator/CRF cylinder system and, because the various experiments were identical with the exception of the CRF density, we were able to compare the relative performance of the simulation at differing foam densities. The optimal LSF, which scales the input laser energy (and therefore also the strength of the driven shock) to compensate for 3D and laser-material interaction effects that the simulation cannot adequately capture, had a roughly similar value between the two cases we have compared, around 0.725-0.75. This gives us confidence that, in the design of future experiments employing plastic ablators under similar irradiation conditions, this scaling factor can be used with CRASH to provide a good estimate of how the shock will propagate.

CRASH's ability to predict shock propagation could be further tested by incorporating data from future experiments employing different CRF densities. One of the principal limitations of this analysis is the difficulty in correctly model the foam–especially at lower densities–and the availability of more data at other densities could help increase our confidence in the validity of simulated shock trajectories. Experiments designed expressly to measure shock breakout from plastic ablators would also provide valuable confirmation of the results presented here.

CHAPTER V

Hot-electron generation in laser-driven systems

5.1 Introduction

The work presented in this chapter was performed on the Titan laser, and is adapted from a manuscript intended for submission to *Physics of Plasmas* entitled "Observations of energetic electron propagation after picosecond laser irradiation." My role in this experiment was to lead the experimental effort, both in designing the experiment and in executing it at the JLF at LLNL. This experiment represents a departure from typical aspects of the experiments described elsewhere in this dissertation, including the physics, the diagnostics, and even in terms of the fundamental nature of performing an experiment on Titan, in which the researchers are required to perform much of the physical work of preparing the laser system and executing the experiment, versus performing an experiment on OMEGA-60 or OMEGA-EP, in which the researcher primarily interfaces with the professional engineering staff at the facility. The experiment is, nonetheless, highly relevant to the main theme of this dissertation, for reasons described in Chapter I.

5.2 Experimental background

The interaction of a laser pulse with a material produces a stream of high-energy electrons by a variety of physical processes [102]. Under certain conditions, these processes can lead to a significant fraction of the laser energy, up to several tens of percent, being converted into the kinetic energy of such electrons [44, 101], and with modern laser technology, the characteristic energies of typical streams can be MeV or larger [88, 6, 68]. Such an electron stream can have a considerable effect on nearby materials, which can either be a useful feature, for example as a possible method to significantly increase fusion fuel heating in the fast-ignition concept [42, 68, 44, 93], or a complicating factor in experiments involving a laser drive, where for example hot-electron heating can alter precisely-chosen initial conditions [56] or introduce noise signal in imaging diagnostics [48, 46], thereby degrading data quality.

The prevalence of electron streams in experiments involving lasers makes it highly desirable to understand, and thereby attempt to control, them. The exact mechanisms behind these phenomena, their dependence upon the intensity of the irradiating laser, and the resulting energy spectrum and directionality of the produced electrons remain challenging to fully understand [42]. It is in this context that we report the present work, in which we observe the propagation of high-energy electrons away from an irradiated material. These experiments were performed by using the Titan laser to irradiate a metal wire. The interaction between the consequent electron stream and nearby spectator wires, placed in various configurations, causes the spectator wires to fluoresce at their characteristic K energies, and we then measure this secondary X-ray fluorescence.

Because these spectator wires are placed at varying distances from the irradiated wire, and by forcing the electron stream to traverse various media to reach the spectator wires, we can use the measured fluorescence of the spectator wires to infer information about the energy spectrum of the incident electron stream, as well

as its directionality, due to the varying dependence of these geometrical effects with electron energy. Further, by imaging the emission of the system, we are able to observe to some extent the travel path of these electrons, which tend to not exhibit straightforward behavior due to their high characteristic energies. The present experiments complement previously reported results [88, 86] investigating the fluorescence of similar systems under other variations.

In particular, the previous results suggest that the strong oscillating electric field associated with the irradiating laser tends to couple to the electrons in the material, consequently influencing both the electrons' direction of propagation and their kinetic energy [88]. Electrons coupling to the laser's electric field are more likely to propagate along the direction of the laser's polarization, and tend to be accelerated to a range of energies, at least up to roughly MeV order. The goal of these experiments is to explore the extent of this coupling, using the observed fluorescence of wires at differing distances and separated by different media to assess the electrons' divergence from the laser spot, as well as any scattering–the likelihood of which depends on the electrons' energies–as they propagate through the intermediate material.

5.3 Experimental conditions

The main experimental system, shown in Fig. 5.1, consists of three elemental metal wires, 0.5 mm in diameter and 3 mm long, mounted onto a substrate. We will subsequently refer to this as system A, in contrast with a second experimental configuration to be described shortly. The axes of these wires were oriented horizontally, parallel to the **y** direction in Figs. 5.1b and 5.1c. The three wires were also coplanar with each other and the vertical direction, corresponding to the **y-z** plane in Figs. 5.1b and 5.1c. They were organized in this manner because the irradiating laser beam is polarized vertically, corresponding to the **z** direction in Figs. 5.1b and 5.1c. The result is that the upper and lower (spectator) wires lie along the polarization direc-
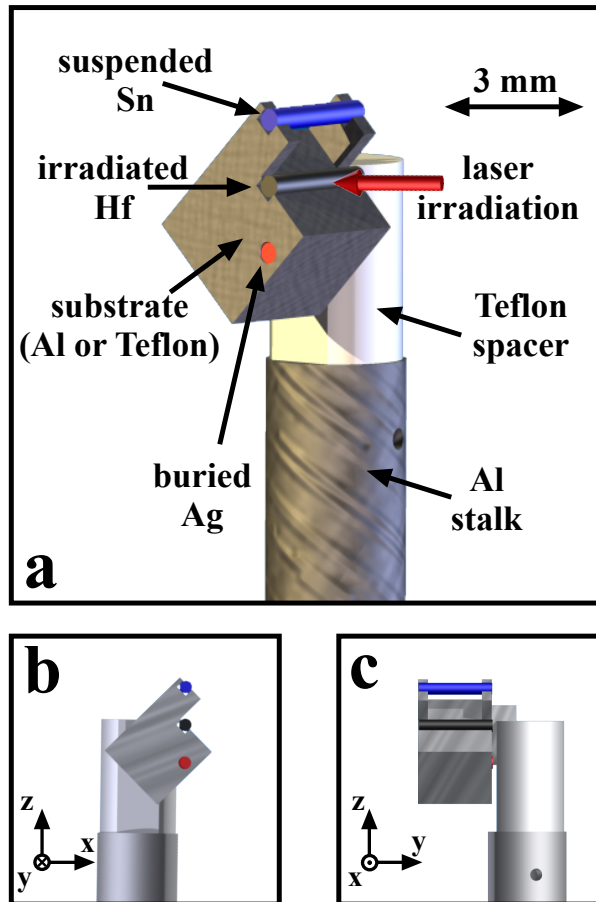
Figure 5.1: Geometrical configuration of the experimental system A. The direction of the laser's polarization corresponds to the direction labeled **z** in frames b and c.

tion relative to the center (irradiated) wire. The substrate was designed such that the center wire was embedded upon its surface, pressed into a rut of depth 0.25 mm, such that approximately half the wire protrudes above the substrate surface. Meanwhile, the lower wire was completely encased by substrate material, and the upper wire was suspended from two struts. The idea is that the direct path between the irradiated and suspended wires traverses vacuum, and the direct path between the irradiated and buried wires traverses substrate material. In some cases, the substrate was made of Teflon, and in others it was made of aluminum. These two materials represent extremes of high and low resistivity, respectively, and were chosen to help isolate resistive effects upon electron propagation. The outer-edge-to-outer-edge spacing of the wires was also varied, from 0.5 mm in some cases to 1.0 mm in others. The experiments were conducted using silver as the suspended wire and tin as the buried wire. As a comparison, in some cases the higher-Z materials dysprosium and gadolinium were used in place of silver and tin, respectively.

The hafnium wire is irradiated by a single Titan 1053-nm laser pulse, nominally at an energy of 100 J and of 1 ps duration, focused to a nominally-10-μm-diameter spot. The interaction of the laser with the hafnium generates a stream of electrons, some of which propagate towards the silver and tin wires, in turn causing these wires to emit X rays at their characteristic $K\alpha$ and $K\beta$ energies. These two materials (as well as the dysprosium/gadolinium pair) were chosen for resolvability of their K lines by the diagnosing X-ray spectrometer, while their relatively low Z permits stronger K-line emission due to the larger cross-section for K-shell ionization [45].

A second, different system geometry was also employed, which we will refer to as system B. A schematic of this system is shown in Fig. 5.2. In this system, the irradiated hafnium wire is centrally located and lies along the laser beam axis. Therefore, refluxing electrons propagate into the target, away from the spectator wires. Spectator wires of gadolinium and dysprosium are oriented around this central wire either
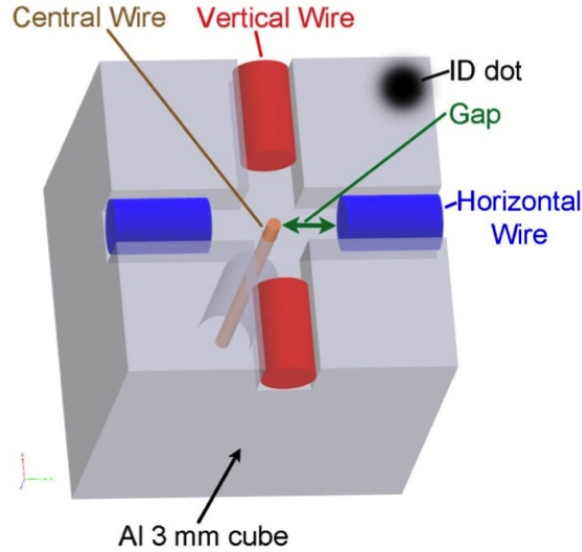
Figure 5.2: Schematic of system B. In this system, the irradiated hafnium wire is central and roughly coaxial with the laser. Wires of two distinct materials, dysprosium and gadolinium, are oriented either vertically or horizontally, corresponding to an orientation along or orthogonal to the laser's electric field. The wires are embedded in an aluminum substrate.

in a vertical or horizontal orientation, such that they either lie along the laser's oscillating electric field or orthogonal to it. The spectator wires are placed such that their tips are at a fixed distance from the irradiated wire, either 0 mm (that is, the wires are in contact), 0.4 mm, or 0.8 mm. Finally, the spectator wires' lengths are such that the wire extends to the edge of the substrate. Therefore, the lengths of the wires are roughly 1.25, 0.85, and 0.45 mm for the spacings 0, 0.4, and 0.8 mm, respectively.

5.4   Experimental results

The primary diagnostic was the Lawrence-Livermore Crystal Spectrometer (LLCS) [87], a transmission crystal spectrometer employing a cylindrically-curved (10-11) quartz crystal, with a 254-mm radius of curvature, in a Cauchois [13, 85] geometrical configuration, producing spectral images upon two imaging plates, one located on the Rowland circle and another 200 mm behind the Rowland circle. Fig. 5.3a shows an

example of a raw data image obtained by LLCS from system A. The brightest lines,
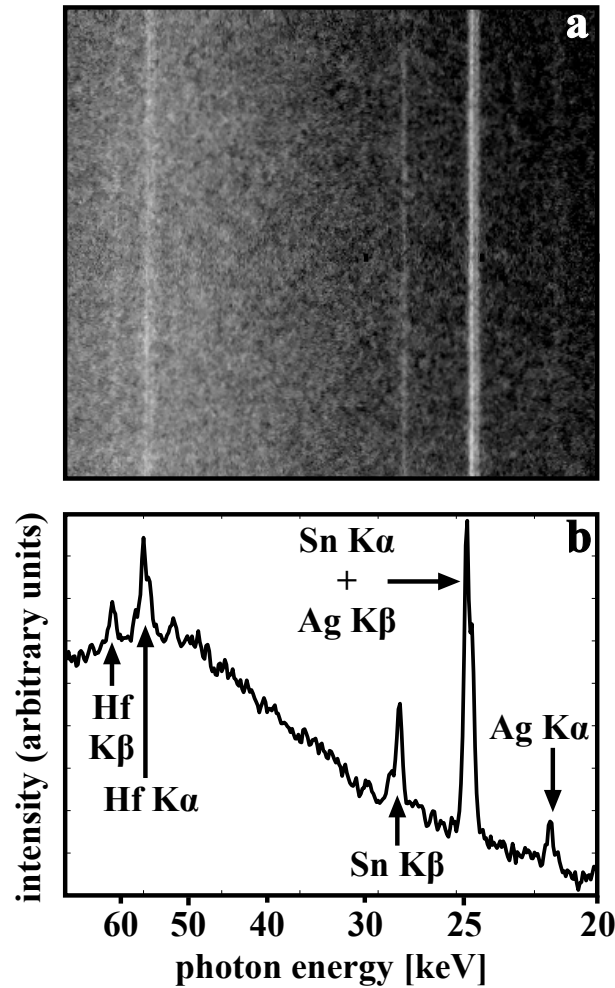
Figure 5.3: a. Raw data image of system A. Because the spectral lines are nominally uniform in the vertical direction on the imaging plate, it is possible, for most observable lines, to obtain a robust signal-to-noise ratio despite the large amount of noise present; b. Horizontal line sample of the data in frame a. The sample was averaged over a vertical region of 400 pixels, corresponding to 2 cm on the imaging plate. The K-shell emission lines are clearly discernible for all three wire materials, except for the Ag Kβ lines, superposed upon the Sn Kα ones.

corresponding to the tin Kα and Kβ, and the hafnium Kα, are clearly visible. The silver Kα and hafnium Kβ are also present, though more difficult to resolve. However, the spectrometer's crystal only disperses in the horizontal direction, enabling us to average the lines in the vertical direction. Averaging in this manner over the entire

lines results in a robust signal-to-noise ratio. Finally, the resulting signal can be calibrated to actual photon counts per pixel on the detector, by taking into account the energy-dependent properties of the imaging plate's sensitive layer and the scanner's response to it [61, 55].

Fig. 5.3b shows the result of this method for the data in Fig. 5.3a. Although there is significant background signal present, the background's large-scale structure is mathematically smooth, permitting it to be easily removed, while small-scale noise fluctuations are small compared to the overall signal due to each spectral line. Approximating the uncertainty due to noise by measuring the fluctuations about second-order polynomial fits to the background near the lines, we find typical measurement uncertainties of roughly 1% for the brightest lines and roughly 5-8% for the faintest lines. It turns out, as will be discussed further in section 5.7, that normal shot-to-shot variations in observed signal is a much more important source of uncertainty than the measurement technique used to obtain the signal's value.

It is well-known that spectral lines tend to broaden in a Cauchy-Lorentz profile, and in the case of the data in this work, this causes many of the lines, especially the split lines of our various materials' $K\alpha$ doublets and $K\beta$ triplets, to convolve on the detector. Fig. 5.4 shows this profile for a pair of Hf $K\alpha$ lines from LLCS data, in which the data has been converted into physical units and the local background has been subtracted according to the method described above. In this figure, the data are shown in black points, while the red curves show the individual $K\alpha_1$ and $K\alpha_2$ lines, iteratively determined such that their sum, shown as a black curve, produces the best fit to the data using a least-squares method and the knowledge that the overall curve should be the superposition of two Cauchy-Lorentz curves, one for each $K\alpha$ line present. In this manner, we find that the data produces the correct $K\alpha_1/K\alpha_2$ ratios corresponding to well-known, tabulated values [36]. These ratios are quantum-mechanical in nature and not affected by the particular details of our experiments.
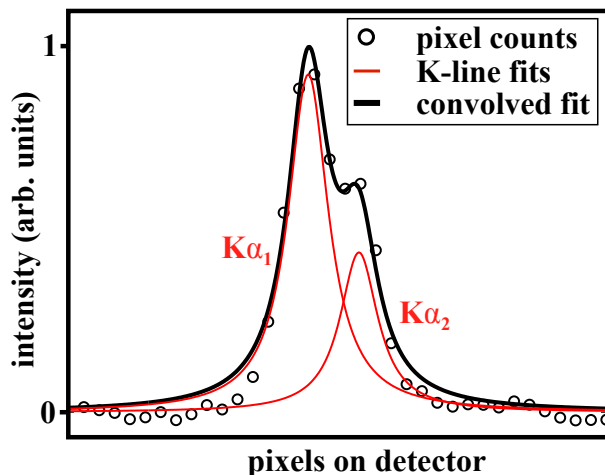
Figure 5.4: Hafnium $K\alpha$ lines from LLCS data, with background signal subtracted. The observed double peak is the result of two superposed Cauchy-Lorentz distributions on the detector, one due to each line in the $K\alpha$ doublet.

The overall curves are therefore simply the sums of the signals from lines present in well-known ratios, and the overall signal can be measured by simply adding the values of each pixel in the peak. Therefore, for simplicity, we will refer to the overall $K\alpha$ and $K\beta$ signals and not to the individual split lines.

Finally, the LLCS diagnostic also records a pinhole image of the experimental system's fluorescence. These images are useful for identifying the locations from which the fluorescence originates, which provides insight into the electron stream's propagation path through the system. An example of these pinhole images and the information they provide is shown and discussed in Fig. 5.5.

Fig. 5.5a shows an image of system A's self-emission, produced by the LLCS diagnostic's alignment pinhole. A rendering of LLCS' view of the system is shown in Fig. 5.5b for reference. In Fig. 5.5a, a hot spot, visible at the image's center, corresponds to the location of the laser's irradiation of the Hf wire. Emission from the spectator wires is also present. Although emission from the entire length of the spectator wires is visible, the emission is visibly stronger near the center of suspended wire, directly above the irradiated wire. Similar behavior is observable from the buried

99
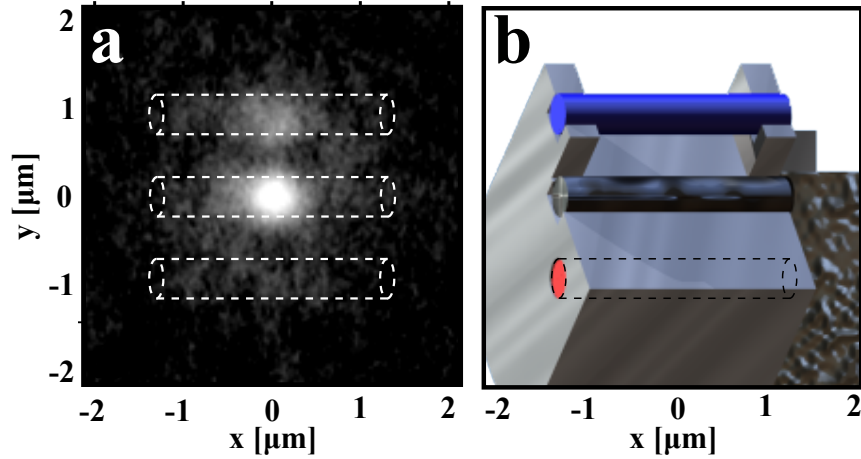
Figure 5.5: Pinhole image of system A captured by the LLCS diagnostic. The image, foreshortened about 8% in the horizontal direction due to LLCS' angle of view, shows the irradiation spot at its center, a hot spot at the center of the suspended wire directly above it, and weaker emission along the full lengths of all three wires.

wire, although the overall weaker emission from this wire makes it more difficult to identify. These general characteristics are consistent across data from all iterations of the experiment.

Fig. 5.6 shows the measured emissions from the spectator wires. In this figure, the
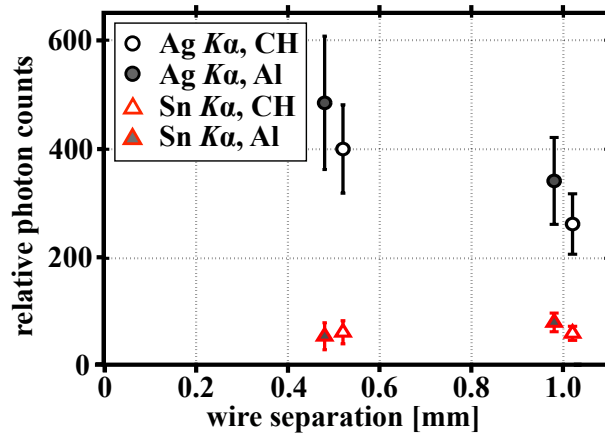
Figure 5.6: Secondary fluorescence recorded by LLCS for the four main experimental configurations of system A. The signal from the suspended spectator wires is shown as black circles, while the signal from the buried wires is shown as red triangle. White-filled points indicate Teflon (CH) substrates, while gray-filled points indicate aluminum substrates.

100

measured $K\alpha_1+ K\alpha_2$ emission is shown for each configuration of the system. Signal from the suspended wires is plotted as black points, while signal from the buried wires is plotted as red points, and the substrate material is indicated by the fill color of the datapoint, white for Teflon and gray for aluminum. Each configuration was repeated 5 times, and the plotted points are the mean of the measurements within each configuration, while the associated uncertainties shown are the standard deviation of those measurements. The two configurations at each individual wire spacing are slightly offset from the 0.5 and 1.0 mm locations along the abscissa for readability.

The system was also diagnosed using three Electron Positron Proton Spectrometers (EPPS), located in the horizontal plane and at angles of 60°, 140°, and 180° from the direction of incidence of the laser. The EPPS diagnostic employs permanent magnets to deflect incoming charged particles at angles that vary according to their energies, and the particles' deflected trajectories are then recorded on imaging plates. Confidence of the source of electrons arriving at the detector was limited to energies above 2 MeV. Distortions in the signal below 2 MeV indicates that these electrons may not be emanating directly from the laser irradiation event, which could occur, for instance, due to lower-energy electrons refluxing through the target or being influenced by strong electromagnetic fields generated on the surface of the system. The three curves in Fig. 5.7 show an example of the spectra generated by irradiation of System A.

5.5 Measurement considerations

5.5.1 Spectator emission model

Because the spectator-wire pairing choice convolves the Ag $K\beta$ and the Sn $K\alpha$ lines, we wish to confirm that we can regard the emission as cold in order to extrap-
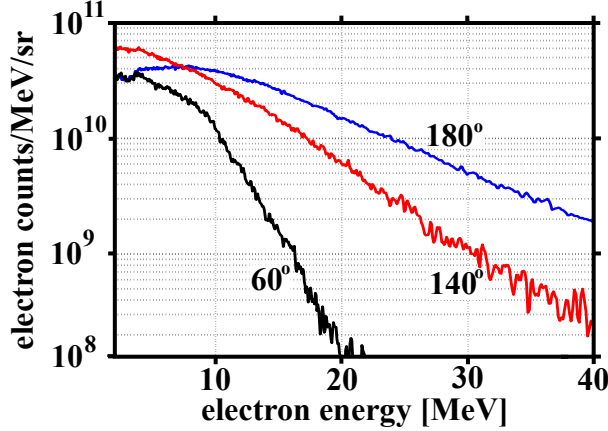
Figure 5.7: High-energy (>2 MeV) electron spectra measured by the EPPS diagnostic in the horizontal plane, measured at various angles from the laser's direction of incidence. This data provides direct evidence of the generation of high-energy electrons, as well as direct evidence of their directional dependence.

olate the strengths of the individual lines. To do so, we chose to irradiate a piece of indium with a Ag spectator wire nearby, as the K lines for these two materials do not overlap. The Ag spectator wire had a $\sum K\alpha / \sum K\beta$ ratio of 5.35, in close agreement with the theoretically-predicted cold-emission ratio of 5.26. Therefore, we are confident that we may deconvolve the Ag and Sn K-lines according to the predicted value of the Ag $K\beta$ line strength corresponding to our measurement of the Ag $K\alpha$ line strength.

5.5.2 Electron-stream isotropy

Previous work [84, 88] established that typical energies of generated electrons in this kind of system, under weaker irradiances than the present experiments, are of roughly 0.5-1 MeV. In this energy range and higher, elemental K-shell ionization cross-sections are roughly independent of the incident electron energy [45]. Here, we will use the values $\sigma_{Ag} = 48$ b and $\sigma_{Sn} = 41$ b. Because the spectator materials were always 0.5-mm-diameter wires in their standard, elemental solid state, we can write

the overall areal cross-section σ_T of the wires as follows:

$$\sigma_T = 0.625 \frac{\rho[\text{g/cm}^3]d[\text{cm}]}{A_r[\#]} \cdot \sigma[\text{b}], \tag{5.1}$$

where ρ is the wire's solid density, d is the wire's diameter, and A_r is the wire's relative atomic mass. Then, $\sigma_{TAg}/\sigma_{TSn} = 1.85$, indicating that we should see this relative emission between these two wires if they are subjected to similar electron streams.

To determine whether the upper and lower spectator wires are in fact subjected to similar electron streams, substrate effects aside, we conducted an experiment with a system geometrically similar to the main experiments, but with no substrate. An image of the resulting wire array is shown in Fig. 5.8a. The recorded spectrum from
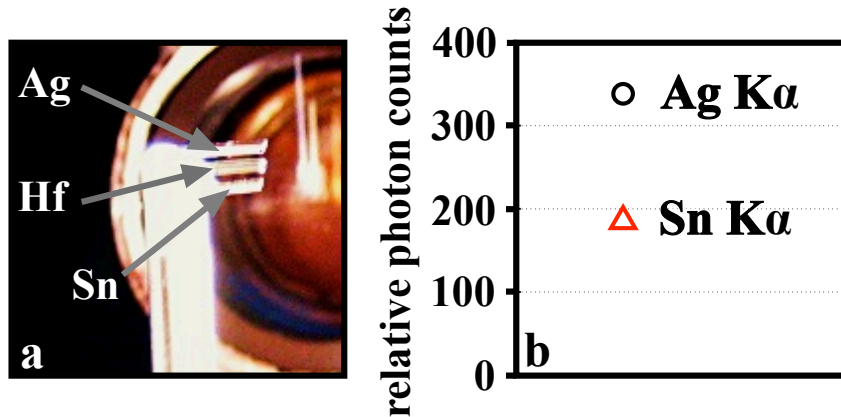
Figure 5.8: a. A three-wire system, featuring irradiated hafnium and spectator silver and tin. This is geometrically identical to System A, but without the substrate; b. Spectrum from a three-wire, no-substrate shot. Open circles mark the inferred values of the the convolved Sn Kα and Ag Kβ signals.

this system is shown in Fig. 5.8b. The Ag to Sn Kα ration is 337/184=1.83, in good agreement with the predicted result.

5.5.3 Equivalence of electron-stream conditions under varying target geometry

Fig. 5.9 shows the measured emission from the irradiated hafnium wire in the experiment. The presentation of the irradiated-wire data in this figure is similar to
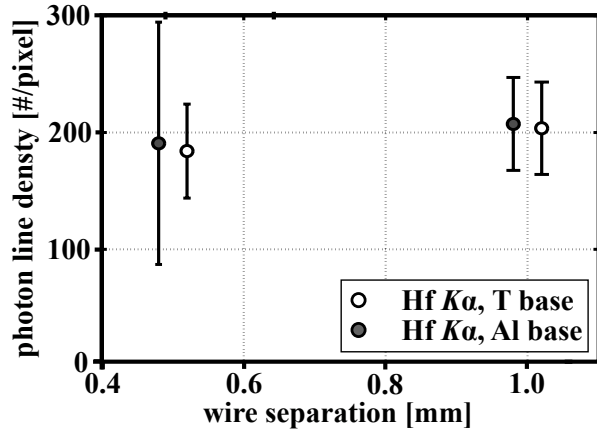
Figure 5.9: Secondary fluorescence recorded by LLCS from the irradiated hafnium wire for the four main experimental configurations.

that described for the spectator wires in Fig. 5.6.

Interestingly, although there is significant shot-to-shot variation in the recorded emission, when averaged over the set of shots in any given configuration, the overall variation is approximately ±5%. This suggests two things: first, that the emission from the irradiated wire is due to the interaction of the laser with the material and is independent from other differences in the system's configuration, and second, that the shot-to-shot variation is the result of consistent variation in the way that the electron stream is generated from the laser's interaction with the hafnium wire. The independence of the emission from the irradiated wire is supported by the results of previous, similar experiments and further implies that the electron stream generated by this irradiation event is also independent of other aspects of the system's configuration [88]. Finally, we do not believe that this variation is a result of variation in the energy profile of the delivered laser pulse. The strength of the measured Hf K lines

over 20 repetitions was statistically independent both of the delivered laser energy and the amount of laser prepulse present, as discussed in Appendix 5.6. This result is also theoretically supported [70].

5.6 Correlation of laser energy and pre-pulse energy to emission

Figs. 5.10a and 5.10b show the intensity of the Hf Kα line for each repetition of the experiment, plotted against the total energy delivered by the laser pulse and against the energy contained in the laser prepulse, respectively. No further information about
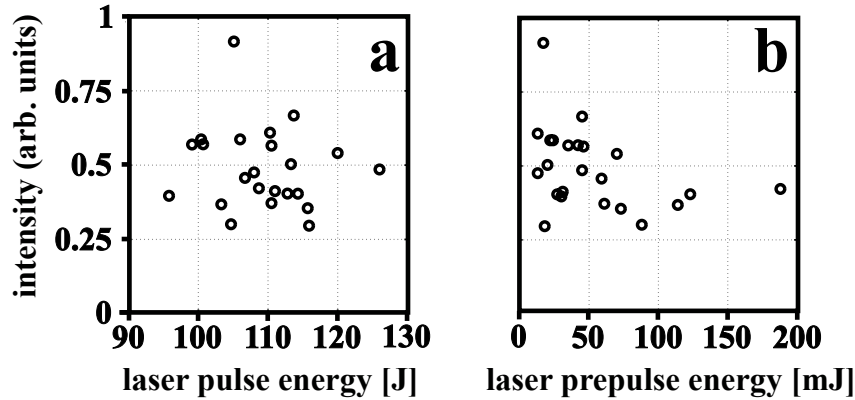
Figure 5.10: a. Hafnium line strengths as a function of the total laser energy delivered; b. Hafnium line strength as a function of the energy contained in the laser pre pulse.

the temporal profiles of the prepulses, other than their total energy, was available. There is no correlation between the total energy delivered and the strength of the Hf line (a P value of 0.14), while a weak correlation is observed between laser prepulse and a slight decrease in Hf line strength (a P value of 0.38), although there were very few occurrences of large ($>$100 mJ) pre pulse. Finally, because the Kα ionization cross-section is very weakly dependent upon electron energy for most energies of interest (of order 100 keV and above) [45], these correlations are tied closely to the total number of electrons coupling to the laser, and are insensitive to the energy

spectrum of those electrons.

5.7   Discussion

Based on a purely geometrical consideration, we expect the X-ray signal from the the spectator wires in the 1.0-mm-spacing to be roughly half that from the wires in the 0.5-mm-spacing, if the electrons are expelled from the irradiated wire isotropically, and do not experience significant attenuation or scattering as they propagate. This assumes the X-ray emission by the spectator wire is also isotropic, and that the spectator wire is long in one direction, properties which lead to a $1/r$ scaling for wire separation r. In fact, we observe the emission to be much less disparate than this. For the suspended wires, the difference is roughly a factor of 1.5, while for the buried wires we observe no difference. This apparent insensitivity of the buried wire emission to wire spacing and substrate material, coupled with the less-than-expected difference in emission from the suspended wires, suggests that the directionalities of different components of the electron energy spectrum have asymmetries. These asymmetries can be explained by the effect of the coupling of the laser's electric field to the electrons.

In order for an electron to propagate through 0.5 mm or 1.0 mm of aluminum without being scattered or attenuated, it must have an initial energy of at least 0.25 MeV or 0.5 MeV, respectively. Beyond this, Monte Carlo simulations [86] indicate that, for a beam of 1-MeV electrons, approximately 80% will be scattered away through 0.5 mm of Al, and more than 95% will be scattered away through 1.0 mm of Al. This suggests two effects that a high-energy tail would have on the observed emission, consistent with the data results. First, signal from the buried spectator wire would not be affected by changes in the electron propagation path, because the low-energy part of the spectrum is attenuated by the substrate material, while the high-energy part is neither diverging nor being fully stopped by the substrate, and

therefore the wire separation distance does not affect the fraction reaching the buried wire. This means the weak dependence of the spectator wire's K-shell ionization cross-section with electron energy results in similar photon emission. Second, dependence of the signal from the suspended wires on wire separation distance should be weaker than expected from geometrical arguments, because there is both a contribution from diverging lower-energy electrons and directional higher-energy electrons. These points are consistent with the idea that strongly-coupled electrons would get more kinetic energy from the laser while being preferentially accelerated along the direction of the laser's electric field, while weakly-coupled electrons would get less kinetic energy and be more likely to be accelerated in other directions, perhaps due to scattering or other mechanisms.

Further evidence of a high-electron-energy component of the spectrum is given by the electron energy spectra recorded by EPPS. The three curves shown in Fig. 5.7 provide direct evidence of the generation of high-energy (>2 MeV) electrons during irradiation of the Hf wire, and of their directional dependence, especially at energies on the order of tens of MeV. It was only feasible to make these measurements in the horizontal plane, perpendicular to the direction of laser polarization. Further, it was not possible to use this diagnostic to resolve electrons of energies less than roughly 2 MeV, a portion of the spectrum which includes a significant portion of the electrons responsible for the X-ray fluorescence observed by LLCS.

Fig. 5.11 shows the fluorescence image from a system consisting of two wires, one silver and one tin, and no substrate. The critical difference between this system and the one shown in Fig. 5.5 is that the irradiated wire is low-Z silver rather than high-Z hafnium. The overall K-shell ionization cross-section for electrons is therefore significantly larger than with an irradiated hafnium wire; therefore, we expect to see more fluorescence due to any refluxing of electrons within the wire. Further, because the system does not have horizontal symmetry, we are able to determine whether the
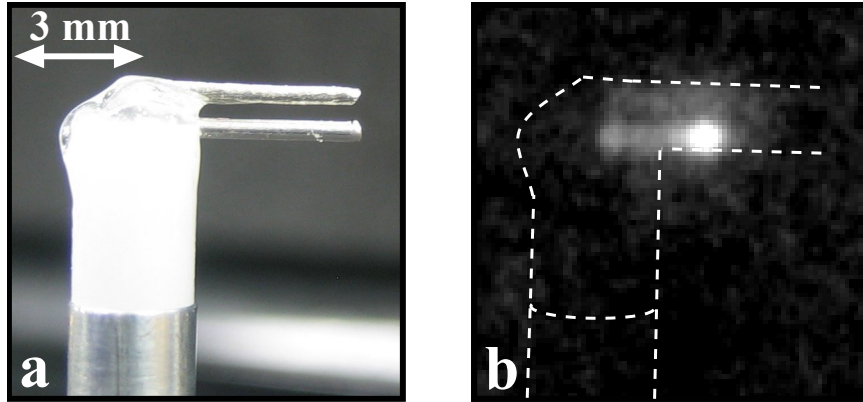
Figure 5.11: a. A two-wire system, featuring irradiated silver and spectator tin. The epoxy used to anchor the wires to the spacer, visible in the upper left corner of the image, is low-Z and almost completely transparent to the wires' $K\alpha$ emission; b. LLCS pinhole image of the system in Fig. 5.11a. The image clearly shows fluorescence along the irradiated wire, from the laser spot towards the stalk, and along the spectator wire, from the stalk to roughly the location above the laser spot. The lack of a hot spot on the spectator wire is likely a result of the lower-Z irradiated material compared to the system in Fig. 5.8, resulting in a weaker generated electron stream.

attachment points of the wires affect the propagation of electrons.

In the figure, the lower wire is the irradiated silver, and the upper wire is the spectator tin. The irradiated spot is clearly visible, as is weaker emission from other parts of the wires. In particular, although the irradiated spot was in the center of the exposed wire, emission is only observed extending from the irradiated spot towards the stalk. This indicates that electrons are propagating preferentially in that direction, and not towards the unsupported end of the wire, despite the fact that the teflon stalk tip and polymer attachment glue are strong insulators. Furthermore, it indicates that there is a component of the observed fluorescence that is due to electrons arriving to the spectator wire via refluxing through the system, rather than through the electron stream emitted by the irradiated wire.

To further test the directionality of the electron stream, we compare results from system A, shown in Fig. 5.1, with results from system B, shown in Fig. 5.2, all

performed with the same combination of irradiated hafnium wires and spectator dysprosium and gadolinium wires. The critical differences between these two systems is that the orientation of the irradiated wire in system B results in refluxing electrons traveling into the system rather than along its surface, and that system B's spectator wires are oriented such that they only present a small cross-section to the emitted electron stream, localized either in line with or orthogonal to the laser's oscillating electric field.

Results from both systems are shown in Fig. 5.12. In this figure, the data from
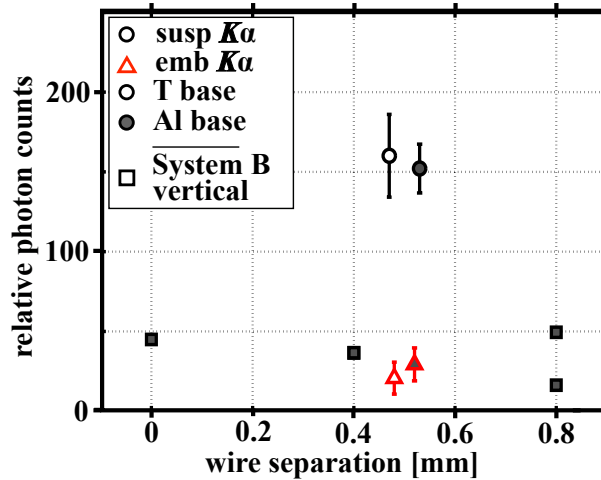
Figure 5.12: Spectator wire signal from systems employing dysprosium and gadolinium spectator wires. Data from system A are shown at 0.5 mm of wire separation, and slightly offset for readability. Data from system B are presented along the abscissa at their correspond wire separations of 0, 0.4, or 0.8 mm.

system A is presented in the same format as that described for Fig. 5.6, except in the present case we only performed the experiment with 0.5-mm wire separations. The data corresponding to system B is presented as open shapes without uncertainties shown, since the uncertainty in the measurement itself is about the size of the plotted points. In the latter case, the signal from the spectator wire aligned with the laser's electric field is plotted as black squares, while the signal from the wire orthogonal to the electric field is plotted as red triangles.

The measured signal from the vertical wire in system B is significantly reduced compared with the emission from the vertical wire in system A. This is suggestive of a highly-directional component to the electron stream. Since we expect the electron stream to be generated by the laser/material interaction event itself, and the wire is in both cases massive, the streams should be similar. The lack of a significant dependence of observed fluorescence from the spectator wires with wire separation, coupled with its correspondence roughly to the amount of signal seen from the buried wire in the first configuration indicates that the responsible electrons are confined to a narrow cone.

5.8 Conclusions

The experiments we present here provide information about the spectral content of an electron stream generated by the interaction of a laser with a metal. The behavior of the electrons as they propagate through space and various media is dependent both on their initial energy and on their directionality, and therefore by measuring secondary fluorescence from materials placed in different configurations, we can infer some of these properties of the electron stream. The secondary emission observed by varying the distance and separating media of the irradiated and spectator wires suggest two properties of the electron stream. First, there are higher- and lower-energy components of the electron stream with roughly MeV characteristic energy. Second, the high-energy component tends to be more strongly directional than the low-energy component. This behavior is consistent with what we would expect from the electrons' coupling to the laser's electric field. Future work, designed to isolate the spectral components and explore their directional effects, would provide more evidence of the electron stream's propagation.

CHAPTER VI

Conclusions and future directions

6.1   General thoughts on laser-driven HED experiments

Experimental HED physics has the capability to make unique contributions to both technology and our understanding of the natural world, as by its nature the types of processes that fall under the category of HED tend to occur under conditions that make them difficult to access experimentally. Their interest, further, oftentimes lies in the fact that these conditions cause the relevant systems to behave in markedly different ways than analogs in our everyday experience might suggest. The development of techniques, such as the use of a laser to deposit energy combined with radiographic and spectroscopic diagnostics as described in this dissertation, to control and study different aspects of these processes has been vital for efforts to harness nuclear fusion as a viable energy source, as well as for understanding the ways that stars, planetary interiors, and many other natural systems behave.

A recurring theme in HED physics is the fact that the overall physical properties of the systems–including their high pressures, densities, and temperatures, as described in Chapter I–and, in many cases, the methods used to achieve these properties (e.g. laser irradiation) tend to be directly responsible for the systems' most interesting behaviors. In this sense, the experiments presented in this dissertation represent simplified, isolated aspects of the complex natural and technological systems we ul-

timately seek to understand, in which the overall HED nature of each experimental system is tweaked to highlight the particular physics of interest to that experiment. In the case of Chapters II–IV, the experimental physics are direct aspects of the dynamics that occur in real-world systems, while in the case of Chapter V, the physics occurs as a typical side effect of the creation of laser-driven HED systems.

The collection of these experiments represent my contributions to the study of HED hydrodynamics, as well as to experimental techniques relevant to HED physics. The experimental efforts focus on different physical mechanisms, and the conclusions and opportunities for further work for each are summarized below. However, there are also general conclusions about these kinds of experiments that we can draw, and these are presented first.

For example, subtle changes in the initial conditions can have profound effects on the dynamics, and can even alter the dominant physical mechanism acting on a system. The experimental consequence is that the initial conditions must be precisely chosen to ensure that one is actually observing the intended behavior. The experiments described in Chapter III are a particularly illustrative case of this, as the observed growth makes no sense and is impossible to predict without these considerations.

Further, in even the most controlled system, secondary processes can arise and affect the observed dynamics. For example, in laser-driven RT experiments, expansion of the high-pressure system often accounts for a significant fraction of observed interface growth, and in the experiments described in Chapter IV, we show how expansion might lead to the breakup of growth features altogether. As another example, the design of the experiments described in Chapter II represent the current state in ongoing work to isolate RM physics from various complicating factors, including decay of the shock conditions, RT growth, and finite-thickness effects, to name a few.

6.2 Experiment-specific conclusions

In Chapter II, I presented work I did executing the first experiments on a new platform, allowing observation of two-mode RM growth through various phases of behavior, all of them occurring under steady shock and flow conditions. In the linear period, the experiment proved able to resolve the earliest-time transient behavior of the growth rate, in which it increases until reaching the familiar maximum rate first predicted by Richtmyer. In the early nonlinear phase, the existing RM modes coupled and we were able to observe the consequent new, harmonic modes that were produced. Finally, in the late nonlinear phase, the bubble-competition process begins to dominate, and we were able to observe the associated decrease in amplitude of shorter-wavelength modes. These physics results, as well as the validation of the Fourier interface-analysis techniques they provide, allowed us to introduce complex, multimode initial conditions. One future goal of this experiment is to use such multimode initial conditions to drive the system to self-similarity, which would allow experimental verification of theoretical predictions about RM self-similar behavior.

Chapter III presents work on the details of small-scale, shear-driven mixing. This work involved theoretical analysis of the mechanisms which lead shear flow to produce the growth of interface structure, including the effect of on initial conditions on the relative growth resulting from these mechanisms. These results were then used to predict experimentally-observed interface mixing. The experimental results are consistent with that expected from a self-similar system, although it is not immediately clear if the system is, in fact, self-similar. This provides a basis for future experimental and simulation work, in which the initial conditions are controlled more precisely, which could permit control of the growth of interface structure as well as stronger evidence of the system's self-similarity.

Chapter IV contains results from two separate directions of inquiry from an experimental platform intended to observe RT instability in a blast-wave-driven system

relevant to the physics of Type IIa supernova events. The first section is devoted to investigation of the breakup of RT structure at late times, and the possibility that the system could have become turbulent. I conclude that the particular parameters of this system to do not allow for the system to transition to a turbulent state on the timescale of the experiment. Instead, it is likely that the blast wave loses sufficient energy that inertial processes begin to dominate the dynamics, leading the ordered interface structure to begin to break apart as the system expands under its own pressure. The second section uses data on the propagation of the blast wave in this experiment to test the CRASH code's understanding of the creation and subsequent motion of the blast wave in systems like this. An appropriate scaling factor, to compensate for the simulation's known over-prediction of laser-driven shock strength, was identified. In addition, CRASH appears to predict the shock's trajectory better for higher-density CRF. Further experiments, especially ones in which the blast wave is measured in uniform plastic, would be useful in confirming these results.

Finally, Chapter V discusses work measuring the generation and propagation of high-energy electrons as a result of laser irradiation of a material. Although the physics contained in this chapter is substantially different from the main hydrodynamic-instability theme of this dissertation, all of the experiments previously described involve the irradiation of at least two materials, and energetic particles have the potential to affect both the physics and the diagnostics. Therefore, this work is relevant to the experimental techniques described elsewhere, in addition to its intrinsic interest as described in Chapter V. In this work, energetic electrons were detected primarily via the fluorescence of materials intercepting the propagating electrons. The configuration of the materials had a strong influence on the amount of observed fluorescence, which implies that different components of the electrons' energy spectrum are more anisotropic than others, an effect that can be traced back to coupling of the electrons to the laser's electric field. In particular, there are relatively few electrons generated

at high energies (roughly > 1 MeV), but these tend to be more strongly directional than lower-energy electrons.

BIBLIOGRAPHY

BIBLIOGRAPHY

[1] Y. Aglitskiy, A. L. Velikovich, M. Karasik, N. Metzler, S. T. Zalesak, A. J. Schmitt, L. Phillips, J. H. Gardner, V. Serlin, J. L. Weaver, and S. P. Obenschain. Basic hydrodynamics of Richtmyer–Meshkov-type growth and oscillations in the inertial confinement fusion-relevant conditions. *Philosophical Transactions of the Royal Society A: Mathematical, Physical and Engineering Sciences*, 368(1916):1739–1768, 2010.

[2] U. Alon, J. Hecht, D. Mukamel, and D. Shvarts. Scale invariant mixing rates of hydrodynamically unstable interfaces. *Phys. Rev. Lett.*, 72:2867–2870, May 1994.

[3] U. Alon, J. Hecht, D. Ofer, and D. Shvarts. Power laws and similarity of Rayleigh–Taylor and Richtmyer–Meshkov mixing fronts at all density ratios. *Phys. Rev. Lett.*, 74:534–537, Jan 1995.

[4] M. A. Barrios, T. R. Boehly, D. G. Hicks, D. E. Fratanduono, J. H. Eggert, G. W. Collins, and D. D. Meyerhofer. Precision equation-of-state measurements on National Ignition Facility ablator materials from 1 to 12 Mbar using laser-driven shock waves. *Journal of Applied Physics*, 111(9), 2012.

[5] M. A. Barrios, D. G. Hicks, T. R. Boehly, D. E. Fratanduono, J. H. Eggert, P. M. Celliers, G. W. Collins, and D. D. Meyerhofer. High-precision measurements of the equation of state of hydrocarbons at 1-10 Mbar using laser-driven shock wavesa). *Physics of Plasmas*, 17(5), 2010.

[6] F. N. Beg, A. R. Bell, A. E. Dangor, C. N. Danson, A. P. Fews, M. E. Glinsky, B. A. Hammel, P. Lee, P. A. Norreys, and M. Tatarakis. A study of picosecond laser-solid interactions up to 1019 w/cm². *Physics of Plasmas*, 4(2):447–457, 1997.

[7] M. C. Begelman. A model for the moving "wisps" in the Crab nebula. *The Astrophysical Journal*, 512(2):755, 1999.

[8] M. J. Berger and P. Colella. Local adaptive mesh refinement for shock hydrodynamics. *Journal of Computational Physics*, 82(1):64–84, 1989.

[9] T. R. Boehly, R. S. Craxton, T. H. Hinterman, J. H. Kelly, T. J. Kessler, S. A. Kumpan, S. A. Letzring, R. L. McCrory, S. F. B. Morse, W. Seka, S. Skupsky,

J. M. Soures, and C. P. Verdon. The upgrade to the OMEGA laser system. *Review of Scientific Instruments*, 66(1):508–510, 1995.

[10] S. I. Braginskii. *Reviews of Plasma Physics*, volume 1, page 205. Consultants Bureau, 1965.

[11] G. L. Brown and A. Roshko. On density effects and large structure in turbulent mixing layers. *Journal of Fluid Mechanics*, 64(4):775–816, 1974.

[12] C. A. M. Castelijns, J. G. M. Kuerten, A. T. A. M. de Waele, and H. M. Gijsman. ^{3}He flow in dilute ^{3}He-^{4}He mixtures at temperatures between 10 and 150 mK. *Phys. Rev. B*, 32:2870–2886, Sep 1985.

[13] Y. Cauchois. Spectrographie des rayons x par transmission d'un faisceau non canalisé ò travers un cristal courbé. *Journal de Physique*, 3:320, 1932.

[14] R. A. Chevalier. The hydrodynamics of Type II supernovae. *The Astrophysical Journal*, 207:872–887, August 1976.

[15] D. S. Clark, S. W. Haan, B. A. Hammel, J. D. Salmonson, D. A. Callahan, and R. P. J. Town. Plastic ablator ignition capsule design for the National Ignition Facility. *Physics of Plasmas*, 17(5), 2010.

[16] National Research Council Committee on High Energy Density Plasma Physics, Plasma Science Committee. *Frontiers in High Energy Density Physics: the X-Games of Contemporary Science.* The National Academies Press, 2003.

[17] G. M. Corcos and F. S. Sherman. Vorticity concentration and the dynamics of unstable free shear layers. *Journal of Fluid Mechanics*, 73:241–264, January 1976.

[18] C. A. Di Stefano, G. Malamud, M. T. Henry de Frahan, C. C. Kuranz, A. Shimony, S. R. Klein, R. P. Drake, E. Johnsen, D. Shvarts, V. A. Smalyuk, and D. Martinez. Observation and modeling of mixing-layer development in high-energy-density, blast-wave-driven shear flow. *Physics of Plasmas*, 21(5), 2014.

[19] C. A. Di Stefano, G. Malamud, C. C. Kuranz, S.R. Klein, C. Stoeckl, and R P. Drake. Richtmyer–Meshkov evolution under steady shock conditions in the high-energy-density regime. *submitted to Applied Physics Letters*, 2014.

[20] G. Dimonte and B. A. Remington. Richtmyer–Meshkov experiments on the Nova laser at high compression. *Phys. Rev. Lett.*, 70:1806–1809, March 1993.

[21] P. E. Dimotakis. The mixing transition in turbulent flows. *Journal of Fluid Mechanics*, 409:69–98, 2000.

[22] F. W. Doss, H. F. Robey, R. P. Drake, and C. C. Kuranz. Wall shocks in high-energy-density shock tube experiments. *Physics of Plasmas*, 16(11):112705, 2009.

[23] R. P. Drake. *High-energy-density physics*. Springer, 2006.

[24] R. P. Drake, D. R. Leibrandt, E. C. Harding, C. C. Kuranz, M. A. Blackburn, H. F. Robey, B. A. Remington, M. J. Edwards, A. R. Miles, T. S. Perry, R. J. Wallace, H. Louis, J. P. Knauer, and D. Arnett. Nonlinear mixing behavior of the three-dimensional Rayleigh–Taylor instability at a decelerating interface. *Physics of Plasmas*, 11(5):2829–2837, 2004.

[25] M. H. Emery, J. H. Gardner, and J. P. Boris. Rayleigh–Taylor and Kelvin–Helmholtz instabilities in targets accelerated by laser ablation. *Phys. Rev. Lett.*, 48:677–680, March 1982.

[26] P. Fitzsimmons. private communication, August 2012.

[27] Center for Magnetic Self-Organization in Laboratory and Astrophysical Plasmas.

[28] A. P. French. *Vibrations and Waves*. The MIT Introductory Physics Series. W. W. Norton and Co., New York, NY, 1971.

[29] S. G. Glendinning, J. Bolstad, D. G. Braun, M. J. Edwards, W. W. Hsing, B. F. Lasinski, H. Louis, A. Miles, J. Moreno, T. A. Peyser, B. A. Remington, H. F. Robey, E. J. Turano, C. P. Verdon, and Y. Zhou. Effect of shock proximity on Richtmyer–Meshkov growth. *Physics of Plasmas*, 10(5):1931–1936, 2003.

[30] S. W. Haan. On target: designing for ignition. *Science and Technology Review*, pages 4–11, July/August 1999.

[31] S. W. Haan, M. C. Herrmann, T. R. Dittrich, A. J. Fetterman, M. M. Marinak, D. H. Munro, S. M. Pollaine, J. D. Salmonson, G. L. Strobel, and L. J. Suter. Increasing robustness of indirect drive capsule designs against short wavelength hydrodynamic instabilities. *Physics of Plasmas*, 12(5), 2005.

[32] E. C. Harding, J. F. Hansen, O. A. Hurricane, R. P. Drake, H. F. Robey, C. C. Kuranz, B. A. Remington, M. J. Bono, M. J. Grosskopf, and R. S. Gillespie. Observation of a Kelvin-Helmholtz instability in a high-energy-density plasma on the Omega laser. *Physical Review Letters*, 103:045005, July 2009.

[33] J. Hecht, U. Alon, and D. Shvarts. Potential flow models of Rayleigh–Taylor and Richtmyer–Meshkov bubble fronts. *Physics of Fluids*, 6(12):4019–4030, 1994.

[34] H. L. F. Helmholtz. Über discontinuierliche flüssigkeits-bewegungen [on the discontinuous movements of fluids]. *Monatsberichte der Königlichen Preussische Akademie der Wissenschaften zu Berlin [Monthly Reports of the Royal Prussian Academy of Philosophy in Berlin]*, 23(215-228), 1868.

[35] M. T. Henry de Frahan and E. Johnsen. Discontinuous Galerkin method for multifluid Euler equations. In *Proc. 21st AIAA Computational Fluid Dynamics Conference*, 2013.

[36] J. D. Huba. *NRL Plasma Formulary*. Naval Research Laboratory, Washington, D.C., 2011.

[37] O. A. Hurricane. Design for a high energy density Kelvin–Helmholtz experiment. *High Energy Density Physics*, 4:97–102, 2008.

[38] O. A. Hurricane, J. F. Hansen, H. F. Robey, B. A. Remington, M. J. Bono, E. C. Harding, R. P. Drake, and C. C. Kuranz. A high energy density shock driven Kelvin–Helmholtz shear layer experiment. *Physics of Plasmas*, 16(5):056305, 2009.

[39] O. A. Hurricane, V. A. Smalyuk, K. Raman, O. Schilling, J. F. Hansen, G. Langstaff, D. Martinez, H.-S. Park, B. A. Remington, H.F. Robey, et al. Validation of a turbulent Kelvin–Helmholtz shear layer model using a high energy density OMEGA laser experiment. *Physical Review Letters*, 109(15):155004, 2012.

[40] J. Kane, R. P. Drake, and B. A. Remington. An evaluation of the Richtmyer–Meshkov instability in supernova remnant formation. *The Astrophysical Journal*, 511:335–340, January 1999.

[41] G. W. C. Kaye and T. H. Laby. *Tables of physical and chemical constants*. Longman, London, UK, 15th edition, 1993.

[42] M. H. Key. Status of and prospects for the fast ignition inertial fusion concept. *Physics of Plasmas*, 14(5), 2007.

[43] A. M. Khokhlov. Fully threaded tree algorithms for adaptive refinement fluid dynamics simulations. *Journal of Computational Physics*, 143(2):519–543, 1998.

[44] R. Kodama, P. A. Norreys, K. Mima, A. E. Dangor, R. G. Evans, H. Fujita, Y. Kitagawa, K. Krushelnick, T. Miyakoshi, N. Miyanaga, T. Norimatsu, S. J. Rose, T. Shozaki, K. Shigemori, A. Sunahara, M. Tampo, K. A. Tanaka, Y. Toyama, T. Yamanaka, and M. Zepf. Fast heating of ultrahigh-density plasma as a step towards laser fusion ignition. *Nature*, 412, 2001.

[45] H. Kolbenstvedt. Simple theory for K-ionization by relativistic electrons. *Journal of Applied Physics*, 38(12):4785–4787, 1967.

[46] C. M. Krauland, L. C. Jarrott, R. P. Drake, P. A. Keiter, C. C. Kuranz, B. Westover, H. Sawada, D. N. Kaczala, and P. Bonofiglio. An evaluation of high energy bremsstrahlung background in point-projection x-ray radiography experiments. *Review of Scientific Instruments*, 83(10, 2), October 2012. 19th Topical Conference on High-Temperature Plasma Diagnostics, Monterey, CA, May 06-10, 2012.

[47] P. K. Kundu, I. M. Cohen, and D. R. Dowling. *Fluid Mechanics*. Academic Press, Boston, fifth edition, 2012.

[48] C. C. Kuranz, B. E. Blue, R. P. Drake, H. F. Robey, J. F. Hansen, J. P. Knauer, M. J. Grosskopf, C. Krauland, and D. C. Marion. Dual, orthogonal backlit pinhole radiography in OMEGA experiments. *Review of Scientific Instruments*, 77(10), 2006.

[49] C. C. Kuranz, F. W. Doss, R. P. Drake, M. J. Grosskopf, and H. F. Robey. Using wall shocks to measure preheat in laser-irradiated, high-energy-density, hydrodynamics experiments. *High Energy Density Physics*, 6(2):215 – 218, 2010. (ICHED 2009 - 2nd International Conference on High Energy Density Physics).

[50] C. C. Kuranz, R. P. Drake, M. J. Grosskopf, A. Budde, C. Krauland, D. C. Marion, A. J. Visco, J. R. Ditmar, H. F. Robey, B. A. Remington, A. R. Miles, A. B. R. Cooper, C. Sorce, T. Plewa, N. C. Hearn, K. L. Killebrew, J. P. Knauer, D. Arnett, and T. Donajkowski. Three-dimensional blast-wave-driven Rayleigh–Taylor instability and the effects of long-wavelength modes. *Physics of Plasmas*, 16(5):056310, 2009.

[51] C. C. Kuranz, R. P. Drake, E. C. Harding, M. J. Grosskopf, H. F. Robey, B. A. Remington, M. J. Edwards, A. R. Miles, T. S. Perry, B. E. Blue, T. Plewa, N. C. Hearn, J. P. Knauer, D. Arnett, and D. R. Leibrandt. Two-dimensional blast-wave-driven Rayleigh–Taylor instability: experiment and simulation. *The Astrophysical Journal*, 696(1):749, 2009.

[52] C. C. Kuranz, R. P. Drake, C. M. Huntington, C. M. Krauland, C. A. Di Stefano, M. Trantham, M. J. Grosskopf, S. R. Klein, and D. C. Marion. Early-time evolution of a radiative shock. *High Energy Density Physics*, 9(2):315–318, 2013.

[53] N. E. Lanier, J. S. Cowan, and J. Workman. Characterization and cross calibration of Agfa D4, D7, and D8 and Kodak SR45 x-ray films against direct exposure film at 4.0–5.5 keV. *Review of Scientific Instruments*, 77(4), 2006.

[54] J. T. Larsen and S. M. Lane. HYADES: a plasma hydrodynamics code for dense plasma studies. *Journal of Quantitative Spectroscopy and Radiative Transfer*, 51(1Äì2):179–186, 1994.

[55] B. R. Maddox, H. S. Park, B. A. Remington, N. Izumi, S. Chen, C. Chen, G. Kimminau, Z. Ali, M. J. Haugh, and Q. Ma. High-energy x-ray backlighter spectrum measurements using calibrated image plates. *Review of Scientific Instruments*, 82(2):023111, 2011.

[56] G. Malamud, C. A. Di Stefano, Y. Elbaz, C. M. Huntington, C. C. Kuranz, P. A. Keiter, and R. P. Drake. A design of a two-dimensional, multimode RM experiment on OMEGA-EP. *High Energy Density Physics*, 9(1):122–131, 2013.

[57] G. Malamud, A. Shimoni, C. A. Di Stefano, Y. Elbaz, C. C. Kuranz, P. A. Keiter, D. Shvarts, and R. P. Drake. A design for a two vortex merger KH

experiment on OMEGA-EP. In *APS Meeting Abstracts*, volume 1, page 6006, 2012.

[58] G. Malamud, A. Shimony, W. C. Wan, C. A. Di Stefano, Y. Elbaz, C. C. Kuranz, P. A. Keiter, R. P. Drake, and D. Shvarts. A design of a two-dimensional, supersonic KH experiment on OMEGA-EP. *High Energy Density Physics*, 9(4):672–686, 2013.

[59] D. Martinez, V. A. Smalyuk, H.-S. Park, B. A. Remington, A. Casner, L. Masses, B. Delorme, I. Igumenshev, D. Shvarts, and Y. Elbaz. Measurement of Richtmyer–Meshkov growth from laser imprint.

[60] D. N. Maywar, J. H. Kelly, L. J. Waxer, S. F. B. Morse, I. A. Begishev, J. Bromage, C. Dorrer, J. L. Edwards, L. Folnsbee, M. J. Guardalben, S. D. Jacobs, R. Jungquist, T. J. Kessler, R. W. Kidder, B. E. Kruschwitz, S. J. Loucks, J. R. Marciante, R. L. McCrory, D. D. Meyerhofer, A. V. Okishev, J. B. Oliver, G. Pien, J. Qiao, J. Puth, A. L. Rigatti, A. W. Schmid, M. J. Shoup III, C. Stoeckl, K. A. Thorp, and J. D. Zuegel. OMEGA EP high-energy petawatt laser: progress and prospects. *Journal of Physics: Conference Series*, 112(3):032007, 2008.

[61] A. L. Meadowcroft, C. D. Bentley, and E. N. Stott. Evaluation of the sensitivity and fading characteristics of an image plate system for x-ray diagnostics. *Review of Scientific Instruments*, 79(11), 2008.

[62] E. E. Meshkov. Instability of the interface of two gases accelerated by a shock wave. *Soviet Fluid Dynamics*, 4:101–104, 1969.

[63] K. A. Meyer and P. J. Blewett. Numerical investigation of the stability of a shock accelerated interface between two fluids. *Physics of Fluids (1958-1988)*, 15(5):753–759, 1972.

[64] A. R. Miles, B. Blue, M. J. Edwards, J. A. Greenough, J. F. Hansen, H. F. Robey, R. P. Drake, C. C. Kuranz, and D. R. Leibrandt. Transition to turbulence and effect of initial conditions on three-dimensional compressible mixing in planar blast-wave-driven systems. *Physics of Plasmas*, 12(5):056317, 2005.

[65] A. R. Miles, D. G. Braun, M. J. Edwards, H. F. Robey, R. P. Drake, and D. R. Leibrandt. Numerical simulation of supernova-relevant laser-driven hydro experiments on OMEGA. *Physics of Plasmas*, 11(7):3631–3645, 2004.

[66] A. R. Miles, M. J. Edwards, and J. A. Greenough. Effect of initial conditions on two-dimensional Rayleigh–Taylor instability and transition to turbulence in planar blast-wave-driven systems. *Physics of Plasmas*, 11(11):5278–5296, 2004.

[67] G. H. Miller and E. G. Puckett. A high-order Godunov method for multiple condensed phases. *Journal of Computational Physics*, 128(1):134–164, 1996.

[68] J. Myatt, W. Theobald, J. A. Delettrez, C. Stoeckl, M. Storm, T. C. Sangster, A. V. Maximov, and R. W. Short. High-intensity laser interactions with mass-limited solid targets and implications for fast-ignition experiments on OMEGA EP. *Physics of Plasmas*, 14(5), 2007.

[69] C. E. Niederhaus and J. W. Jacobs. Experimental study of the Richtmyer–Meshkov instability of incompressible fluids. *Journal of Fluid Mechanics*, 485:243–277, 4 2003.

[70] P. M. Nilson, W. Theobald, J. F. Myatt, C. Stoeckl, M. Storm, J. D. Zuegel, R. Betti, D. D. Meyerhofer, and T. C. Sangster. Bulk heating of solid-density plasmas during high-intensity-laser plasma interactions. *Phys. Rev. E*, 79:016406, January 2009.

[71] L. Ofman and B. J. Thompson. SDO/AIA observation of Kelvin–Helmholtz instability in the solar corona. *The Astrophysical Journal Letters*, 734(1):L11, June 2011.

[72] G. C. Orlicz, S. Balasubramanian, and K. P. Prestridge. Incident shock Mach number effects on Richtmyer–Meshkov mixing in a heavy gas layer. *Physics of Fluids*, 25(11), 2013.

[73] K. S. Raman, O. A. Hurricane, H.-S. Park, B. A. Remington, H. Robey, V. A. Smalyuk, R. P. Drake, C. M. Krauland, C. C. Kuranz, J. F. Hansen, and E. C. Harding. Three-dimensional modeling and analysis of a high energy density Kelvin–Helmholtz experiment. *Physics of Plasmas*, 19(9), 2012.

[74] Lord Rayleigh. *Scientific Papers*, volume II. Cambridge University Press, Cambridge, England, 1900.

[75] B. A. Remington, S. V. Weber, M. M. Marinak, S. W. Haan, J. D. Kilkenny, R. Wallace, and G. Dimonte. Multimode Rayleigh–Taylor experiments on Nova. *Phys. Rev. Lett.*, 73:545–548, Jul 1994.

[76] R. D. Richtmyer. Taylor instability in shock acceleration of compressible fluids. *Communications on Pure and Applied Mathematics*, 13(2):297–319, 1960.

[77] A. Rikanati, U. Alon, and D. Shvarts. Vortex-merger statistical-mechanics model for the late time self-similar evolution of the Kelvin–Helmholtz instability. *Physics of Fluids*, 15(12):3776–3785, 2003.

[78] H. F. Robey, J. O. Kane, B. A. Remington, R. P. Drake, O. A. Hurricane, H. Louis, R. J. Wallace, J. Knauer, P. A. Keiter, D. Arnett, and D. D. Ryutov. An experimental testbed for the study of hydrodynamic issues in supernovae. *Physics of Plasmas*, 8(5):2446–2453, 2001.

[79] H. F. Robey, Ye Zhou, A. C. Buckingham, P. Keiter, B. A. Remington, and R. P. Drake. The time scale for the transition to turbulence in a high Reynolds number, accelerated flow. *Physics of Plasmas*, 10(3):614–622, 2003.

[80] A. Rose. Television camera tubes and the problem of vision. *Advances in Electronics and Electron Physics*, 1:131–166, 1948.

[81] A. Rose. *Vision: Human and Electronic.* Plenum Press, New York, NY, 1974.

[82] D. D. Ryutov, R. P. Drake, J. O. Kane, E. Liang, B. A. Remington, and W. M. Wood-Vasey. Similarity criteria for the laboratory simulation of supernova hydrodynamics. *The Astrophysical Journal*, 518(2):821, 1999.

[83] O. Sadot, L. Erez, U. Alon, D. Oron, L. A. Levin, G. Erez, G. Ben-Dor, and D. Shvarts. Study of nonlinear evolution of single-mode and two-bubble interaction under Richtmyer–Meshkov instability. *Phys. Rev. Lett.*, 80:1654–1657, Feb 1998.

[84] J. F. Seely, G. E. Holland, L. T. Hudson, C. I. Szabo, A. Henins, H.-S. Park, P. K. Patel, R. Tommasini, and J. M. Laming. K-shell spectra from Ag, Sn, Sm, Ta, and Au generated by intense femtosecond laser pulses. *High Energy Density Physics*, 3:263–271, 2007. Radiative Properties of Hot Dense Matter.

[85] J. F. Seely, L. T. Hudson, G. E. Holland, and A. Henins. Enhanced x-ray resolving power achieved behind the focal circles of Cauchois spectrometers. *Applied Optics*, 47(15):2767–2778, 2008.

[86] J. F. Seely, C. I. Szabo, P. Audebert, and E. Brambrink. Energetic electron propagation in solid targets driven by the intense electric fields of femtosecond laser pulses. *Physics of Plasmas*, 18(6):062702, 2011.

[87] J. F. Seely, C. I. Szabo, P. Audebert, E. Brambrink, E. Tabakhoff, G. E. Holland, L. T. Hudson, A. Henins, P. Indelicato, and A. Gumberidze. Hard X-ray spectroscopy of inner-shell K transitions generated by MeV electron propagation from intense picosecond laser focal spots. *High Energy Density Physics*, 5(4):263 – 269, 2009.

[88] J. F. Seely, C. I. Szabo, P. Audebert, E. Brambrink, E. Tabakhoff, and L. T. Hudson. Lateral propagation of mev electrons generated by femtosecond laser irradiation. *Physics of Plasmas*, 17(2):023102, 2010.

[89] V. A. Smalyuk, J. F. Hansen, O. A. Hurricane, G. Langstaff, D. Martinez, H.-S. Park, K. Raman, B. A. Remington, H. F. Robey, O. Schilling, R. Wallace, Y. Elbaz, A. Shimony, D. Shvarts, C. A. Di Stefano, R. P. Drake, D. C. Marion, C. M. Krauland, and C. C. Kuranz. Experimental observations of turbulent mixing due to Kelvin–Helmholtz instability on the OMEGA laser facility. *Physics of Plasmas*, 19(9):092702, 2012.

[90] V. A. Smalyuk, O. A. Hurricane, J. F. Hansen, G. Langstaff, D. Martinez, H.-S. Park, K. Raman, B. A. Remington, H. F. Robey, O. Schilling, R. Wallace, Y. Elbaz, A. Shimony, D. Shvarts, C. A. Di Stefano, R. P. Drake, D. C. Marion, C. M. Krauland, and C. C. Kuranz. Measurements of turbulent mixing due

to Kelvin–Helmholtz instability in high-energy-density plasmas. *High Energy Density Physics*, 9(1):47–51, 2013.

[91] C. Stoeckl, G. Fiksel, D. Guy, C. Mileham, P. M. Nilson, T. C. Sangster, M. J. Shoup, 3rd, and W. Theobald. A spherical crystal imager for OMEGA EP. *Rev Sci Instrum*, 83(3):033107, March 2012.

[92] D. C. Swift and R. G. Kraus. Properties of plastic ablators in laser-driven material dynamics experiments. *Phys. Rev. E*, 77:066402, June 2008.

[93] M. Tabak, J. Hammer, M. E. Glinsky, W. L. Kruer, S. C. Wilks, J. Woodworth, E. M. Campbell, M. D. Perry, and R. J. Mason. Ignition and high gain with ultrapowerful lasers. *Physics of Plasmas*, 1(5):1626–1634, 1994.

[94] G. Taylor. The instability of liquid surfaces when accelerated in a direction perpendicular to their planes. I. *Royal Society of London Proceedings Series A*, 201:192–196, March 1950.

[95] W. Thomson. Hydrokinetic solutions and observations. *Philosophical Magazine*, 42:362–377, 1871.

[96] B. Thornber, D. Drikakis, D. L. Youngs, and R. J. R. Williams. The influence of initial conditions on turbulent mixing due to Richtmyer–Meshkov instability. *Journal of Fluid Mechanics*, 654:99–139, 6 2010.

[97] E. F. Toro, M. Spruce, and W. Speares. Restoration of the contact surface in the HLL–Riemann solver. *Shock Waves*, 4(1):25–34, 1994.

[98] B. van der Holst, G. Tóth, I. V. Sokolov, K. G. Powell, J. P. Holloway, E. S. Myra, Q. Stout, M. L. Adams, J. E. Morel, S. Karni, B. Fryxell, and R. P. Drake. CRASH: A block-adaptive-mesh code for radiative shock hydrodynamics— implementation and verification. *The Astrophysical Journal Supplement Series*, 194(2):23, 2011.

[99] B. van der Holst, G. Tóth, I. V. Sokolov, B. R. Torralva, K. G. Powell, R. P. Drake, M. Klapisch, M. Busquet, B. Fryxell, and E. S. Myra. Simulating radiative shocks with the CRASH laser package. *High Energy Density Physics*, 9(1):8–16, 2013.

[100] A. L. Velikovich, J. P. Dahlburg, A. J. Schmitt, J. H. Gardner, L. Phillips, F. L. Cochran, Y. K. Chong, G. Dimonte, and N. Metzler. Richtmyer–Meshkov-like instabilities and early-time perturbation growth in laser targets and Z-pinch loads. *Physics of Plasmas*, 7(5):1662–1671, 2000.

[101] K. B. Wharton, S. P. Hatchett, S. C. Wilks, M. H. Key, J. D. Moody, V. Yanovsky, A. A. Offenberger, B. A. Hammel, M. D. Perry, and C. Joshi. Experimental measurements of hot electrons generated by ultraintense ($> 10^{19}$ W/cm^2) laser-plasma interactions on solid-density targets. *Phys. Rev. Lett.*, 81:822–825, July 1998.

[102] S. C. Wilks and W. L. Kruer. Absorption of ultrashort, ultra-intense laser light by solids and overdense plasmas. *Quantum Electronics, IEEE Journal of*, 33(11):1954–1968, November 1997.

[103] J. Workman and G. A. Kyrala. X-ray yield scaling studies performed on the OMEGA laser. *Review of Scientific Instruments*, 72(1):678–681, 2001.

[104] Y. Yang, Q. Zhang, and D. H. Sharp. Small amplitude theory of Richtmyer–Meshkov instability. *Physics of Fluids*, 6(5):1856–1873, 1994.

[105] Q. Zhang and S.-I. Sohn. An analytical nonlinear theory of Richtmyer–Meshkov instability. *Physics Letters A*, 212(3):149–155, 1996.

[106] Q. Zhang and S.-I. Sohn. Nonlinear theory of unstable fluid mixing driven by shock wave. *Physics of Fluids*, 9(4):1106–1124, 1997.

[107] Y. Zhou. Unification and extension of the similarity scaling criteria and mixing transition for studying astrophysics using high energy density laboratory experiments or numerical simulations. *Physics of Plasmas*, 14(8):082701, 2007.